# Copper zinc tin sulfide ($Cu_2ZnSnS_4$) photovoltaic material development and thin film solar cells

A DISSERTATION

SUBMITTED TO THE FACULTY OF

UNIVERSITY OF MINNESOTA

BY

Liyuan Zhang

IN PARTIAL FULFILLMENT OF THE REQUIREMENTS

FOR THE DEGREE OF

DOCTOR OF PHILOSOPHY

Professor Stephen A. Campbell

March, 2016

## Acknowledgements

I've been waiting for writing this page since I started my thesis. Going through all the up and down, I finally realize how lucky I am. I would not have been able to achieve this without the constant support and encouragement from my advisor, collaborators, colleagues, friends and family.

I would first like to thank my advisor, Prof. Stephen Campbell, for his continuous support, patience, guidance, and encouragement over the past five and half years. The weekly meetings, and hands-on guidance in the lab were great lessons to learn from. I am also thankful for the advisement from Prof. Eray Aydil, Prof. Chris Leighton, Dr. Michael Manno and all the discussions with Melissa Johnson and Xin Zhang. Their expertise and knowledge helped to extend my study to broader areas. I am extremely thankful for all my group members, Sreejith Karthikeyan, Mandip Sibakoti, Brian Benton, JunYoung Lim, Forrest Johnson, Sehyun Hwang, Tim Bontrager for all those invaluable discussions and enjoyable time working both in the lab and office. I also would like to thank my previous lab members including Brijesh Kumar, Sang-Ho Song, and Maryam Jalali-Mousavi, who have also been guiding and supporting me through the years.

I am so grateful to have all my friends and family with me through this journey. Words cannot express how much my parents have meant though all of thick and thin. It is their continuous support and guidance that makes me who I am today. And to my best friend Dong Qin, who has been there for me for better or worse, you are the light in my life. I am also thankful for my friends, Xiaoshu Chen, Luxi Li, Guan Wang, Shu Xiao, Haoping Wang, Ke Li, Rui Ma and Yoska Anugrah, who have been very supportive for the last five and half years. I am so grateful to have all of you in my life.

## Dedication

To my parents, Yangmin and Huizhen.

## Abstract

Copper zinc tin sulfide ($Cu_2ZnSnS_4$, or CZTS) is emerging as an alternative light absorbing material to the present thin film solar cell technologies such as $Cu(In,Ga)Se_2$ and CdTe. All the elements in CZTS are abundant, environmentally benign, and inexpensive. In addition, CZTS has a band gap of ~1.5 eV, the ideal value for converting the maximum amount of energy from the solar spectrum into electricity. CZTS has a high absorption coefficient ($>10^4$ $cm^{-1}$ in the visible region of the electromagnetic spectrum) and only a few micron thick layer of CZTS can absorb all the photons with energies above its band gap. Pure sulfide CZTS solar cells have already reached power conversion efficiencies ~8.5% [1].

A two-stage process of CZTS thin film synthesis is presented, which consists of sequential thermal evaporation of copper, tin and zinc layers followed by a heat treatment in the presence of sulfur vapor (sulfurization) in a sealed quartz ampoule. The metal precursor stacking order, deposition rate and thickness of each metal layer can be adjusted to give uniform metal precursor stacks of controlled morphology and composition. The effects of sulfurization temperature, time, substrate material, metal precursor stacking order, and back contact layer on the morphological and structural properties of the CZTS films are investigated. Observations of grain size changes and compositional modification are made and explained in terms of the likely secondary phases present.

CZTS thin film solar cells were fabricated and the effects of chemical composition were studied both on the absorber layer properties and on the final solar cell performance. It is confirmed that CZTS thin film chemical composition affects the carrier concentration profile, which then influences the solar cell properties. Only a small deviation from the optimal chemical composition can drop device performance to a lower level, which confirms that the CZTS solar cells with high conversion efficiency existed in a relatively narrow composition region.

Besides CZTS absorber chemical composition study, post deposition rapid thermal annealing (RTA) was conducted and its influence on solar cell performance was studied. It is observed that post deposition RTA would lead to an increase of device performance. Through C-V measurement results, we have shown that post RTA of CZTS solar cell affects the CZTS/CdS interfacial defect concentration and zero bias depletion depth, which means the defect-related charge at CZTS/CdS interface reduces and it improves $V_{oc}$ and the fill factor.

## Table of Contents

## List of Tables

## List of Figures

# Chapter 1

# 1 Introduction

## 1.1 Importance of Renewable Energy, and Especially Solar Energy

Ever since the Industrial Revolution took off in the 18th century, vast quantities of fossil fuels, such as coal, petroleum and natural gas, have been used to power the economy and it also led to significant development of science and technology. The development of drilling technology for oil wells in mid-19th century America led to mass-consumption of petroleum as a high specific energy fuel, powering transportation in the form of automobiles, ships, and airplanes, applied to generate electricity, used for heating and to provide hot water.

The use of fossil fuels has been increasing in step with economic and population growth. They were prerequisites for the birth of a new industrial civilization that transformed our world. However, the total reserve of fossil fuels is limited while global energy consumption is increasing rapidly. Given the large pressure on energy crisis, increasingly severe environmental problems pushed the expanded exploitation of renewable energy sources world-widely. The main environmental problems are classified as water pollution, maritime pollution, solid waste disposal [2], hazardous air pollutants, ambient air quality, acid rain, stratospheric ozone depletion, and global climate change

(greenhouse effect). In principle, all of these can be solved or relieved by the use of renewable energy [3].

Renewable energy technologies convert direct or indirect effect of sunlight (wind, falling water, plant growth) and other effects (tides, heat of the earth's core) into more useful forms of energy. These resources indicate a massive available energy potential, but only a small amount of them are being effectively used at current stage. Considering that they are usually diffusive, not fully accessible, and all have distinct regional variability, it is difficult to develop and apply these renewable energy resources. Although there have been decades of studies in the field, further research is required to extract the full potential of these resources [2].

Solar energy technologies use direct sunlight to produce electrical energy. It is considered to be the most abundant and effective among all available renewable energy resources. Solar energy has already been theoretically and experimentally proved to be environmentally friendly if being used properly [4]. In fact, with 20% efficient solar cells covering only 0.1% of the earth's surface would provide sufficient energy to satisfy the entire global electric energy demand [4].

## 1.2 Brief History of Solar Cell

The photovoltaic effect was first discovered by a French scientist, Edmond Becquerel, while he was experimenting with an electrolyte cell made up of two metal electrodes

placed in a conductive solution in 1839 [5]. In 1873 Willoughby Smith, an English engineer, discovered the photo conductive property of a selenium bar exposed to light during the passage of electrical current [6]. In 1876, William Grylls Adams and Richard Evans Day discovered that a junction between selenium and platinum produces electricity when exposed to light. Their fabricated selenium cells proved that light can be converted into electricity without heat or any mechanical moving parts [7]. Charls Fritts developed the first solar cell from selenium on a thin gold layer in 1883 [7]. In 1905, Albert Einstein published his paper on photoelectric effect and explained these phenomena theoretically [8]. He demonstrated the discrete nature of light in which electrons are emitted from a solid surface due to the quantized energy of the absorbed light called *photons* [8]. The minimum energy required to eject an electron from the solid is called *work function*, which is a characteristic of a material.

Three American researchers, Gerald Pearson, Calvin Fuller and Daryl Chapin, at Bell Labs designed a silicon solar cell capable of 6% energy conversion efficiency under direct sunlight, which made 1954 a significant year in solar cell research. This was the first solar cell that could convert solar energy to produce usable power for electrical equipment. They created the first solar panel based on several serially connected silicon strips. This was the starting point of the commercial exploitation of the use of solar energy [7]. Solar cells have been used in space satellites since 1958 and in providing residential electricity since 1978. Due to its increasing efficiency and decreasing cost,

solar energy production is increasing and may be the ultimate solution for the worldwide energy crisis.

## 1.3 Photovoltaic Fundamentals

### 1.3.1 Solar Energy

The sun is by far the most important energy source on earth and it is responsible for almost every aspects of our daily life. The temperature of the solar photosphere is about 5778 K, while the temperature of the extremely dense and hot core is about $1.57\times10^7$ K where thermonuclear fusion happens and huge amount of energy is radiated [9]. At edge of the upper atmosphere of the earth, 174,000 terawatts (TW) of incoming solar radiation is received. Approximately 30% of the energy is reflected back to space. The rest is absorbed by atmosphere, oceans and lands and then re-radiated at a lower frequency [9]. Solar radiation nearly matches the spectrum of a broad band black body emitter. The light intensity decreases as it passes through the atmosphere because of scattering and absorption effects [10]. In order to characterize the solar spectrum after solar radiation has traveled through the atmosphere and test solar cells under standardized conditions, the *air mass coefficient* (AM) is defined.

For a path length L through the atmosphere, for solar radiation incident at angle θ relative to the normal to the earth's surface the AM coefficient is [11]:

$$AM = \frac{L}{L_0} \approx \frac{1}{\cos\theta} \quad (1.1)$$

where $L_0$ is the zenith path length (normal to the earth's surface) at sea level and θ is the zenith angle in degrees. The AM coefficient value is thus dependent on several factors, such as time of the day, seasons of the year, and the latitude of the observer.

Several common cases of AM number include [11]:

1. AM0: meaning "zero atmosphere", the spectrum outside the atmosphere, approximated by the 5778 K black body.

2. AM1: meaning "one atmosphere", the spectrum after traveling through the atmosphere to sea level with the sun directly overhead, $\theta = 0^o$.

3. AM1.5: meaning "1.5 atmosphere", corresponds to a solar zenith angle of $\theta = 48.2^o$, useful to represent a yearly average AM number for mid-latitude areas. It has been selected for the global standardized testing and rating of terrestrial solar cells and modules [12].

4. AM2~3: AM2 ($\theta = 60^o$) to AM3 ($\theta = 70^o$) is a useful range for estimating the overall average performance of solar cells installed at high latitudes or wintertime solar cell performance.

Solar radiation *spectral power density* (P) is defined as incident power per unit area per unit wavelength. The spectral distribution of solar radiation with different values of AM coefficient is shown in Figure 1.1 [13].

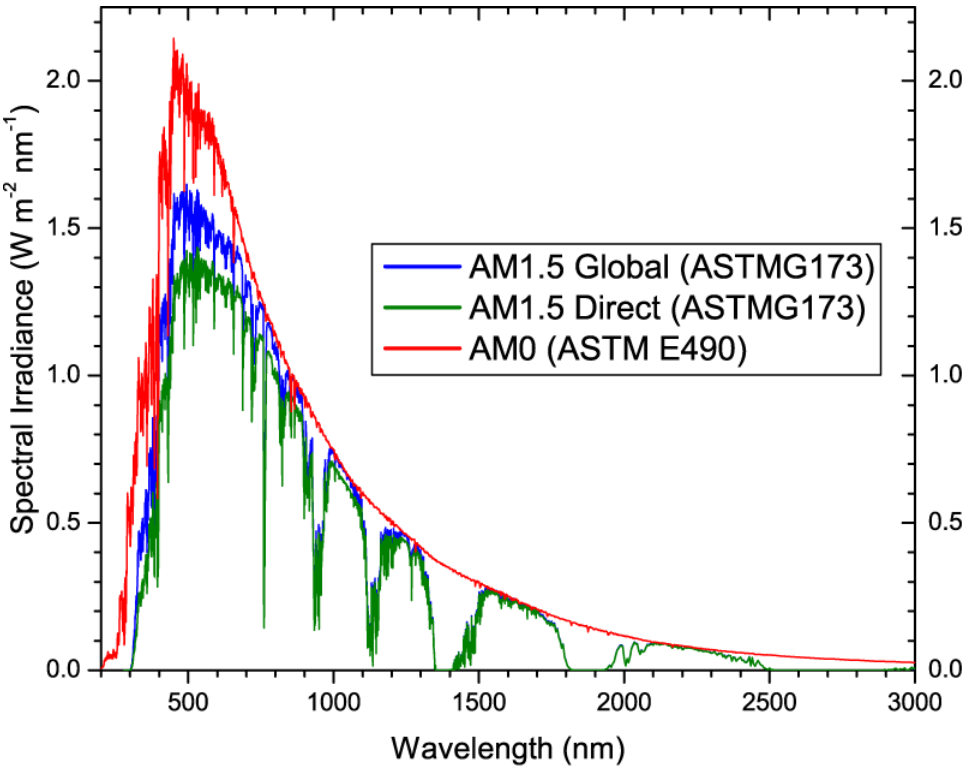


**Figure 1.1 Standard Solar Spectra for space and terrestrial use. (Source: Department of Energy National Renewable Energy Laboratory)**

The power density of the solar spectrum reduces in the IR region and is prominent at the shorter wavelengths, especially near 500 nm (2.48 eV). Figure 1.1 supports cells with an absorbing material at a band gap near to 2.48 eV, *i.e.* materials such as CdS (2.4 eV). But such cells experience lower photon flux.

In order to choose optimal absorbing materials for single junction solar cells, the *photon flux density* (Φ) also needs to be considered. It is defined as the number of incident photons per unit area per unit time.

$$P\left(\frac{W}{m^2}\right) = \Phi \times \frac{hc}{\lambda} = \Phi \times q\,\frac{1.24}{\lambda} \qquad (1.2)$$

where Φ is measured in photons per $m^2$-sec, q is the conversion factor for energy ($1.6\times10^{-19}$ J/eV), and $\lambda$ is measured in micrometers.

The photon flux density of solar radiation is higher for larger wavelengths, especially in infra-red regions. In ultra-violet region, the power density is prominent but photon flux density is lower. Thus, wide band gap materials have fewer photo-generated electrons promoted to the conduction band resulting in a reduction in photocurrent but producing a higher solar cell output voltage. On the other hand, smaller band gap materials produce more current. However, the excess energy of incoming photons needs to be dissipated in the form of heat.

The theoretical limit of the conversion efficiency of a single *p-n* junction solar cell was first calculated by William Schockley and Hans Queisser in 1961 and is known as the Shockley-Queisser limit. They reported a maximum efficiency of 30% with a single *p-n* junction with band gap 1.1 eV [14]. They suggested a range between 1 and 1.5 eV for a single *p-n* junction cell, but other researchers have proposed slightly different values [15, 16].

### 1.3.2 Photovoltaic Physics

A solar cell, or photovoltaic cell, is a device that can convert direct solar energy to electrical energy in the form of voltage and current by the photovoltaic effect. The fundamental four processes for photovoltaic energy conversion are [17]:

1. Light absorption, which causes a transition in a material from ground state to an excited state when the incident photon energy is equal or larger than the absorber material bandgap.

2. Conversion process, which converts the excitons to a free negative- and a free positive-charge carrier pair.

3. Separation process, which causes the free negative-charge carriers to move to the cathode and free positive-charge carriers to move to the anode.

4. Recombination process, which causes the recombination of an arriving positive-charge carrier with a negative-charge carrier, thereby returning the material to the ground state.

Usually, a *p-n* junction is required to help separate and transfer carriers to cathode and anode, respectively. *P-n* junctions can be classified as *homogeneous*, if the junction is made up of the same materials or *heterogeneous*, if the junction is made up of two different semiconducting materials. In order to study the characteristics of an absorbing semiconductor material, a diagram showing the allowed values of energy *E* versus the

propagation constant ***k***, also called the carrier momentum (an *E*-***k*** or band diagram), is quite useful [17]. For example, GaAs is a *direct* band gap semiconductor which means the lowest position of the conduction band aligns with the maximum value of the valance band at the same ***k*** value. As for silicon, an *indirect* band gap semiconductor, this occurs at different ***k*** values. This suggests that in GaAs, an electron can transition from the conduction band to the valance band without change in ***k***, while in Si, a change in ***k*** and electron momentum is required. Direct band gap semiconductors absorb light more efficiently compared with the indirect materials. Therefore solar cells with indirect materials such as Si require a thicker layer for absorbing a given fraction of the incident radiation. This thick layer requires highly perfect material since recombination sites can reduce the performance of the solar cells if the absorber thickness becomes comparable to the minority carrier diffusion length.

The performance of a solar cell can be characterized by the current-voltage (I-V) characteristic, the energy conversion efficiency ($\eta_{eff}$), the short-circuit current ($I_{sc}$), the open-circuit voltage ($V_{oc}$), and a fill factor (FF). The ideal equivalent circuit of a solar cell is a constant-current source of photocurrent in parallel with a *p*-*n* junction, as shown in Figure 1.2.

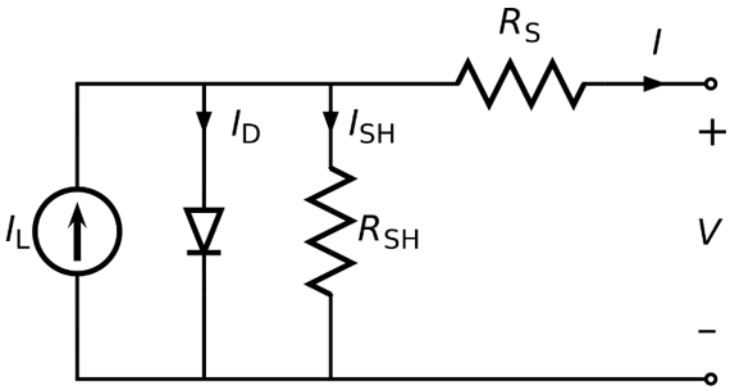


**Figure 1.2 The ideal equivalent circuit of a solar cell [18].**

The source $I_L$ results from the excitation of excess carriers by solar radiation; $I_D$ is the diode saturation current and $R_S$ and $R_{SH}$ are series resistance and shunt resistance, respectively. The total I-V characteristics of a solar cell under illumination is simply a summation of the dark current and the photocurrent, given as

$$I = I_D \left[ exp\left(\frac{qV}{kT}\right) - 1 \right] - I_L - I_{SH} \tag{1.3}$$

By setting $I = 0$, we can obtain the open-circuit voltage ($I_{SH}$ is negligible if $R_{SH}$ is large)

$$V_{oc} = \frac{kT}{q} \ln\left(\frac{I_L + I_{SH}}{I_D} + 1\right) \approx \frac{kT}{q} \ln\left(\frac{I_L}{I_D}\right) \tag{1.4}$$

While by setting $V = 0$, we can obtain the short-circuit current

$$I_{sc} \approx I_L \tag{1.5}$$

The output power is given by

$$P = IV = I_D V \left[ exp\left(\frac{qV}{kT}\right) - 1 \right] - I_L V \tag{1.6}$$

The maximum output power operating point, $I_m$ and $V_m$, can be derived from the condition $\frac{dP}{dV} = 0$.

The fill factor (FF) measures the sharpness of the I-V curve and is defined as

$$FF = \frac{I_m V_m}{I_{sc} V_{oc}} \tag{1.7}$$

The energy conversion efficiency is defined as the ratio of the maximum output power to the incident power $P_{in}$,

$$\eta_{eff} = \frac{P_m}{P_{in}} = \frac{I_m V_m}{P_{in}} \tag{1.8}$$

Quantum efficiency (QE) indicates the ability of a solar cell to produce photocurrent when irradiated by photons of a certain wavelength. Integrating the product of the QE and the incident intensity over the solar radiation spectrum one obtains the current that a solar cell produces when exposed to sunlight. Two types of QE are commonly considered, internal quantum efficiency (IQE) and external quantum efficiency (EQE). IQE is defined as the ratio of the number of charge carriers collected by solar cell to the number of absorbed photons of a given energy. EQE is the ratio of the number of charge carriers collected by solar cell to the number of incident photons of a given energy.

$$EQE = \frac{electrons/sec}{photons/sec} = \frac{current/charge\ of\ one\ electron}{total\ power\ of\ photons/energy\ of\ one\ photon} \quad (1.9)$$

$$IQE = \frac{electrons/sec}{absorbed\ photons/sec} = \frac{EQE}{1-Transmission-Reflection} \quad (1.10)$$

As described above, EQE is dependent on absorption of light and collection of carriers. It has a square shape in the ideal case. However, the real EQE value is reduced because of the carrier recombination and heat generation. EQE plots often provide important clues for determining the loss mechanisms in the device.

## 1.4 Current Photovoltaic Materials and Cell Structures

Since the birth of the first silicon solar cell in Bell Labs in 1954, researchers have studied various semiconductor materials as light absorber and tested different cell structures for higher efficient solar cell and lower cost. The first generation solar cells were single junctions based on wafers of single-crystal (c-Si) or multi-crystalline silicon (mc-Si). These cells are highly efficient and successfully commercialized, but Si has a relatively high price, associated with its indirect bandgap and large material wastage during wafer cutting. A large expenditure of energy in the manufacturing processes limits the further development of Si-based solar cells. The second generation is mainly thin film-based heterojunction cells made with $CuInSe_2$, CdTe, $Cu(In_xGa_{1-x})Se_2$, and $Cu_2ZnSnS_4$. First generation and some of the second generation cells are available commercially. The third generation of cells utilize advanced features. Devices in this category include multi-

junction structures, nanoparticle, dye sensitized, and organic photovoltaic cells. Recently, perovskite solar cells also receive worldwide attention and show great potential as a high efficiency, low cost solar cell choice. Researchers are still optimizing the performance for these second and third generation cells for higher conversion efficiencies and industrial mass-production.

### 1.4.1 Si-Based Solar Cell

The most commonly used semiconductor material is silicon, with its extensive application on chip manufacturing [19-21]. The silicon-based solar cell dominates approximate 90% of the photovoltaic market and is the most developed single junction solar cell in photovoltaic history. Most Si-based solar cells are single crystal Si, but multi-crystalline Si also has a large market share. Amorphous thin film Si has been manufactured, but its market share is declining due to its low efficiency.

Single crystal Si (c-Si) based solar cells have achieved a single junction conversion efficiency of 25.6%, compared with the theoretical maximum efficiency of 30% [1]. After continuous research for about half century, various methods of growing c-Si have been developed. In the Czochralski method of c-Si growth [22], a single-crystal ingot is formed by pulling a single-crystal seed slowly from the high-purity melt. The ingots are then sawed into thin wafers about 200-400 μm thick and then polished, doped, and coated. The process of making the wafer slices which can produce a lot of wastage. This

method is very time consuming and also is limited by its high manufacturing cost, and necessary operating skills for pulling the crystal out from the melt.

Multi-crystalline Si (mc-Si) based solar cells are less efficient than c-Si photovoltaic devices because of the existence of grain boundaries where more deep level traps and defects are found and the flow of electrons is hindered. The energy conversion efficiency for a commercial module made of mc-Si ranges between 10 to 20.8% [1]. Mc-Si solar cells are made from molten silicon poured into a mold container. The container is then cooled and the silicon solidified carefully to form square shaped polycrystalline silicon. There is less wastage of materials and it is a relatively easy and low-cost way of manufacture but is offset by lower cell efficiency.

Amorphous Si (a-Si) was a promising candidate for thin films solar cells compared to c-Si and mc-Si because of its higher absorption coefficient and small thickness required. The band gap of a-Si is near 1.5 eV which is close to the optimal value for theoretical maximum efficiency. A-Si can be deposited by a rather simple and low cost deposition process. Long range order of atoms is not present in a-Si, and the solar cell performance is lower compared to traditional c-Si solar cells. Stabilized efficiencies rarely exceed 12%, making it noncompetitive for most applications.

For c-Si and mc-Si solar cells the main disadvantage is the indirect band gap nature of the material. This requires more photons to provide energy for promotion of electrons from

the valance band. The reduced absorption coefficient requires a thick layer of absorbing materials for effective light absorption. The thicker Si layer can have many recombination sites which in turn can reduce the overall efficiency. In order to reduce these defect sites, Si cells need high purity raw materials and high temperature growth, both of which require more money and effort, as discussed above.

### 1.4.2 III-V Group Material Based Solar Cell

Two common III-V materials for solar cell application are gallium arsenide (GaAs) and indium phosphide (InP). Direct band gap semiconductors, GaAs and InP have same zinc blende crystal structure, similar to that of silicon but with a reduced level of symmetry. Because of its large light absorption coefficient and larger bandgap than Si, GaAs solar cells have higher conversion efficiency with an absorber layer that is only several micrometers thick. The current record conversion efficiency for a GaAs solar cell is about 28.8% and 22.1% for InP crystalline solar cells [1]. The GaAs solar cell is an ideal candidate for concentrator systems because its wide bandgap allows it to operate at higher cell temperatures. Meanwhile, its strong resistance to space radiation damage, lower temperature degradation effect and relative high cell efficiency make it a popular in space applications. The biggest disadvantage of III-V material based solar cells is the cost, thus it is mainly used in concentrator systems where only a small area of cells is needed.

### 1.4.3 Dye-sensitized Solar Cells (DSSC)

The dye-sensitized solar cell (DSSC) has several components including a nanocrystalline semiconductor oxide film electrode, dye sensitizers, electrolytes, a counter electrode and a transparent conducting substrate. When photons are incident on the cell, the dye molecules are photo-excited and an electron is injected onto the conduction band of the semiconductor oxide electrode. Next an electron donated by the electrolyte restores the original state of the dye. The recapture of the conduction band electron by the oxidized dye is prevented by the regeneration of the sensitizer caused by iodide. In return, the iodide is generated by the decrease of tri-iodide at the counter electrode, and the circuit is carried out via electron flow through the external load [23]. As a result, permanent chemical transformation is not required for generating electric power. The breakthrough of dye-sensitized solar cell development was the use of sintered mesoporous titanium dioxide ($TiO_2$) as the dye sensitized material. This produced a successful DSSC with an efficiency of 7.9% [24]. The current conversion efficiency of DSSC is in the range of 10% to 15%. The main limiting factors of DSSC are the instability of the dye and cell degradation [25]. Another disadvantage of DSSC is the usage of a liquid electrolyte which has temperature stability issues [26].

### 1.4.4 Organic Photovoltaic Cells (OPVC)

Typical organic solar cells are planer-layered structured, with an organic absorbing layer and two different electrodes. One of the electrodes must be transparent while the other electrode can be metallic [27]. When incident photons are absorbed by organic material, electrons are excited and injected to the Lowest Unoccupied Molecular Orbit (LUMO) and leaving holes in the Highest Occupied Molecular Orbit (HOMO). Besides the sandwiched structure, a multi-layer cell structure is often used in molecular solar cells. The photo-generation takes place at interfaces between electron donor and acceptor molecule interfaces [28]. One of the primary challenges for OPV is finding a way to efficiently separate the electron hole pairs (excitons) which are more tightly bound than in inorganic materials. As for organic solar cell fabrication, wet solution process and thermal evaporation of organic constituents are two main production techniques that are widely-used today.

Organic solar cells have been studied for several decades. The best achieved conversion efficiency is about 11% reported by Toshiba in 2014 [1]. The low production cost of flexible photovoltaic devices with large area is the biggest driving force of the development of this technology [29]. However, cell conversion efficiency and stability still need to be greatly improved.

### 1.4.5 Thin Film Solar Cells

The manufacture of solar grade silicon wafers is quite expensive and accounted for more than 50% of total cost of silicon solar modules [30] in 2007. Since then the cost of modules has decreased by 2 to 3x. There is not much room for further cost reduction in Si. Furthermore, Si is rigid, making flexible devices extremely difficult. Thin film solar cells are promising for terrestrial and space solar energy applications because of their versatility of device structure design and fabrication techniques [31]. Other than amorphous Si thin film PV, there are three main thin film solar technologies which have been widely studied and even commercialized [32]. There are:

1. Cadmium telluride based solar cells;

2. Copper indium diselenide $CuInSe_2$ (CIS) / copper indium gallium selenide $Cu(In_xGa_{1-x})Se_2$ (CIGS) based thin film solar cells;

3. Copper zinc tin sulfide $Cu_2ZnSnS_4$ (CZTS) based thin film solar cells. (Details in Chapter 2)

#### 1.4.5.1 CdTe thin film solar cells

Cadmium telluride (CdTe) is the dominant thin film alternative to silicon as of this writing. Due to its ability to use thin (~1μm) absorber layers, the cost of CdTe solar modules continues to drop. CdTe has a direct bandgap of ~1.5 eV which is close to the

optimal bandgap of light absorbers for single junction high solar energy conversion efficiency [33]. The high optical absorption coefficient of CdTe as well as its chemical stability make it an attractive photovoltaic material to both academic researchers and industry. The theoretical conversion efficiency limit for CdTe thin film solar cell is reported to be 28% - 30% [34] which is the highest among all the photovoltaic materials known today. Currently, First Solar's top research CdTe solar cell has an efficiency of 21.5%. It shows great opportunity for cell performance improvement through material development and manufacturing process optimization [35].

The most common cell structure of CdTe solar cell is CdS/CdTe heterojunction, which shows very good electrical properties [36]. Even though the typical CdS/CdTe heterojunction structure has been a huge success in industrial mass production, there are still some limiting factors of this technology preventing its reaching the theoretical efficiency [33]:

1. Short minority carrier lifetime caused by the recombination of electron-hole pairs at absorber defect centers and CdS/CdTe interface;
2. Light absorption of transparent conductive oxide (TCO) and CdS window layer;
3. Series resistance between CdTe layer and back contact;
4. P-type CdTe doping instability;
5. CdTe module reliability and long-term degradation concerns;
6. Use of Cd limits sales in Europe and Japan.

CdTe technology is still very likely to continue to develop if it would address the challenges listed above. The CdS/CdTe thin film solar cell will be a major candidate for global low-cost photovoltaic technology in the future.

#### 1.4.5.2 CIS / CIGS Thin Film Solar Cell

Copper indium diselenide $CuInSe_2$ (CIS), with a bandgap of 1.04 eV, is also of great interest for low-cost thin film solar cell application. Due to its high photo absorption coefficient ($>10^4$ $cm^{-1}$) and relative thermal stability in air, CIS was one of the most popular photo absorber materials in the 1980s and 90s [37]. CIS thin film solar cells with conversion efficiency larger than 10% were reported in 1984, and an improvement of efficiency to 17.8% was published in 1990s [38]. Later, researchers found that by replacing indium (In) with gallium (Ga), the material bandgap can be increased continuously from 1.04 eV for CIS to 1.68 eV for $CuGaSe_2$ (CGS) films. The material bandgap can be tuned by partially substitution of Ga for In. Optimal performed solar cells have been fabricated by thin films with a bandgap of about 1.3 eV. These solar cells are commonly known as copper indium gallium selenide $Cu(In_xGa_{1-x})Se_2$ (CIGS) cells [38]. The reported highest CIGS terrestrial cell efficiency is 21.7% from ZSW [1]. Currently, CIGS thin film solar cells on flexible substrates with conversion efficiencies up to 17% [39] are successfully manufactured in industry and will be one of the most promising photovoltaic technologies in the future solar market.

### 1.4.6 Earth Abundant Thin Film Solar Cells: Motivations and Challenges

As the most dominant commercialized thin film PV, CdTe and CIGS cells and modules have limited sustainability in the future because of the scarcity, cost, and toxicity of In, Ga, and Cd elements [40]. Thus, a search for alternatives of non-toxic, inexpensive, and earth-abundant solar materials is indispensable and necessary.

A number of promising earth-abundant PV materials have attracted researchers' attentions, including CZTS, $Zn_3P_2$, $FeS_2$, and $CuSbS_2$, as shown in Table 1.1 [40, 41]. These materials show considerable promise, and especially CZTS, which has reached an efficiency of ~10%, can be considered for commercialization [42]. There are some other promising materials synthesized using earth-abundant constituents, such as SnS, $Cu_2O$, $CuSn_2S_3$ (CTS), and $Cu_2FeSnS_4$ (CFTS) that are still under consideration [40].

**Table 1.1 Figure of merits of CZTS, $Zn_3P_2$, $FeS_2$, and $CuSbS_2$ toward a PV cell complied from the literature [43].**

| **Property** | **CZTS** | **$Zn_3P_2$ [44]** | **$FeS_2$** | **$CuSbS_2$ [41]** |
|---|---|---|---|---|
| **Bandgap (eV)** | 1.5 | 1.5 | 0.95 | 1.38-1.5 |
| **Absorption Coeff. ($cm^{-1}$)** | $> 10^4$ | $> 10^4$ | $3.3\times10^5$ | $> 10^4$ |
| **Electron Diff. Length** | n/a | 4-10 | 0.13-1 | n/a |
| **Dark Resistivity ρ (Ω·cm)** | $1\text{-}39\times10^3$ | $2.5\times10^3$ | 1.43 | n/a |
| **Carrier Mobility μ ($cm^2$/Vs)** | 30 | 450 | 200-300 | 49 |

$Zn_3P_2$ is an important optoelectronic material synthesized from earth abundant elements. It exhibits favorable optoelectronic properties, such as an optimal bandgap of 1.5 eV for PV application, a large optical absorption coefficient ($>10^4$ $cm^{-1}$), a long minority diffusion length for high current collection efficiency [45]. In the early 1980s and 90s, $Zn_3P_2$ was extensively studied [40]. Previous exploration of $Zn_3P_2$ thin film solar cells include Schottky contacts [46], p-n semiconductor heterojunctions [47], and liquid contacts [44]. However, the highest efficiency of $Zn_3P_2$ thin film solar cell was only around 6% [46]. Kimball *et al.* have done research on the influence of magnesium doping on $Zn_3P_2$ thin films [44]. Other researchers successfully synthesized $Zn_3P_2$ in both nanowire and thin film forms [40]. Research on the alternatives for a heterojunction partner material is still ongoing to improve $Zn_3P_2$ PV properties.

$FeS_2$ is non-toxic and also earth-abundant. It has a potential to produce low-cost high efficiency thin film solar cells due to its extremely high optical absorption coefficient ($>10^5$ $cm^{-1}$) and optimal bandgap (0.95 eV) [40]. Since its bandgap is close to Si, the calculated theoretical conversion efficiency of a $FeS_2$ thin film solar cell is close to 30%. The biggest challenge of this technology is creating phase pure iron disulfide. A number of iron sulfides exist in nature with various properties depending on different iron (Fe) to sulfur (S) ratios as well as crystal structures [40]. Only a small trace of sulfides with other phases will significantly reduce $FeS_2$ PV performance. Thus, exploring various pure phase $FeS_2$ synthesis techniques is quite important.

$CuSbS_2$ and $CuBiS_2$ compounds also show very promising optical and electronic properties and are considered as alternatives of thin film photovoltaic absorbers. Welch *et al.* reported an initial $CuSbS_2$ solar cell with about 1% efficiency [48]. The solar cell performance is currently limited by low short-circuit current due to poor collection of photo-excited electrons, and a small open-circuit voltage due to a theoretically predicted conduction band offset between $CuSnS_2$ and CdS [48]. Therefore, it is very critical to understand the fundamental physical properties of these $CuXS_2$ (X=Sb, and Bi) compounds.

Other earth abundant candidates, such as $Cu_2O$, SnS, $MoS_2$, $WS_2$, CTS, and CFTS are also under investigation. Overall, these results illustrate the potential of the development of thin film PV devices with CZTS and other earth-abundant absorbers. Currently, CZTS is considered the most promising thin film material among all the earth abundant PV candidates.

### 1.4.7 Perovskite Thin Film Solar Cell

A new type of solar cells based on mixed organic-inorganic halide perovskites has attracted researchers' attentions recently because of its unprecedentedly rapid development [49]. Perovskites have a crystal structure of $ABX_3$ (X = oxygen, halogen). The fundamental technology for perovskite solar cells is solid-state sensitized solar cells which are based on dye-sensitized photovoltaic technology [50]. Organometallic halide

perovskites were used as visible-light sensitizer for solar cells and reached an efficiency of 3.8% in a $CH_3NH_3PbI_3$-based cell in 2009 [51]. Later, a perovskite quantum-dot-sensitized solar cell with an efficiency of 6.5% was reported [52]. Since the first efficient solid-state perovskite solar cell which was published in 2012, dramatically rapid progress has been made and cell efficiencies have been improved up to 18% in two years [50].

Further improvement of cell performance can be achieved through cell structure modification and material development. Improving the material humidity-resistance and photo-stability is critical to their commercial development [53]. Finally, looking for other elements to substitute Pb is necessary to fabricate environmentally friendly perovskite solar cells [50].

## 1.5 Efficiency Roadmap of Various Solar Cells

The National Renewable Energy Laboratory (NREL) reports a plot of compiled values of highest confirmed conversion efficiencies for various photovoltaic technologies, from 1976 to the present, as shown in Figure 1.3.

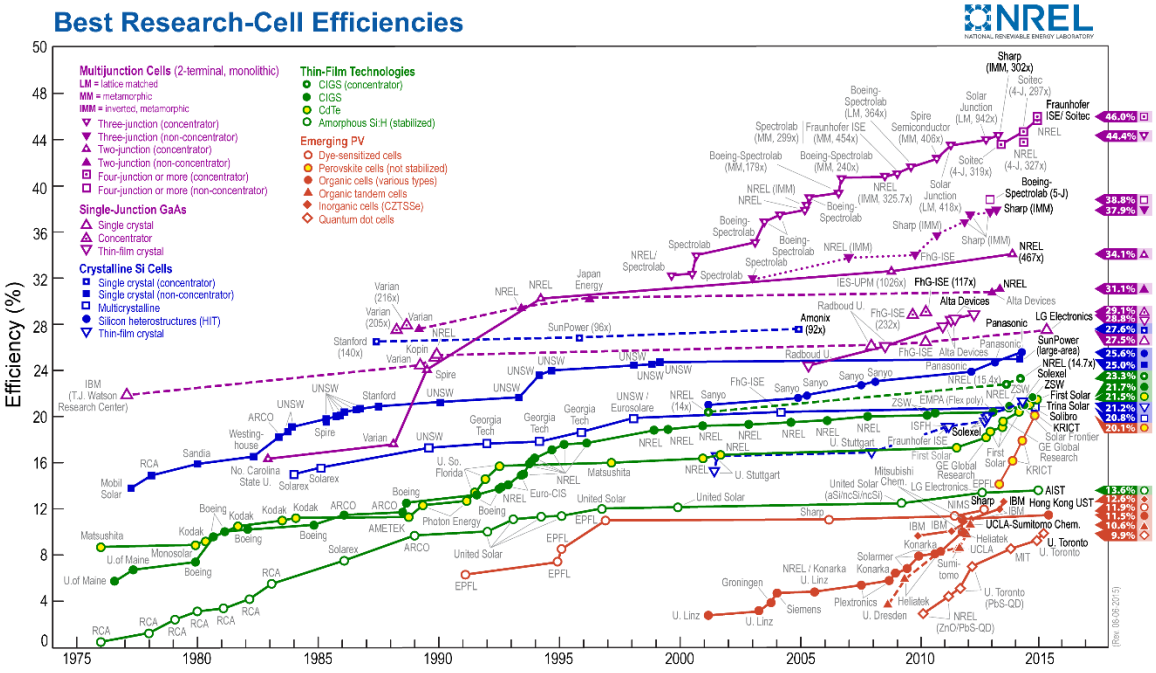


**Figure 1.3 Latest research on solar-cell efficiencies from different institutions. (Source: Department of Energy National Renewable Energy Laboratory)**

Different types of cells are shown, moving toward to their theoretical limit with improved device techniques and manufacturing processes. These are research cell results. Where it exists, manufactured solar modules are typically ~60% of these record small-cell devices.

## 1.6 Vision of This Project and Thesis Overview

This project is mainly focused on the growth of $Cu_2ZnSnS_4$ (CZTS) thin films by post sulfurization of thermally evaporated Cu-Zn-Sn thin film metal precursors, as well as fabrication and characterization of CZTS heterojunction solar cells.

The biggest the challenge for growing CZTS is phase separation and defect formation. Some of the secondary phases alter the properties of the CZTS film in a negative way, such as enhancing recombination or forming insulating regions. For example, copper sulfides and copper tin sulfide ($Cu_2SnS_3$ or CTS) behave like metals. They promote recombination and reduce the current, or even shunt the solar cell [4]. Tin (IV) sulfide ($SnS_2$) is an n-type semiconductor with a band gap of 2.2 eV [54]. Since this is a much wider gap than CZTS, it can act as an insulating phase, degrading electrical transport and limiting the area where electron-hole pairs will form, or in large amounts, could create a diode of opposite polarity to CZTS, forming an electrical barrier [4]. Additionally, the boundary between CZTS and the minority phase are likely to contain defects which can act as recombination centers. Zinc sulfide (ZnS) has a large band gap of 3.5-3.8 eV [55], which makes it also behave like an insulator. One possible crystal structure of zinc sulfide (sphalerite) is similar to that of CZTS, which means they share some peaks in x-ray diffraction (XRD) measurements. Like zinc sulfide, CTS shares peaks with CZTS in XRD measurements, making them difficult to detect [4].

Unfortunately, the energy required to form many defects and secondary phases in CZTS is very small and so they are difficult to avoid. To produce an optimal absorber film and make a photovoltaic device we need to achieve: (1) smooth and uniform films with large grains that are free of voids and cracks; (2) pure CZTS films with no secondary phases; (3) low cost and high efficiency in film deposition; (4) films with the correct carrier

concentration and a low trap density. CZTS thin film growth is optimized from four different aspects:

1. Choice of substrate material;
2. Sulfurization conditions, including sulfurization temperature, time;
3. Thin film metal precursor stacking order;
4. Back contact metal.

In order to improve the efficiency of CZTS-based thin film solar cells, a deeper understanding of the fundamental properties and optimal preparation of CZTS material is important. Even though there is no consensus on which way is the best for the preparation of CZTS thin films [56], the process established here has the potential to promote the development of low-cost CZTS thin film solar cells.

The second part of this work is CZTS thin film solar cell fabrication and characterization. CZTS solar cells we fabricated have a stack structure of Al/Ni/ITO/ZnO/CdS/CZTS/Mo-coated SLG. Current-voltage (I-V) measurement, capacitance-voltage (C-V) measurement and external quantum efficiency (EQE) measurement are usually conducted to test and evaluate the cell performance.

Through C-V measurement results, we have shown that CZTS thin film chemical composition affects its carrier concentration profile, which then influences the solar cell properties. Only a small deviation from the optimal chemical composition can reduce

device performance, which confirms that the CZTS solar cells with high conversion efficiency exist in a relatively narrow composition region. It is also shown that fine tuning the CZTS thin film microstructure morphology and structural properties by adjusting metal precursor stacking order influences solar cell performance.

Various techniques have been used to improve CZTS solar cell performance besides tuning the thin film morphology and chemical composition, such as testing different methods of CZTS synthesis, adjusting the window layer materials and top contact deposition, trying different back contact materials and controlling or modifying material interfaces. As the CZTS cell structure is a carryover from CIGS solar cells, it is convenient to refer CIGS cells when studying CZTS solar cells. Post rapid thermal annealing (RTA) has been investigated in CIGS cells where it has shown a significant increase in device performance while preserving the film composition and microstructure morphology [57]. RTA is usually conducted at high temperatures and fast ramping rate to keep a low thermal budget. It has been widely used to activate dopants while minimizing diffusion in thin film and semiconductor manufacturing industries [57, 58]. Previous researchers have found that post deposition RTA treatment will improve carrier concentration and mobility and then significantly enhance solar cell performance in CIGS [57]. It has also been reported that the use of RTA will remove copper selenide ($Cu_{2-x}Se$) compounds from the surface layer [59]. The motivation of this part of work is to apply

the RTA technique to CZTS thin film solar cells to study the relationship between post RTA conditions, CZTS/CdS interfacial defect concentration and solar cell performance.

In summary, this research could begin to fill the gap between CZTS material development and solar cell performance improvement and link the material properties to CZTS solar cell characteristics. As with all of the theoretical and experimental study on CZTS material and solar cells, this work could help establish a standardized evaluation system with respect to CZTS-based thin film solar cell characterization. Photovoltaic cells and modules are proving to be very promising and a potentially ultimate solution to energy crisis issue and chalcopyrite thin film solar cell technology is generally recognized to be leading in this field.

# Chapter 2

## 2 $Cu_2ZnSnS_4$ (CZTS) Photovoltaic Technology Review

Concerns about the ability of thin film photovoltaics to produce terawatts of energy, since they are currently based on scarce elements, have prompted the search for alternative earth-abundant non-toxic light absorbers. Among the thin film absorbers, copper based I-II-IV-VI semiconductors, especially the direct band gap semiconductor $Cu_2ZnSnS_4$ (CZTS) has attracted considerable interest. CZTS is the $I_2$-II-IV-$VI_4$ quaternary compound semiconductor formed by substituting the selenium with sulfur, the rare metal indium with zinc and tin in a 1:1 ratio in $CuInSe_2$ (CIS) ternary compound [60]. Note that unlike In and Ga in CIGS, Zn and Sn are not isoelectronic. Each has a distinct ideal position in the CZTS lattice. All of the components of CZTS are earth-abundant and have extremely low toxicity [61]. Polycrystalline CZTS films are p-type with a band gap of 1.4-1.5 eV, close to the optimum value for single-junction solar energy conversion. Katagiri *et al.* reported the first CZTS thin film solar cell with an efficiency of 0.66% in 1997 [62]. The best efficiency so far for pure sulfide phase CZTS submodule with antireflection coating is 9.2%, reported by Solar Frontier [42] and 8.4% for a single cell [63]. It was also found that partially replacing sulfur by selenium to form $Cu_2ZnSn(S_xSe_{4-x})$ (CZTSSe) helps to improve solar cell performance [64]. With decades of effort from researchers worldwide, the best performing CZTSSe thin film solar cell was fabricated by solution method with an efficiency of 12.6% from the IBM photovoltaic research group

[65]. Mitzi *et al.* clearly report the importance of the depletion width on the carrier collection efficiency of a cell. Further improvement of solar cell performance is dependent on further increase of open-circuit voltage $V_{oc}$ [65].

## 2.1 CZTS Crystal Structure, Defects, and Secondary Phases

CZTS is a mineral which has been found in nature [66]. It is $I_2$-II-IV-$VI_4$ quaternary semiconductor compound which has the kesterite (space group $I\bar{4}$) and the stannite (space group $I\bar{4}2m$) structures [67] due to the different ordering of Cu and Zn atoms (Figure 2.1). Chen *et al.* conducted first principle calculations and reported that the kesterire structure has a lower energy and should be more stable than the stannite structure [68]. However, the crystal energy of the stannite structure is only slightly higher (2.86 meV/atom) than that of the kesterite structure, which suggests that both forms can coexist [68]. The coexistence of the kesterite and stannite structure might be able to explain the disorder between Cu and Zn sites observed experimentally [69]. The formation of the stannite structure might be one reason for the relatively low open-circuit voltage ($V_{oc}$) found in kesterite solar cells, because the stannite structure is predicted to have a smaller bandgap than the kesterite CZTS [69].

It is relatively difficult to distinguish crystal structure of kesterite CZTS. Since $Cu^+$ and $Zn^{2+}$ are isoelectronic, X-ray diffraction cannot differentiate between the kesterite and stannite structure. A comprehensive neutron diffraction study can be useful, but such

facilities are difficult to access. Raman scattering, which measures molecular vibrational information is used in this project to further identify CZTS crystal structure.

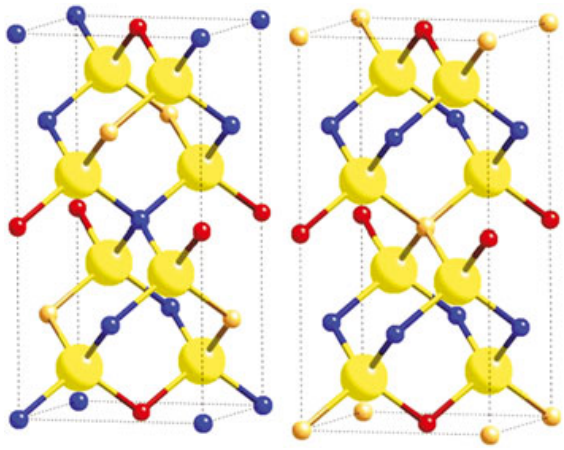

**Figure 2.1 Kesterite (left) and stannite (right) structure of CZTS; large yellow spheres: S and Se; small spheres: blue, Cu; yellow, Zn; red, Sn. Taken from [67].**

Defects will affect the doping level, band structure, recombination properties, and the device performance of solar cells. Similar to chalcopyrite CIGS, kesterite CZTS is also doped by intrinsic defects and has always been reported as p-type [67]. It is well-known that the Cu vacancy ($V_{Cu}$) is the dominant acceptor defect in $CuInSe_2$ and CIGS [70-72]. It is natural to assume if $V_{Cu}$ is also the dominant defect in CZTS.

Chen *et al.* did some nice theoretical work to clarify which defects mainly contribute to the widely-observed p-type conductivity in CZTS [73]. First-principle theoretical calculations of the formation-energy and the transition-energy for several point defects and defect complexes in CZTS were conducted. From their study, the formation of

intrinsic defects is directly related to the chemical composition of the films and the formation of secondary phases (Figure 2.2) [73].

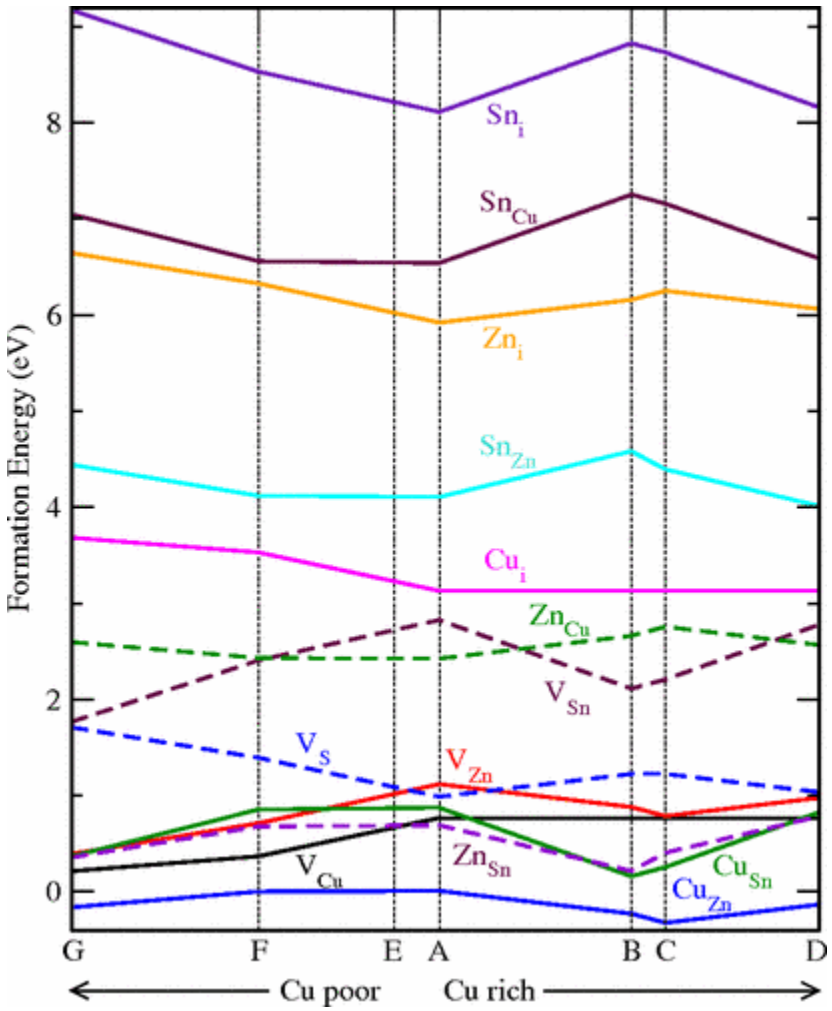


**Figure 2.2 The formation-energy of intrinsic defects in CZTS as a function of Cu atomic composition. A, B, C, D, E, F, G are different chemical potential points in the stable region of CZTS. Taken from [73].**

Being a quaternary semiconductor compound, CZTS has three kinds of cations, giving more possible antisite defects. As shown in Figure 2.2, among all these intrinsic defects,

antisites $Cu_{Zn}$, $Cu_{Sn}$, $Zn_{Sn}$, and vacancy $V_{Cu}$ have lowest formation energies. To be more specific, $Cu_{Zn}$ has the lowest formation energy in both Cu rich and Cu poor composition regions, which means $Cu_{Zn}$ antisite is the dominant intrinsic defect in quaternary CZTS. One of the reasons for this behavior is the small difference in both size and valence of the antisite cations, such as Cu and Zn which are next to each other on the periodic table. The antisite $Cu_{Zn}$ can have a smaller formation energy than $V_{Cu}$. This is different from the behavior of chalcopyrite $CuInSe_2$ and CIGS where the $V_{Cu}$ is the dominant defect. Also, all of the donor defects have higher formation energies, which makes it hard to grow CZTS with n-type conductivity [73].

The passivation of active point defects through forming defect complexes is a common issue in chalcopyrite thin film absorbers. For example, $[2V_{Cu}^{-} + In_{Cu}^{2+}]^0$ in $CuInSe_2$ exhibits an electrically benign character even with high degrees of deviation from stoichiometry and defects density [74]. Similarly, defect complexes can also be found in CZTS thin film absorbers. According to the calculated formation energy of point defects shown in Figure 2.2, $Cu_{Zn}^{-}$, $Cu_{Sn}^{-}$, $Zn_{Sn}^{-}$, $V_{Cu}^{-}$, and $V_{Zn}^{-}$ related defect complexes have lower formation energies and therefore have a higher possibility to exist in the quaternary CZTS system. The researchers also investigated the influence of these defect complexes on CZTS thin film properties and also solar cell performance. It is found that $[Cu_{Zn}^{-} + Zn_{Cu}^{+}]^0$ is the easiest to form because of the smaller chemical and size difference between Cu and Zn. However, the $[V_{Cu}^{-} + Zn_{Cu}^{+}]^0$ defect pair which can be formed under

Zn-rich and Cu-poor conditions proved to be beneficial to maximizing the CZTS solar cell performance [74]. Another reason to choose Zn-rich and Cu-poor condition to grow CZTS thin film for photovoltaics is to suppress the formation of $Cu_{Zn}$ and enhance the formation of $V_{Cu}$ [74].

As a quaternary semiconductor, CZTS is more complex than the common binary simple semiconductors. The increasing number of elements also increases the degrees of chemical composition and structure. It is quite critical to obtain the desired thin film with specific composition and avoid the formation of binary and ternary secondary phases. To be specific, binary compounds such as $Cu_{2-x}S$, ZnS, SnS, $SnS_2$ and ternary phase $Cu_2SnS_3$ are commonly found in CZTS thin films when the film composition varies with various deposition conditions. It is found to be very hard to grow single phase CZTS because of the narrow range of the optimal deposition conditions [73]. As a result, looking for an optimal deposition method for high quality CZTS thin film is quite urgent.

## 2.2 Typical CZTS Synthesis Methods

Since CZTS was first studied by Kentaro *et al.* in 1988 [75], CZTS thin films have been prepared by various methods, including both vacuum and non-vacuum processes. Techniques such as spray pyrolysis [76], e-beam evaporation [62], thermal evaporation [77], sputtering [78], chemical vapor deposition [79], electrochemical deposition [80], screen printing [81, 82], and the sol-gel method [83] have been used. Different kinds of issues arise depending on the deposition method. These include thin film morphology,

crystal structure and electrical and optical properties. For example, Fernandes *et al.* have demonstrated several problems when growing CZTS, such as poor film quality, weak adhesion to back contact metal layer (Molybdenum), and $Cu_{2-x}S$ secondary phase's appearance [84]. Katagiri *et al.* did much of the early work and many of the problems they identified remain as significant barriers to efficient energy conversion [56]. Here major methods of CZTS synthesis and appeared issues are reviewed, as well as the measures that have been taken to improve the CZTS thin film deposition process.

### 2.2.1 Vacuum Techniques

The most common vacuum techniques for CZTS deposition can be sub-classified as sputtering and evaporation. In general, these approaches will provide better uniformity over a large area, easier control of chemical composition of the thin films, and good reproducibility.

Sputtering deposition has been widely used to deposit high quality thin films in both academic research and industry. CZTS thin films can be deposited by two different approaches: a single step co-sputtering process, or a two-step process with a deposition of either metallic precursors Cu/Zn/Cu or metal sulfide precursors Cu/ZnS/SnS and an ex-situ sulfurization process.

In 1988, Ito and Nakazawa published the first synthesis of CZTS by sputtering [75]. In this method, a target which was composed of a synthesized powder of all the elements in

the quaternary compound was sputtered. The film showed a light absorption coefficient larger than $1\times10^4$ $cm^{-1}$ in the visible range and a bandgap around 1.45 eV. A heterojunction diode which was fabricated using this CZTS thin film showed an open circuit voltage of 165 mV under AM1.5 illumination [75]. However, the sputtering of a quaternary compound target suffers from difficulty in controlling the film's chemical composition and its electrical and optical properties. Later, Kyoo-Ho Kim *et al.* tried to use a cold-compressed sputtering target composed of finely mixed $Cu_2S$, ZnS and $SnS_2$ for CZTS deposition [85]. It was possible to control the CZTS film composition by tuning the atomic ratio of the sulfides. In order to achieve a more precise control of CZTS chemical composition, a suitable CZTS deposition technique was required. In 2005, Tanaka and Ogawa *et al.* [86] reported a two-step deposition with a sequential sputtering of metal elements and a post annealing in a sulfur-containing atmosphere. This technique was utilized to obtain CZTS thin films with good optical and electrical properties. Previously, the metallic precursor deposition vacuum was separated from the post-annealing chamber, and precursors suffered from being oxidized and contaminated by the air [87]. Katagiri *et al.* proposed an inline-type vacuum apparatus for three RF sources co-sputtering and vapor phase sulfurization. By optimizing CZTS deposition and film compositional ratio, an efficiency of 5.74% was obtained [87]. In 2011, Katagiri and Jimbo *et al.* [88] prepared a CZTS compound target with the preferable composition for a single sputtering followed by sulfurization. A solar cell with an efficiency of 6.48% was achieved in this study. Single sputtering of a quaternary compound target has been

studied rigorously to reduce the manufacturing cost, but further efforts will be needed to improve device performance [89-91].

Among conventional vacuum deposition techniques, sputtering has many advantages such as precise control of film composition, less contamination from the vacuum chamber, high uniformity of film morphology, and convenience for large scale film deposition [60]. Sputtering is currently one of the most promising techniques for CZTS thin film deposition. However, there are also some drawbacks for the sputtering method.

Evaporation techniques are being used to deposit CZTS thin film absorbers due to its good control of film chemical composition and convenience to operate. Various evaporation techniques can be employed for the deposition of CZTS thin films, such as electron beam (E-B) evaporation, co-evaporation, and thermal evaporation [77, 92-94]. Similarly to the sputtering technique, CZTS thin films are evaporated by two different approaches: (i) a single step simultaneous deposition of all precursors followed by annealing; (ii) a two-step process with sequential deposition of metallic precursors Cu/Zn/Sn or Cu/ZnS/SnS and an ex-situ sulfurization. A similar approach to that used in sputtering is used for the sulfurization of deposited precursors by evaporation, but with varying sulfurization temperature and time durations.

Katagiri *et al.* synthesized CZTS thin films by using sulfurization of E-B evaporated metallic precursors in 1997 [62], and a solar cell was fabricated with a structure of

Al/ZnO/CdS/CZTS/Mo/SLG substrate. An open circuit voltage of 400 mV was obtained, however the conversion efficiency was very low (0.66%) [62]. Later, CZTS thin films were successfully synthesized by sulfurization of E-B evaporated stacked metallic precursors, as reported by Araki *et al.* [92]. Six precursors with different stacking orders were tested and the best conversion efficiency 1.79% was obtained in cells with a stacking order of Mo/Zn/Cu/Sn [92]. Wang and Mitzi *et al.* carried out detailed studies on film microstructure, secondary phases and grain boundary properties of CZTS thin films deposited by sulfurization of thermal-evaporated metallic precursors [95]. The importance of controlling the precursor composition and the stoichiometry of CZTS films to achieve better solar cell performance was emphasized. Co-evaporation has also been investigated to synthesize CZTS thin films for photovoltaic applications but further study is required to obtain higher conversion efficiency [96, 97].

### 2.2.2 Non-vacuum Techniques

For the past few decades, CZTS thin films have been successfully deposited mostly by vacuum deposition techniques. However, vacuum techniques suffer from a high deposition cost, high energy consumption, and low material utilization. Researchers have begun to search for cheaper ways to grow CZTS thin films. The majority of non-vacuum techniques, such as spray pyrolysis deposition, electrochemical deposition, sol-gel deposition, ink-based deposition, and solution-based deposition, offer simple, low cost deposition of uniform CZTS thin films.

Spray pyrolysis deposition is widely used to deposit thin films due to its easy handling and simplicity in fabrication [98]. Researchers have tried to deposit CZTS thin films using this method due to its advantages such as good reproducibility on large scale and ease of scaling to industrial applications [81]. The experimental procedure of spray pyrolysis is simple and easy to operate, and high-cost vacuum and gas protection equipment are not required. Rezig *et al.* investigated spray pyrolysis deposition conditions to optimize CZTS thin film properties for solar cell fabrication [98]. CZTS was synthesized by spraying of copper chloride ($CuCl_2$), zinc chloride ($ZnCl_2$), tin chloride ($SnCl_2$) aqueous solutions and thiourea on heated glass substrates at various temperatures. Based on their experimental results, CZTS thin films achieve better optical properties if the substrate temperature is controlled between 500 $^oC$ and 650 $^oC$ in pyrolysis [98].

Electrochemical deposition is a widely-used technique for the low cost deposition of various semiconductor thin films in both small scale research and large scale industrial applications. CZTS thin films have been deposited using two different approaches: a single step electrochemical deposition followed by annealing, or sequential electroplating of metallic precursors and an *ex-situ* sulfurization. It was reported that 8% efficiency CZTS thin film solar cells were successfully fabricated by electrochemical deposited metallic precursors followed by a post sulfurization [99]. A preheating treatment of precursors before the high temperature sulfurization was found to be beneficial to obtain

final high quality CZTS thin films [99]. Electrodeposition is a low temperature process without residual thermal stress between thin films and substrates. Because it is a solution-based deposition technique, good interface bonding and better uniformity over various surfaces can be obtained. Also, film thickness, chemical composition, crystalline structure and porosity can be precisely controlled [100].

The sol-gel based spin coating technique is a very simple, low cost method of preparing different semiconductor thin films. This technique basically involves the preparation of sol-gel precursor, and then spin coating of precursor solution on the substrate to form thin films. As it is well developed in industry, this type of direct liquid deposition approach including solution, particle and mixed particle-solution precursors is of great interest for large area manufacturing [83, 101]. Tanaka *et al.* published a sol-gel method of using dimethyl alcohol as the solvent and the ethanolamine as the stabilizer to make sol gel with cupric acetate, zinc acetate, and tin chloride ($SnCl_2$). Spin coating was repeated 5 times and the sample was annealed at 300 $^oC$ for 5 minutes in the air and then at 500 $^oC$ for an hour in an atmosphere of 5% $H_2S$ in $N_2$ to form CZTS [102]. Later, CZTS thin film solar cells with an efficiency of 1.01% were obtained by improving the approach [103]. Tanaka *et al.* achieved CZTS solar cell with an efficiency of 2.03% by optimizing film composition in 2011 [104]. Todorov and Mitzi *et al.* published a device with an efficiency of 9.6% by spin-coating a hydrazine solution in 2010 [105].

Similar to other solution-based deposition techniques, the sol-gel method requires very simple process equipment without vacuum conditions. It is also convenient to deposit uniform thin films over large areas with effectively controlled film composition and microstructure. However there are also some drawbacks such as the high price and probable toxicity of organic raw materials, and the long process time usually needed for sol gel deposition [83].

## 2.3 Introduction to CZTS / CdS Solar Cells

The most widely studied CZTS thin film solar cell is made from a stack structure of Al/Ni/ITO/zinc oxide (ZnO)/cadmium sulfide (CdS)/CZTS/Molybdenum-coated (Mo-coated) soda-lime glass (SLG). This sequence is a carryover from CIGS solar cells. As a result, it is convenient to refer to CIGS cells when studying CZTS solar cells.

### 2.3.1 Substrates

Substrates have a strong influence on deposited material growth and properties, since various substrate characteristics, such as surface roughness, substrate composition, thermal expansion and stability, can be taken into consideration [106]. Reducing material and manufacturing cost, and the requirements of the intended application are other reasons that lead to optimal substrate choices. For example, soda-lime glass (SLG) is one of the most widely-used substrate for CIGS and CZTS thin film solar cells in the lab.

However, flexible polymer and metals are more popular in industrial manufacture for large area PV modules and applications such as building integrated PV [106].

SLG is chosen as almost an ideal substrate for CIGS thin film solar cells for several reasons. SLG has lower price and relatively high sodium (Na) composition which provides Na to the CIGS/CZTS films by thermal diffusion during crystal growth. It is widely reported that Na diffusion is beneficial to CIGS grain growth as well as the solar cell performance [106-111]. Based on a study on Na diffusion and its effects, Yun *et al.* reported that a thick layer of Na/Mo can be deposited on stainless steel to provide extra Na for CIGS absorber growth for large scale manufacture of high efficiency CIGS solar cells on a flexible substrate [112]. With the extra Na layer, lower leakage current of the absorber was observed.

Due to the success of SLG in CIGS thin film solar cells, SLG has also been used as the most common substrate in CZTS solar cells [56, 84, 92, 93, 113, 114]. The effect of SLG on CZTS grain growth and solar cell performance will be discussed later in this thesis.

### 2.3.2 The Window Layer

The buffer layer in a heterojunction thin film solar cell is primarily used to form a p-n junction with the absorber layer. It should be thin and wide gap to admit a maximum amount of light to the junction region and absorber layer [31]. To improve solar energy conversion efficiency, this layer should also have minimal recombination losses to drive

out the maximum number of photo-generated carriers, and a minimum of electrical resistance to maximize the fill factor. Therefore, window layer with higher bandgap and smaller thickness is desired for high optical throughput and low series resistance [31]. It is also important to minimize the potential ‘spike’ in the conduction band at the heterojunction for optimal minority carrier transport.

The CZTS thin film solar cells typically use a chemical bath deposited (CBD) CdS window layer. It is reported that CdS deposited by CBD surpasses that deposited by a physical vapor deposition (PVD) technique, for providing a superior device performance [115]. One of the reasons is due to the enhancement in the interface chemistry between light absorber and window layer during the CBD process. As in CIGS technology, there are multiple effects. The chemical bath removes the natural oxides from the absorber film surface. Meanwhile, Cd diffuses into the Cu-poor surface layer of the CIGS thin films [116]. There are indications that Cu diffuses out of the absorber during CBD increasing the vacancy concentration. Cd is also believed to diffuse into the absorber surface and, at least in CIGS, may act as a donor, changing the band bending near the interface. The other reason that CBD films may be preferred is the step coverage of the film, which is very nearly conformal. This permits the deposition of thinner CdS layer which provides good surface coverage over the rough polycrystalline CIGS films [117, 118]. These benefits all apply to Cu-poor CZTS thin film solar cell fabrication as well.

CdS has a relatively small bandgap (2.4 eV). This is responsible for the decreased blue response in EQE spectrum [119]. This effect can be reduced by using thinner CdS films. Alternatively, it is also applicable to mitigate the effect and improve optical transmission by switching to a wider bandgap window layer such as $Cd_{1-x}Zn_xS$ [120-122]. With the doping of Zn, $Cd_{1-x}Zn_xS$ has a larger bandgap but also a higher resistivity. As a result, it is possible to optimize the Zn compositional ratio, optical transmission, resistivity and film thickness of the window layer by tuning the chemical precursors and CBD deposition conditions and obtain higher solar cell performance [122].

Considering the toxicity of Cd, several environmentally friendly wide-bandgap window layer candidates such as ZnS and ZnS(O, OH) ($E_g$ = 3.7 eV) are currently being investigated to replace CdS [119, 123]. To better integrate the heterojunction formation into in-line fabrication process, much research work has been done to replace the CBD deposition by a PVD process [119, 124, 125]. However, the CBD-ZnS/CZTS thin film solar cell has a conversion efficiency of 5.82% [126], while an efficiency of only about 2% was achieved for the PVD-ZnS/CZTS solar cell [119] which is much lower than the best CdS/CZTS devices. Further study is required on the development of a Cd-free window layer for CZTS thin film solar cells.

### 2.3.3 Back contact

Molybdenum (Mo) is the “historical” back contact choice for both CIGS and CZTS thin film solar cells. The most important requirements of a good back contact material are [127]: (i) it can form a low-resistance contact with the absorber layer; (ii) the contact should be non-rectifying; (iii) the contact should be stable under low term worst-case use conditions. Other requirements include good adhesion to both the substrate and the absorber, low film stress, high optical reflectance and high stability during post high temperature absorber growth process [114].

Based on these fundamental qualifications, many metals have been tested as potential back contact candidates for CIGS thin film photovoltaics technology [127], including tungsten (W), Molybdenum (Mo), Chromium (Cr), Tantalum (Ta), Niobium (Nb), Vanadium (V), Titanium (Ti), and Manganese (Mn). Even though it shows a very high optical reflection, Ag cannot be utilized directly as back contact because of its high mobility in CIGS. The analysis of absorber materials and solar cell performance shows that only W, Mo, Ta and Nb are inert during CIGS deposition [127]. While this may be somewhat different in CZTS, there four would have to be considered as leading candidates.

Currently, Mo is the most widely used back contact material for CZTS thin film photovoltaics in view of the previous study on CIGS devices. Sputtering is commonly

used to deposit Mo thin films on the SLG substrate. In order to achieve an adhesive and low resistive back contact layer with low stress, a bi-layer Mo deposition was proposed [128]. In this thesis, a detailed demonstration of bi-layer Mo deposition will be emphasized and its beneficial influence on CZTS thin film solar cell performance will also be discussed. Other than Mo, several other metal materials are tested for the candidacy as back contact materials for CZTS photovoltaic technology as well.

### 2.3.4 Interfaces

Two critical interfaces in CZTS thin film PV technology are the back interface between Mo back contact and CZTS absorber and the interfacial layer (p-n interface) between CZTS absorber layer and CdS window layer. For most solar cells, device performance is strongly influenced by these two interfaces.

This brings us to a discussion of Mo/CZTS interfacial layer and the formation of $MoS_2$ during CZTS growth. In this project, CZTS is deposited using a two-step processing, ie, the deposition of metallic precursors followed by a post sulfurization process. The reason for doing an *ex-situ* sulfurization is that high sulfur (S) partial pressure and high temperature is required to suppress the decomposition reaction of CZTS that may occur during the growth [114]. However, another decomposition process has been investigated between CZTS absorber layer and back contact Mo during sulfurization [114]:

$$2Cu_2ZnSnS_4 + Mo \xrightarrow{High\ Temp} 2Cu_2S + 2ZnS + 2SnS + MoS_2 \qquad (2.1)\ [129]$$

$$2SnS_2 + Mo \xrightarrow{High\ Temp} 2SnS + MoS_2 \quad (2.2)\ [130]$$

$$Mo + S_2 \xrightarrow{High\ Temp} MoS_2 \quad (2.3)\ [130]$$

The majority of $MoS_2$ exists in hexagonal crystalline form which has a "sandwich" crystal structure with one planar hexagonal layer of Mo atoms interspersing between two layers of S atoms [131]. Such $MoS_2$ layer could influence not only the electrical properties of the contact, but also the adhesion of CZTS thin film to Mo back contact layer.

The reactions shown above can be self-limiting if the accumulation of reaction products at the interface creates a battier to further reaction. As a result, it is suggested that a high temperature and an external pressure of S vapor can be used to suppress further reactions between CZTS and Mo layer by the rapid formation of $MoS_2$. An inert layer can be deposited between CZTS and Mo layer to prevent rigorous chemical reaction at the interface. As was previously reported [114], a TiN barrier layer was utilized to passivate interface reaction between Mo and CZTS layer, and Na transport from the substrate was not influenced. The drawback of this technique is the high series resistance of TiN/CZTS contact. Therefore, further study is needed to develop low resistive inert back contacts. Then more flexible and less complicated CZTS synthesis methods by using lower chalcogen pressures can be achieved.

As for the interfacial layer between the CZTS absorber and the CdS window layer where the defects and deep-level traps need to be minimized to reduce the interfacial recombination [132]. The interfacial properties are largely dependent on the CdS deposition techniques. A deficit of open-circuit voltage ($V_{oc}$) of the PVD-CdS CIGS solar cells was observed, and this was attributed to defects created by a large lattice mismatch between CIGS and CdS [133]. While, the CBD-CdS/CIGS interface was found to be less abrupt due to Cu diffusion into CdS layer as well as the Cd incorporation into the absorber layer. This inter-diffusion leads to an inversion of the CIGS surface and then a decrease in interfacial recombination [134]. It was also observed in CZTS thin film solar cells that a Cd and Zn diffusion taking place at the CBD-CdS/CZTS interface [135, 136]. Thus, one could argue that a higher $V_{oc}$ is attributed to a better junction formation at the CBD-CdS/CZTS interface.

Other than optimizing the CdS/CZTS interface by choosing CBD deposition techniques, some other approaches have been investigated as well. For example, selective chemical etching of the absorber prior to CdS deposition to minimize the interfacial defects was studied [137]. Also, post rapid thermal annealing was conducted for complete CIGS thin film solar cells [57, 59] and an improvement of interfacial properties and device performance was observed. These approaches will be discussed in details in the following section.

## 2.4 Improving CZTS thin films and device performance

### 2.4.1 Alkali metal doping

The significance of sodium (Na) incorporation into CIGS absorber thin films was first reported by Hedstrom and his co-workers in 1993 [138]. Since then, Na diffusion and its effects on CIGS film properties and device performance has attracted attention from the researchers world-wide. Nataka *et al.* showed that Na diffusion was beneficial to CIGS grain growth, increasing hole concentration, and then improving $V_{oc}$ and solar cell performance [111]. Most often Na was introduced into CIGS thin films by diffusion from the SLG substrate through the Mo back contact layer. In some studies, NaF and NaOH were also investigated as post-deposition Na sources [139] and similar solar cell efficiency enhancement was observed. This Na-containing layer is necessary for improving CIGS photovoltaic device performance on a Na-free flexible substrates in large-scale manufacturing.

Based on the wealth of observations [110, 111, 139, 140] of the beneficial effects of Na, experiments were also conducted to verify the Na influence on CZTS thin films and solar cell performance [109, 141-143]. Aydil *et al.* [109] studied the composition and microstructure of CZTS thin films synthesized on SLG and Na-free substrates. It was found that Na and K diffusing from SLG facilitated CZTS grain growth. Also, a method for delivering precisely controlled amount of Na and K to CZTS thin films was proposed

[109]. Other than its profound influence on CZTS grain growth and crystal structure, Na at the grain boundaries in CZTS can passivate donors and deep defects, thereby reducing recombination [144]. This normally shows as an increase of $V_{oc}$ and the fill factor (FF).

### 2.4.2 Absorber chemical composition tuning

Although the CZTS thin film solar cell development has been promising, Shockley and Queisser predicted 32.2% the theoretical limit of the solar cell efficiency [14]. Absorber layer quality is one of the most critical points for obtaining high performance solar cell, which can be mostly affected by thin film composition, secondary phases, and defect concentration [145]. It has been widely observed [104, 146-148] that the best CZTS thin film solar cell performance can be achieved from a slightly Zn-rich/Cu-poor absorber layer. An excessively Zn-rich precursor will lead to a lower quality CZTS absorber with a ZnS secondary phase, which is responsible for a sharply reduced solar cell efficiency [145].

The influence of the CZTS compositional ratio on the film structural, optical and electrical properties was rigorously studied [145]. Normally, the presence of the ZnS phase is due to the high Zn/Cu atomic ratio, while $Cu_{2-x}S$ and ternary sulfide $Cu_2SnS_3$ are the major impurities under Cu-rich deposition conditions [73]. The existence of these secondary phases might be also responsible for the decrease of electron mobility, which is probably due to the increased scattering factor at the grain boundaries between CZTS

and secondary phase grains [149]. What's more, the existence of metallic Cu-rich secondary phases can reduce the CZTS resistivity and cause recombination which is detrimental for making solar cells. As for the optical transmission of CZTS thin films, a slight decrease in the transmission was observed in CZTS samples with higher Cu/(Zn+Sn) ratios [145]. This is probably due to the increase of CZTS film roughness under Cu-rich deposition conditions.

The electrical properties of the CZTS thin films were measured using the Van der Pauw method [145]. As mentioned earlier, the p-type conductivity of CZTS is attributed to acceptor defects, the copper vacancy ($V_{Cu}$) vacancy and the copper-zinc antisite ($Cu_{Zn}$). These point defects have very low formation energy which leads to the large difficulty of making n-type CZTS [73]. CZTS thin films with a Zn-rich/Cu-poor composition tends to form $V_{Cu}$ and $Zn_{Cu}$ point defects and defect clusters of $[V_{Cu}^{-} + Zn_{Cu}^{+}]^{0}$ and $[Zn_{Sn}^{-} + Zn_{Cu}^{+}]^{0}$. On the other hand, $Cu_{Zn}$ defect is more preferentially formed in CZTS films with a higher Cu/Zn ratio. The carrier concentration thus increases with Cu rich films because $Cu_{Zn}$ defect has a lower formation energy than $V_{Cu}$ and then is easier to form. The Zn-rich/Cu-poor composition is preferred for high efficiency solar cells because of the beneficial effects of defect cluster $[V_{Cu}^{-} + Zn_{Cu}^{+}]^{0}$, which can help to separate electron-hole pairs [74]. In order to achieve a better understanding of the properties of the defects in CZTS thin films, the carrier concentration profile was measured using C-V measurement as discussed in Chapter 5.

### 2.4.3 Absorber selective etching

One approach to the improvement of CZTS thin film solar cells is developing specific procedures to minimize or avoid the formation of detrimental secondary phases, especially the ZnS secondary phase favored by Zn-rich/Cu-poor device-grade absorber deposition conditions [137]. One needs to develop a selective etching technique to remove Zn-rich secondary phases from the CZTS surface. Katagiri *et al.* [150] first reported the preferential etching effect of deionized water (DIW) soaking which eliminated the metal oxide and sulfide particles and improved the solar cell performance. However, no sound theoretical explanation of DIW soaking effect has been published so far. Other than classical KCN etch that removes Cu-rich secondary phases [137], more environmentally friendly and less toxic HCl-based and $H_2SO_4$-based chemical etching techniques were utilized to lower Zn-rich phases [137, 151]. A significant improvement of conversion efficiency of the devices was observed as well as the solar cell optoelectronic properties. Due to the current-blocking effect of Zn-rich secondary phases, selective etching of ZnS surface phase directly enhances short-circuit current density ($J_{sc}$) and series resistance ($R_s$). Also, an improvement of $V_{oc}$ and FF are related to an absorber surface passivation effect which chemical solution process brings [151]. Nonradiative-recombination states can be reduced by chemical solution process and then p-n junction properties can be improved.

### 2.4.4 Post deposition rapid thermal annealing (RTA)

Since CZTS/CdS interfacial properties are critical to CZTS thin film solar cell performance, it is quite important to develop techniques for improving the interface of these heterojunction devices. Besides selective etching, post deposition rapid thermal annealing (RTA) has also been verified as an alternative. Mostly, RTA was done on CIGS solar cells. Its beneficial influence on CZTS thin film solar cells will be discussed in Chapter 6.

RTA is generally conducted on completed CIGS thin film solar cells between 250 $^{o}$C to 400 $^{o}$C for seconds. It proved to improve photovoltaic performance and yield a higher conversion efficiency [57, 59]. Konogai *et al.* discussed the removal of $Cu_{2-x}Se$ compounds from surface layer during RTA process which may lead to the solar cell performance improvement [59]. Later, Anderson *et al.* reported their AMPS-1D numerical simulation of RTA process with different peak annealing temperatures and holding times [57]. It was found that optimal RTA would enhance the CIGS electrical properties while preserving CIGS film compositions and microstructure morphology. The defect density in the CIGS absorber was reduced by RTA, and hence the light I-V, dark I-V and spectral response of the cell was improved. However, no strong correlation between defect density and FF was observed.

As for the explanations of the beneficial effects of RTA on CIGS thin film solar cells, there is no consensus. This means that the causes of the photovoltaic performance improvement are probably on a smaller scale than the resolution of these techniques and could be, for example, the removal of very finely distributed secondary phases, changes in grain boundaries, or of course, reducing the point defect density. Despite these unknowns, this study enabled us to identify routes to improving material and device quality, as well as providing some direction for further studies of loss mechanisms in CZTS solar cells. RTA treatment was also conducted on CZTS thin film solar cells in this project and will be discussed in detail later.

# Chapter 3

# 3 Experimental Techniques

## 3.1 Characterization of CZTS Thin Films

### 3.1.1 Structural Characterization

X-ray diffraction and Raman scattering spectroscopy are the two methods most often used to identify CZTS crystalline structure. CZTS is a line compound between $Cu_2SnS_3$ and ZnS and theoretically even a 2-3% compositional variation could lead to a phase separation [152]. Given that the primary XRD peaks of $Cu_2SnS_3$ and ZnS secondary phases and kesterite CZTS overlap, it is very hard to identify those secondary phases by XRD and therefore kesterite CZTS structural characterization is challenging. Raman scattering spectroscopy has been widely used to distinguish these secondary phases and pure kesterite CZTS [84].

#### 3.1.1.1 X-ray Diffraction

X-ray diffraction has long been used to deal with issues related to the crystal structure of materials, such as lattice type and lattice constants, defects and stress, orientation of single crystals, preferred orientation and grain size of polycrystalline materials, and identification of unknown materials [153]. The x-ray diffraction technique is non-

destructive and does not demand elaborate sample preparation. These two major advantages make it widely used in material structural characterization.

The basic theory of this technique can be derived from Bragg's law. When an x-ray interacts with a single atom, it scatters the incident beam in all directions. However, when a beam interacts with a material and the net effect is the sum of the individual scattered beams. These can add together in a few directions to create high intensity spot. Bragg's law states the conditions for this constructive interference (Fig. 3.1):

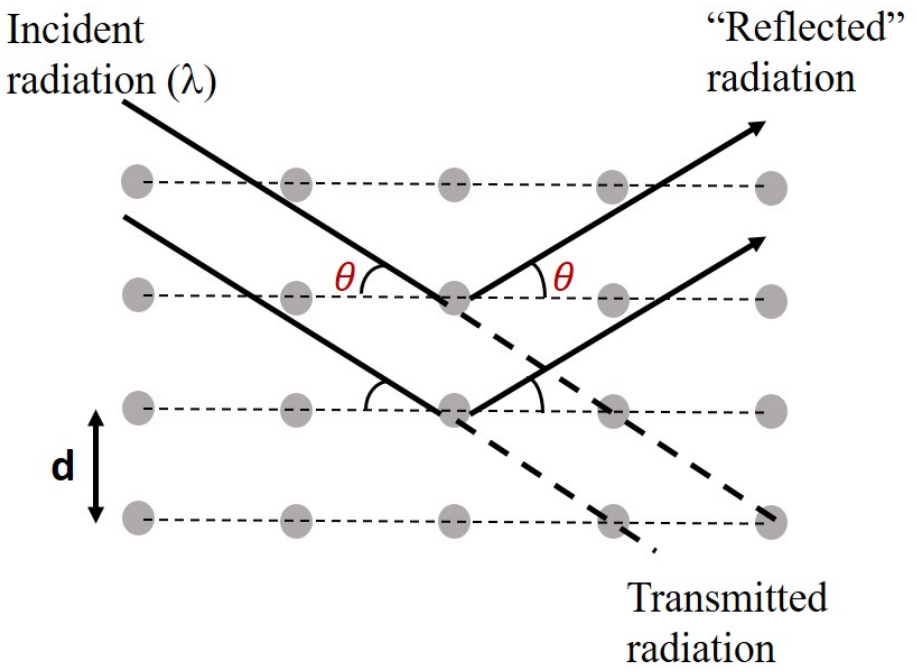


**Figure 3.1 Basic theory of X-ray diffraction.**

$$n\lambda = d \sin\theta, \tag{3.1}$$

where n = the order of diffraction, usually n = 1

$\lambda$ = the wavelength of x-ray

d = the inter planar spacing

$\theta$ = the Bragg angle

The crystal structure of CZTS thin films was examined using a Bruker-AXS micro-diffractometer with a 2.2 kW Cu ($\lambda$ = 1.54 Å) X-ray source and a two-dimensional detector. Two dimensional X-ray diffraction patterns were converted to a one dimensional intensity versus 2$\theta$ data set. This data set including the X-ray diffraction peak positions and relative intensities was analyzed and compared to Powder Diffraction File (PDF) reference, a database of X-ray powder diffraction patterns maintained by the International Center for Diffraction Data (ICDD), to obtain the phase of specific materials.

X-rays have great penetrating power and sometimes, with specific incident angles, their path length through films is too short to produce diffracted beams of sufficient intensity. Under such circumstances the substrate, rather than the film, dominates the scattered X-ray signal. As a result, longer counting times are usually needed to generate better diffraction patterns.

#### 3.1.1.2 Raman Scattering Spectroscopy

Raman scattering spectroscopy is commonly used as a supportive technique for X-ray diffraction method to identify kesterite CZTS [84, 154]. This technique is basically measuring the vibrational energies of molecules or solids, so it is very convenient and efficient to identify the secondary phases in CZTS thin films. Two-dimensional and depth profiles can also be measured to investigate the phase distributions in the samples.

When photons interact with molecular systems, most are elastically scattered, a process which is called Rayleigh scattering. In Rayleigh scattering, the scattered photon has the same wavelength (energy) as the incident photon. Raman scattering is based on the Raman Effect, the inelastic scattering of photons by molecules. Raman spectroscopy detects the molecular deformation of materials caused by inelastic scattering of incident monochromatic light, usually from a laser. Photons of the laser light are absorbed by the sample and then reemitted. The frequency of the reemitted photons is shifted up or down compared to the original monochromatic frequency. This is called the Anti-stokes or Stokes scattering. This shift provides information about vibrational, rotational and other low frequency transitions in molecules. However, elastic Rayleigh scattering is the dominant effect and typically only one in $10^7$ photons is scattered inelastically. This typically leads to a very weak spontaneous Raman scattering signal, as shown in Figure 3.2.

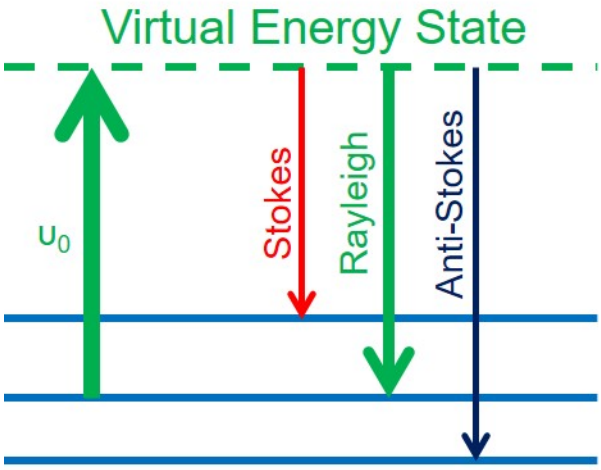


**Figure 3.2 Energy-level diagram showing the states involved in Raman signal. The line thickness is meant to the signal strength from the different transitions.**

We observe the presence of CZTS with a preferential growth orientation of (112) from the XRD pattern, however the results cannot rule out the existence of binary chalcogenides such as ZnS and $Cu_{2-x}S$. Under such conditions, the presence of CZTS can be confirmed by Raman scattering peaks at 337-338 $cm^{-1}$, 282-288 $cm^{-1}$, and 367-372 $cm^{-1}$ which was published for monogains of CZTS [155]. It has been shown that a Raman scattering peak at 476 $cm^{-1}$ is related to $Cu_{2-x}S$, while a shoulder at 255 $cm^{-1}$ is due to the convolution of peaks corresponding to $Sn_2S_3$, CZTS, $Cu_{2-x}S$, and ZnS [84, 154, 156]. Meanwhile, ZnS is associated with Raman peak located at 348-352 $cm^{-1}$ [156].

Due to the small energy barrier between kesterite (space group $I\bar{4}$) and stannite (space group $I\bar{4}2m$) CZTS, it is rather difficult to obtain pure kesterite CZTS and normally these two phases will co-exist. The presence of the stannite phase is reflected in the appearance

of a dominant broadened Raman peak at lower frequency (~ 331 $cm^{-1}$) than the main Raman peak of kesterite at 337 $cm^{-1}$[154].

### 3.1.2 Film Microstructure and Chemical Composition

There are several hierarchies of thin film information that are of interest to researchers [157]: (i) metrology of patterned films [20], such as lateral or depth dimensions and tolerances, uniformity of thickness, uniformity of coverage, and completeness of etching; (ii) film surface topography and microstructure, including grain size and shape, the existence of compounds, presence of hillocks or whiskers, evidence of film voids, micro-cracking, or lack of adhesion, etc; (iii) cross-section views of multilayer structures exposing interfacial regions, columnar grain morphology, and substrate interactions; (iv) structural information such as defects in films, structure of the grain boundaries, identification of phases; (v) Details of film-nucleation and growth processes.

Scanning electron microscopy (SEM) is generally used to analyze the first three levels of information in thin film characterization. Unlike transmission electron microscopy (TEM), which is a true microscope and all the image information in the field is acquired simultaneously, SEM probes a small portion of the total image at a time and the image is built up serially by scanning the probe [157]. Upon impinging on the sample, the high energy electrons decelerate and transfer energy inelastically to other atomic electrons and to the lattice. Through continuous random scattering events, the primary electron beam

effectively spreads and fills a “tear-drop-shaped” interaction volume with several absorption and emission processes, as shown in Figure 3.3.

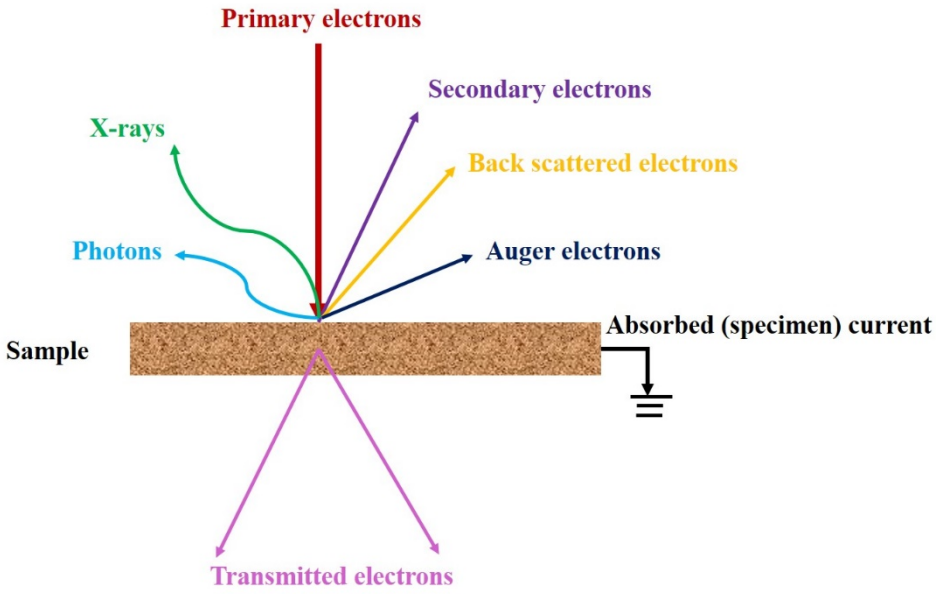


**Figure 3.3 Schematic representation of the electron-sample interaction in a SEM and various signals are generated.**

The secondary electrons (SE) and back scattered electrons (BSE) are used to generate the sample image. The SEs are ejected from the outer shell of the sample atoms and are the lowest portion of the emitted energy distribution. The depth from which SEs escape the sample is usually between 5 to 50 nm due to their low energy. The SEs are also generated by the BSEs as they escape the specimen. A detector composed of a scintillator, a photomultiplier and an output is used to detect emitted electrons, acquire sample information and produce 2-D images. The detection process relies primarily on the raster scanned primary beam. The number of SEs reaching the detector changes

depending on the surface properties and this changes the brightness in the two-dimensional intensity distribution [158].

BSEs can be used to analyze the contrast between areas with different chemical compositions. The BSEs are high energy electrons which are elastically scattered and essentially possess the same energy as the incident primary electrons. The depth from which the BSEs escape depends on both the beam energy and the sample composition. The probability of backscattering increases with the atomic number Z of the sample material, which can be shown as $0.05 \times Z^{0.5}$. This feature can be used for generating compositional images in which the higher Z phases appear brighter compared with the lower Z phases. However, this is not a strong function of Z, so the elemental identification is not optimal [158].

The inelastic interaction of the primary electron beam with the sample also emits inner electrons from the sample. This creates a vacant space in the inner shell and the atom relaxes by a transition in which an outer shell electron fills the inners shell by releasing energy in the form of photons (characteristic X-rays) or electrons (Auger electrons) [158]. These emitted X-rays and Auger electrons are characteristic of the particular atom undergoing emission and so are a possible source for an unambiguous identification of chemical compositions.

Since each atom in the periodic table has a unique set of electron orbitals, the density of a particular type of atom can be identified by measuring the density of x-rays of the corresponding energy. Then the concentration of each element in the sample can be determined. Usually, SEM systems are equipped with an EDX (Energy-dispersive X-ray spectroscopy) detector unit which is used for atom identification. EDX samples the entire depth of interaction, typically about 1 μm. Auger electron spectroscopy (AES) is a common analytical technique to study sample surface, since the escape depth of Auger electrons is only about 1 nm. Under such circumstances, sputtering etching cycles can be coupled with AES to obtain a precise chemical composition depth profile. Also, the Auger yield becomes smaller than X-ray yield for heavier elements, which means it will be more difficult to measure Auger signal for atoms with large Z. However, AES is sensitive to lighter elements and can be used to identify elements as light as lithium (Z = 3) [159].

### 3.1.3 Thin Film Thickness and Roughness

Thin film thickness can be easily measured by a surface profilometer which is equipped with a sensitive stylus placed in contact with the surface and moves along the sample. The vertical deflection measures the step height of the surface. A sharp step between the film and substrate is required for this technique. Usually the profilometer measurements are accurate from >100 nm range, while SEM cross-section images are useful for measuring films thinner than 100 nm [159].

Other than this mechanical thickness measurement technique, there are two major optical techniques for thin film thickness measurement, interferometry and ellipsometry. Both of them use impinging light on the film surface and measure a reflection. Interferometry relies on the interference of two or more beams of light from air/film interface and film/substrate interface. The film thickness is related to the optical path difference. Interferometry is mainly used for measuring transparent films since interference naturally occurs. Ellipsometry is a polarization spectroscopy and measures the changes in the state of polarization of light reflected from film surface [159]. Ellipsometry is able to measure the optical properties of single-layer films and multilayer dielectric film stacks and, in some cases, can monitor films *in situ* during deposition and processing. As a result, ellipsometry is sometimes incorporated into plasma and CVD reactors, or molecular beam epitaxy (MBE) systems.

Atomic force microscope (AFM), the most common of the various scanning probe microscopies (SPM), is commonly utilized to obtain information of film roughness and grain shape. The thin film surface is imaged by a force with a vertical resolution on the order of nanometer. The major advantage of detecting force rather than current is that all kinds of material surfaces including metals, semiconductors, and insulators can be imaged [157]. An AFM typically is composed of a cantilever, a sharp tip, xyz-drive, a detector, controller and plotter. In order to mechanically sense atomic-scale surface topography, the sharp tip should be mounted at the end of a soft cantilever spring, which

has a smaller spring constant than that effectively exists between atoms, so that the applied force isn't large enough to displace surface atoms. In this mechanical raster-scanning system, tip-sample interactions are transduced into the cantilever deflection, which will be converted into an image by a display system. A feedback system is used to monitor and control the cantilever force to diminish the sample surface damage [157].

### 3.1.4 Type of Conductivity and Resistivity

The hot point probe method is a simple technique to determine the conductivity type (n-type or p-type) of semiconductors. Two probes are attached from the sample surface to a current meter, and one probe is maintained at a higher temperature (hot probe) while the other isn't heated (cold probe). The temperature gradient creates a flow of majority carriers between the hot and cold probes. The direction of the current is determined by the polarity of the majority carriers in the sample. In n-type materials electrons are the majority carriers and net flow will generate "positive current" into the hot probe and for p-type material it will be "negative current" [157]. Probe heating is achieved by passing a current through the heating element which is placed near the hot probe. The impurity concentration and charged carriers dynamic parameters can also be calculated [160].

The Hall effect, discovered in 1879 by E. H. Hall [161], has been widely utilized to measure the electronic properties of materials. The Hall effect describes the creation of a transverse voltage that is perpendicular to both the applied magnetic field and the current

along the length of the sample, as shown in Figure 3.4. Lorentz force, the force exerted on a moving electric charge in a magnetic field, is the underlying principle. The well-known “right hand rule” allows us to determine the direction of Lorentz force on a charge carrier based on its direction of motion and the direction of the applied magnetic field.

Hall effect measurements are widely used in many areas of the electronics industry, including basic materials research, device development, and device manufacturing. To be more specific, it can be used to determine quite a few material parameters, such as Hall mobility, carrier concentration, Hall coefficient ($R_H$), resistivity, and most importantly, Hall voltage ($V_H$). With the assistance of some other instruments, I-V characterization curves can be created with a similar test setup [162].

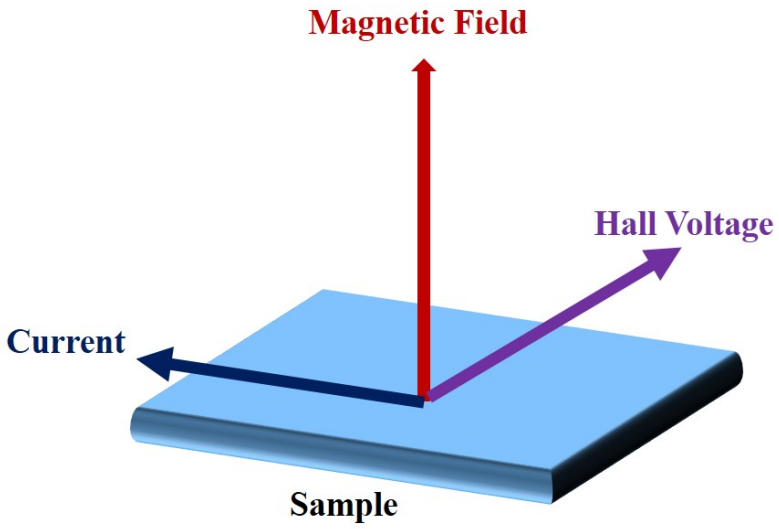


**Figure 3.4 Illustration of Hall effect.**

Specifically, Hall effect measurements attracted industrial researchers' attention because of its convenience and effectiveness for bulk silicon material characterization. Since silicon bulk material properties are well-understood, Hall effect measurements have been utilized for modern semiconductor material development, especially for thin films. For example, the detailed study of thin film carrier concentration and carrier mobility is required for better photovoltaic performance.

Resistivity is another critical parameter of the bulk material for semiconductor device fabrication and it's essential in determining the characteristics of the completed devices [163]. A four-point probe method was discussed, which consisted of placing four probes that make contact along a line on the surface of the material. A current is passed through the outer pair of probes and the resultant voltage is measured across the inner pair, as shown in Figure 3.5.

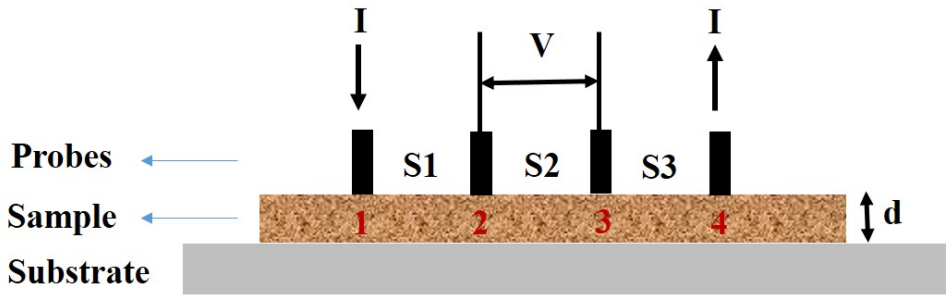


**Figure 3.5 Schematic diagram of four-point probe setup.**

The resistivity is calculated using Ohm's law with a correction factor which takes into account the geometry of the arrangement [163]. The floating potential $V_f$ of a distance r from an electrode carrying a current $I$ in a material of resistivity ρ is given by

$$V_f = \frac{\rho I}{2\pi r} \tag{3.2}$$

In the diagram shown in Figure 3.5, there are two current carrying electrodes, numbered 1 and 4 and they carry current of the same magnitude but in opposite directions. As a result, the floating potential $V_f$, at any point in the semiconductor is the difference between the potential induced by 1 and 4 electrodes. Thus:

$$V_f = \frac{\rho I}{2\pi}\left(\frac{1}{r_1} - \frac{1}{r_4}\right) \tag{3.3}$$

Where $r_1$ and $r_4$ are the distances from probe 1 and 4.

The floating potentials at probe 2 $V_{f2}$ and at probe 3 $V_{f3}$ can be calculated from (3.3) by substituting the proper distances as follows:

$$V_{f2} = \frac{\rho I}{2\pi}\left(\frac{1}{S_1} - \frac{1}{S_2+S_3}\right) \tag{3.4}$$

$$V_{f3} = \frac{\rho I}{2\pi}\left(\frac{1}{S_1+S_2} - \frac{1}{S_3}\right) \tag{3.5}$$

The potential difference V between probe 2 and 3 is then

$$V = V_{f2} - V_{f3} = \frac{\rho I}{2\pi}\left(\frac{1}{S_1} + \frac{1}{S_3} - \frac{1}{S_1+S_2} - \frac{1}{S_2+S_3}\right) \quad (3.6)$$

Usually the probe spacing is equal, that is S1 = S2 = S3 = S ~1 mm (much smaller than the sample thickness d), then the resistivity ρ can be simplifies to

$$\rho = \frac{V}{I} 2\pi S \quad (3.7)$$

When the probe spacing S is much larger than the sample thickness d, the resistivity ρ is given by:

$$\rho = \frac{V}{I}\frac{\pi d}{\ln 2} = 4.53 d \frac{V}{I} \quad (3.8)$$

In the case of thin films the second condition is always used because the film thickness is very small compared with the probe spacing [163]. Three different values of current were applied and the corresponding voltages were taken. The data is fitted using a straight line function and a value for $V/I$ calculated and applied to the above Eqn. (3.8) to calculate the resistivity.

### 3.1.5 Optical Properties

In this work, CZTS optical properties dependent on the bandgap of the material are studied by transmission/absorption measurement. The reflectance (R) and transmittance (T) of the sample were measured and the absorption (A) can be calculated using the following equation.

$$R + T + A = 1 \tag{3.9}$$

where absorption $A = \alpha d$, $\alpha$ is the absorption coefficient and d is the sample thickness. The absorption coefficient $\alpha$ can be calculated using the following equation [164]:

$$\alpha = -\frac{1}{d}\ln\left(\frac{T}{(1-R)^2}\right) \tag{3.10}$$

The derived value of $\alpha$ was used to calculate the band gap of the material described later in this session. For measuring CZTS thin films, the scanning wavelength was from UV to NIR range (350 nm to 1100 nm) by utilizing two different diffraction gratings.

If $I_0$ is the intensity of the incident light and I is the intensity of the light after passing through the sample, then from the Beer-Lambert-law, we have:

$$I = I_0 \exp(-\alpha d) \tag{3.11}$$

This refers to the band-band absorption in which an electron is excited from the valance band to the conduction band of a semiconductor.

Conventionally for inorganic semiconductors, electrons can be excited from the valence band to the conduction band by absorption of incident radiant energy only if this energy is equal to or larger than $E_g$. Thus, absorption edge of light occurs when a quantum of energy ($h\gamma$) equals $E_g$;

$$E_g = h\gamma_g = \frac{hc}{\lambda_g} = \frac{1240}{\lambda_g}\ eV \tag{3.12}$$

Where $\gamma_g$ and $\lambda_g$ are the frequency and wavelength at absorption edge, respectively.

Taking logarithms on both sides of Eqn. (3.11),

$$\alpha = \frac{1}{d}\ln\left(\frac{I_0}{I}\right) \tag{3.13}$$

$$A = \ln\left(\frac{I_0}{I}\right) \tag{3.14}$$

A simple analysis of the absorption process yields a fundamental form for absorption coefficient [164]:

$$\alpha \propto \left(h\gamma - E_g\right)^{1/2} \tag{3.15}$$

$$\alpha \propto \left(h\gamma - E_g\right)^{3/2} \tag{3.16}$$

Eqn. (3.15) and (3.16) are for direct and indirect band gap material, respectively. Here $E_g$ is the energy band gap of the material. Thus a plot of $(\alpha h\gamma)^2$ verses $h\gamma$ gives the direct band gap energy.

## 3.2 CZTS Thin Film Solar Cell Measurement Techniques

### 3.2.1 I-V Measurement

Typically a solar cell I-V measurement system is composed of a source meter, a solar simulator equipped with an AM 1.5 global filter, a feedback/stabilizer, and a microcontroller regulated unit to maintain a constant power output irrespective of the lamp aging or filament erosion. The output light from the solar simulator was focused on the sample, which was placed on a specially designed spring-loaded probe station. The measurement parameters were controlled and I-V data was collected by computer. Current-voltage data, called an I-V curve, can be plotted as shown in Figure 3.6. The curve can be used to extract some important device parameters.

The short circuit current ($J_{sc}$) can be obtained at zero voltage, while the value of the voltage at zero current is called the open circuit voltage ($V_{oc}$) of the solar cell. These are the maximum voltage and current that the cell can output. The power output of the solar cell is zero at these two points. If the power versus the voltage is plotted, this curve has a maximum power point, which is used to calculate the power conversion efficiency.

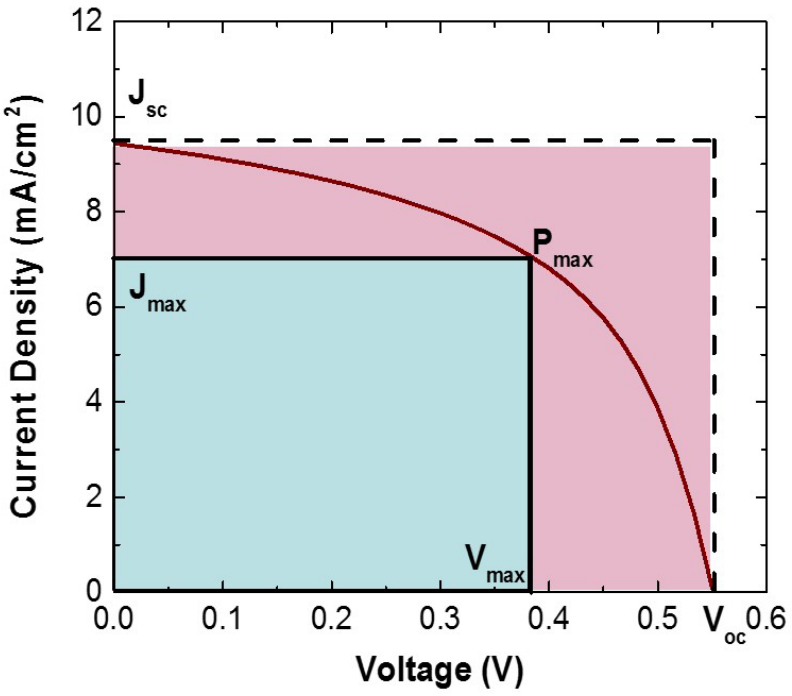


**Figure 3.6 Typical I-V curve of a solar cell.**

The I-V curve can also be used to extract another important parameter, the fill factor (FF). This gives information about the form of the IV curve. It is the ratio of the maximum output power (shown as blue area) and the maximum power that the cell could theoretically give (shown as pink area). The latter is the product of $J_{sc}$ and $V_{oc}$. The FF should be as high as possible, and it shows some internal resistance values in the cell that can be subject to optimization.

Solar cells can be modeled mathematically by an idealized equivalent circuit [4], where the photo-generation at the junction can be represented by a constant current source. Typically one also includes a series resistance ($R_S$) and a shunt resistance ($R_{SH}$). The

latter represents leakage and/or recombination associated with the junction. The value of $R_S$ depends on a number of factors such as the sheet resistance and geometry of the electrodes, the contact resistance, and the resistance of the quasi-neutral region. Generally, $R_S$ and $R_{SH}$ determine the shape of the I-V curve and so the value of the fill factor. This directly affects the solar cell conversion efficiency. The $R_S$ and $R_{SH}$ values can be calculated based on the slope of the I-V curve at the $V_{oc}$ and $J_{sc}$, respectively.

### 3.2.2 C-V Measurement

C-V measurement is one of the most widely-used electrical measurement techniques for evaluating semiconductor device characteristics. The advantages of C-V measurement are: (i) this technique is non-destructive; (ii) various important parameters can be measured, such as the carrier concentration [165], interfacial defect level [166], bulk or surface states, and heterojunction properties [167]; (iii) the method can be used on fabricated devices and is adaptable for automation [168].

The Schottky diode or the p-n junction is simply described as a small-signal equivalent circuit model which is composed of a capacitor parallel with a resistor. Except at strong forward bias, the capacitor represents the space-charge capacitance, while the resistor shows the residual conductance of the diode [167]. A constant ac voltage is applied to the diode and the capacitance is calculated from the imaginary part of the resulting admittance, while the real part leads to conductance. Often a dc voltage is swept and the

dependence of the capacitance on dc voltage is used to measure a carrier profile versus depth as discussed below. To obtain a more accurate depth profile in the presence of traps, dc voltages are successively superimposed. This is called drive level capacitance profiling (DLCP) [169].

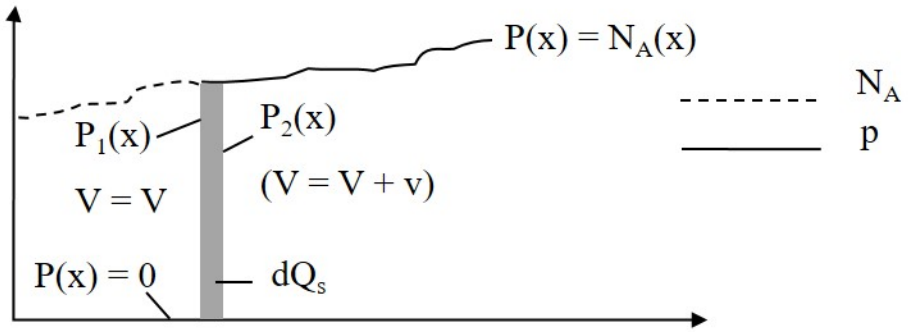


**Figure 3.7 Doping density profile in the depletion approximation.**

In this work, C-V measurement was conducted mainly to estimate the CZTS doping density and CZTS/CdS interfacial properties using an impedance analyzer. The doping density and majority density profiles in the depletion approximation is shown in Figure 3.7. From the fundamental definition of capacitance, we have

$$\mathrm{C} = -\frac{dQ_s}{dV} \tag{3.17}$$

Where $$dQ_s = -qAN_A(w)dw \tag{3.18}$$

Then we have $$\mathrm{C} = -\frac{dQ_s}{dV} = \frac{qAN_A(w)dw}{dV} \tag{3.19}$$

If we assume depletion region as a dielectric material with a dielectric constant $\varepsilon_s = K_s\varepsilon_0$, then we have

$$C = \frac{K_s\varepsilon_0 A}{w} \tag{3.20}$$

Then the doping density can be calculated as a function of C-V data,

$$N_A(w) = \frac{2}{qK_s\varepsilon_0 A^2\left(d\left(\frac{1}{C^2}\right)/dV\right)} \tag{3.21}$$

DLCP measurements are usually performed and supplemented with C-V data. Especially, when it is important to characterize the CZTS thin film bulk doping density and interface response with post deposition RTA conditions, DLCP measurement becomes very critical.

DLCP measurements are usually taken with DC bias values ranging from -0.2 to +0.5 volts, with the drive-level amplitude varying between 0.06 and 0.12V, at a frequency of 200 kHz. Samples were mounted in a dark cryostat with liquid nitrogen cooling. The drive-level density $N_{DL}$ of CZTS thin film at various depth can be calculated from the DLCP results. It is reported [169] that, due to the high n-type doping concentration in the CdS window layer, the depletion region is almost entirely in the CZTS, and thus the $N_{DL}$ values determined by DLCP are representative of the CZTS. These quantities are not sensitive to interface states. Thus, DLCP measurement will provide a more precise description of CZTS bulk carrier concentration.

### 3.2.3 EQE Measurement

Two types of quantum efficiency (QE) of a solar cell are often studied. The external quantum efficiency (EQE) stands for the ratio of the number of carriers collected by the solar cell to the number of photons of a given energy (wavelength) incident on the solar cell. The internal quantum efficiency (IQE) represents the ratio of the number of carriers collected to the number of photons of a given energy (wavelength) absorbed by the solar cell. The EQE of a solar cell includes the effect of optical losses such as transmission and reflection and is of more interest to most researchers.

If all photons of a certain wavelength are absorbed and the resulting minority carriers are collected, then the quantum efficiency at that particular wavelength is unity. The quantum efficiency for photons with energy below the band gap is zero. A typical quantum efficiency curve for a solar cell is shown below.

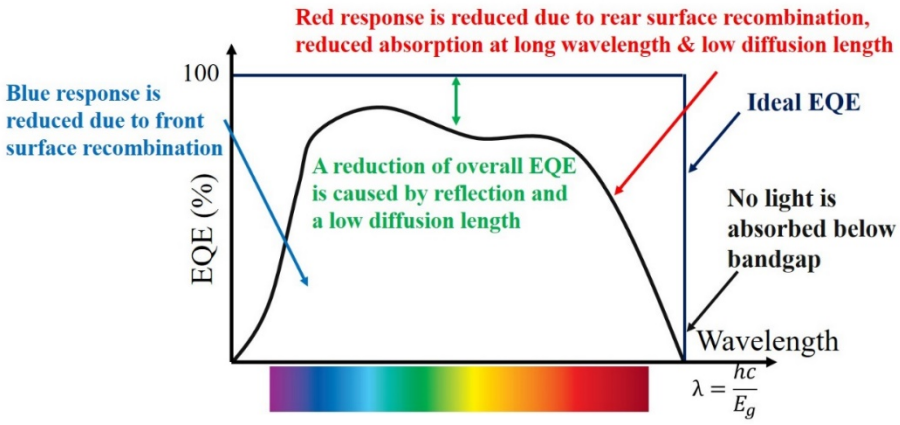


**Figure 3.8 The EQE spectrum of a solar cell under illumination [13].**

EQE measurements were conducted to assess the factors that limit the CZTS solar cell performance and further improve the material design and device efficiency. EQE measurements are preferably carried out by measuring the effect of a small amount of monochromatic light under short-current conditions [170].

# Chapter 4

# 4 Synthesis and characterizations of $Cu_2ZnSnS_4$ (CZTS) Thin Films

## 4.1 Synthesis of $Cu_2ZnSnS_4$ (CZTS) Thin Films

Polycrystalline $Cu_2ZnSnS_4$ (CZTS) were made on Mo-coated soda-lime glass (SLG) by sulfurization of thermally-evaporated metal precursor layers (copper, zinc, and tin) under vacuum. The thicknesses of metal layers in precursor stack were adjusted to tune the film composition. Substrate material choice, sulfurization conditions, and back contact metal's influence on CZTS growth was studied. Metal stacking order (from bottom to top) of the precursors was also investigated.

### 4.1.1 Thermal Evaporation of Cu-Zn-Sn Precursor

Successive ultrasonic cleaning in a soap solution, deionized water, isopropanol, and acetone was used to clean SLG substrates and then the substrates were dried with nitrogen and baked at 120 $^oC$ for 5 minutes. The deposition of a Molybdenum (Mo) back contact layer was conducted by a two-step dc magnetron sputtering method which was developed to get good adhesion and a low sheet resistance [128, 171]. Then, the metallic precursor deposition was performed by sequential thermal evaporation under vacuum (below $2\times10^{-6}$ Torr).

The thermal evaporator was used to sequentially deposit precursor metals onto the substrates. Under vacuum, current is passed through a filament boat, which heats the metal contained in the boat. When the desired evaporation current is reached, the molten metal evaporates. Some of the vapor deposits onto the substrate. The deposition rate of each layer was kept at about 0.1 nm/sec by controlling the current passing through the filament boat. *In situ* thickness monitoring was performed with a quartz crystal rate monitor.

### 4.1.2 Sealing of Quartz Ampoule

Sulfurization of metal precursors was conducted in a sealed space under vacuum. Quartz is one of the most popular materials for a fusing ampoule. Clear fused quartz tubes ordered from AdValue Technology with 12.7 mm outer diameter, 10.5 mm inner diameter and 1.1 mm wall thickness are used. The quartz tubes were sealed at one end initially and were cleaned using a soap solution, deionized water, isopropanol, and acetone, successively. Then they were allowed to dry naturally overnight.

Sealing of the ampoule was initially done in the glass shop in department of Chemistry. The quartz ampoule with a piece of Cu-Zn-Sn precursor and a small amount of sulfur powder inside was pumped down overnight in a research lab in the Material Science department, and then sealed by a tri-clamp and brought to glass shop for fusing.

However, there is a concern that tri-clamp is not a perfect seal and there might be leakage to the ampoule which will introduce oxygen and moisture to the reaction environment.

In order to improve the ampoule vacuum, an oxygen/propylene gas torch sealing system was built in our lab with Dr. Sreejith Karthikeyan's help. This system allows one to reliably seal the ampoule while pumping it down. The sealing system is composed of a vacuum system comprising a Navco rotary oil vacuum pump and a Leybold turbopump, oxygen and propylene gas cylinders, and a cutting torch (Smith Equipment). One open end was used for connecting the tube in to the vacuum system while the precursor and sulfur powder would stay at the other end of the tube which was completely sealed initially.

Prior to sample loading, the tube was exposed to an oxygen-propylene cutting torch flame during pump down, which was applied from one end to the other end which was connected to the vacuum system three to four times to remove the remaining moisture from inside the tube. The open end of the tube was used to then load the precursor film stack and the sulfur powder and to connect the tube to the pumping system. The tube was then pumped down to $2\times10^{-6}$ Torr or below, as shown in Figure 4.1.

**Figure 4.1 The image of the sealing system.**

Again a gentle flame was moved briefly from sample end of the tube to other in order to remove remaining moisture. Applying a gentle flame can remove remaining moisture but care was needed to avoid an exothermic reaction of the elements or the sublimation of sulfur. Then the hot oxygen/propylene flame was carefully introduced about 10 cm away from the precursor and sulfur powder. Extreme care was taken at this point because the tube was under vacuum and there was a possibility that the softened quartz could be sucked inside and that could lead to breakage of the tube. Upper and lower sides of the tube were heated to become softened and then the tube was rotated slowly. This allowed the softened areas to touch each other and remain in contact till both sides were fused completely. After sealing the ampoule was removed and stored for use.

### 4.1.3 Sulfurization of Metal Stack Precursors

When we were ready to carry out the sulfurization, the sealed ampoule was placed in a ceramic holder and then inserted in a tube furnace, heated to a certain temperature and cooled to room temperature naturally to form CZTS thin films. The half of the ampoule containing the sample was inside of the ceramic holder, while the other half was hanging in space. This configuration creates a temperature gradient when cooling down and helps excess sulfur condense at the end of the ampoule opposite the sample. Sulfurization parameters were programmable for this tube furnace, such as ramping rate for heating and cooling, temperature set point, hold time, etc. It's not necessary to flow any inert gas during sulfurization because the ampoule was sealed and formed an isolated reaction environment itself.

## 4.2 Substrate Influence on CZTS Properties

The most widely used substrate for CZTS thin film solar cells is Mo-coated SLG which is a carryover from CIGS solar cells, where, as discussed in a previous chapter, it has been shown that sodium (Na) diffusion from the SLG to CIGS drastically increases the power conversion efficiencies [110, 111, 139, 140]. A few studies on Na diffusion have shown an enhancement of CZTS grain growth [142-144, 172]. It has been proved that alkali element potassium (K) is also beneficial to grow CZTS thin film with larger grains [109]. However there is no widely accepted theoretical explanation on this phenomenon. Based

on previous study on Na diffusion and its influence on CZTS grain growth, SLG has become the first choice of substrate for CZTS synthesis. In this chapter, CZTS thin films were synthesized on SLG and the mechanism of CZTS grain growth was investigated. However, SLG has several drawbacks. SLG has a glass transition temperature ($T_g$) of about 575 $^oC$ limiting the sulfurization temperature since softening of the SLG might introduce film stress to CZTS which will be detrimental to thin film solar cells. What's more, SLG is a brittle material that can be easily broken, making SLG substrates unattractive for commercial CZTS solar cells and modules. As a result, it is worthwhile to investigate other alternate substrate materials and their influence on CZTS microstructures and phase composition.

This part presents the thin film morphology and structural property data obtained from CZTS thin films deposited on various substrates while keeping other parameters the same. CZTS thin films were synthesized by sulfurization of thermal evaporated Cu, Zn, Sn metal stack precursors on three different substrates including SLG, fused silica, and sapphire ($Al_2O_3$). Fused silica is amorphous (non-crystalline) silica without other added impurities. Crystalline sapphire ($Al_2O_3$) glass is highly transparent and significantly stronger than any other optical materials or glasses [173]. Compared to those two pure materials, a large amount of impurities can be found in SLG, which is made by melting various materials, such as sodium carbonate (soda), lime (calcium-containing material ),

dolomite ( $CaMg(CO_3)_2$), silicon dioxide (silica), aluminium oxide (alumina), and small quantities of sodium sulfate and sodium chloride [174].

**Table 4.1 Properties of three different substrates for CZTS synthesis.**

| Substrate | Thermal Expansion coefficient (/$^oC$) | Softening Point ($^oC$) | Added Impurities (mole %) |
|---|---|---|---|
| Fused silica | $5.5\times10^{-7}$ | 1683 | None |
| Sapphire ($Al_2O_3$) | $7.5\times10^{-6}$ | | None |
| SLG | $8.6\times10^{-6}$ | 575 | $Na_2O$ (13%), CaO (9%), etc |

Metal precursors with stacking order Sn/Zn/Cu (from bottom to top) were deposited on three different substrates (fused silica, sapphire, and SLG) using thermal evaporator under exactly the same conditions. Total thickness of precursors was about 58 nm. After sulfurization at 450 $^oC$ and 500 $^oC$ for 8 hours, thin films obtained were characterized using XRD, SEM and EDS.

X-ray diffraction results collected from samples deposited on three substrates showed all of the XRD peaks aligned to kesterite CZTS, as shown in Figure 4.2. However, the CZTS main peaks (112) at 28.44 $^o$ and (204) at 47.33 $^o$ can also be assigned to ZnS or $Cu_2SnS_3$ so secondary phases couldn't be ruled out in this case. The CZTS (101) peak at 18.24 $^o$ was only observed in thin film grown on SLG, which means SLG enhances CZTS grain

growth. The mean size of CZTS crystallites can be derived from XRD results by Scherrer Formula

$$\tau = \frac{K\lambda}{\beta \cos\theta} \tag{4.1}$$

where $\tau$ is the mean size of the crystallites, which may be smaller or equal to the grain size; K is a dimensionless shape factor, with a value close to unity; $\lambda$ is the X-ray wavelength; $\beta$ is the line broadening at half the maximum intensity (FWHM), after subtracting the instrumental line broadening, in radians; $\theta$ is the Bragg angle.

Usually, the Scherrer formula is limited to nano-scale particles [175], and it's not applicable to grains larger than about 0.1 to 0.2 μm, which precludes those observed in most CZTS microstructures. However, sample grain size can be roughly estimated because the relatively small grains observed in SEM images (Fig. 4.3). As shown in Figure 4.2, smaller FWHM was observed for XRD peaks collected from thin film deposited on SLG substrate, which indicated larger grains. It is quite critical that the Scherrer equation provides an effective estimation on the particle size, since a variety of factors can play a role in the width of a diffraction peak besides instrumental effects and crystallite size. Among those factors, the most important are usually inhomogeneous strain and crystal lattice imperfections [175], such as dislocations, stacking faults, twinning, micro-stresses, grain boundaries, sub-boundaries, coherency strain, chemical heterogeneities, etc.

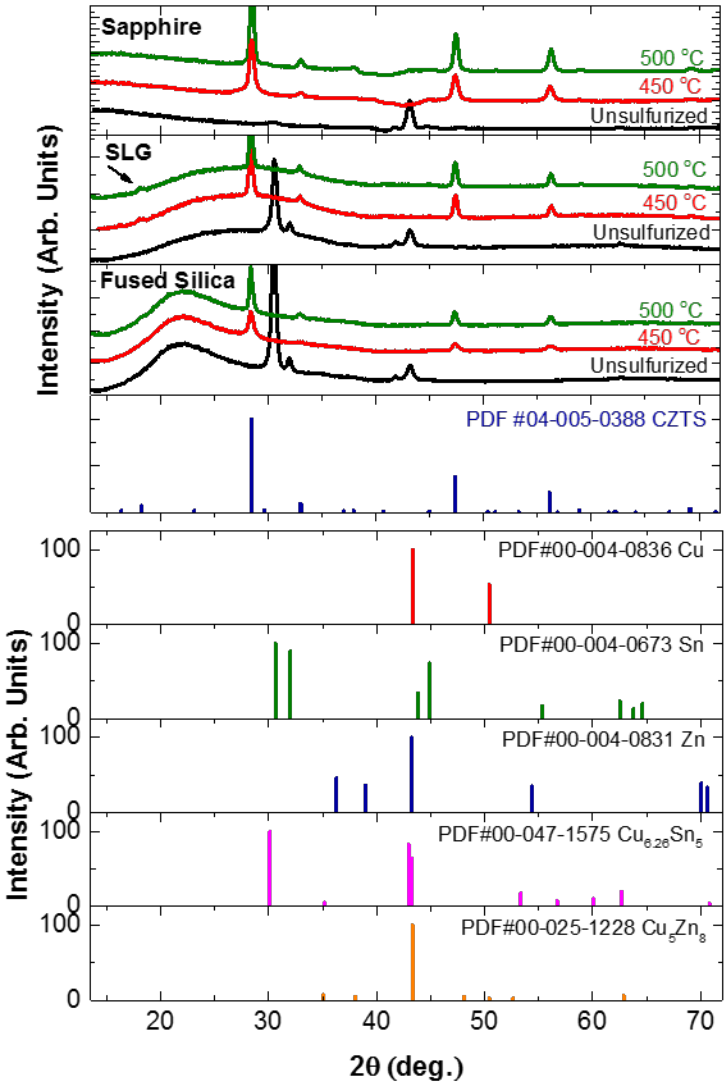


**Figure 4.2 X-ray diffraction results of CZTS deposited on different substrates.**

As shown in Figure 4.3, tiny rod-like and flake-like grains were found in thin films deposited on sapphire and fused silica, while sample grown on SLG showed rounded equiaxed grains. The latter is probably due to bulk diffusion during grain growth.

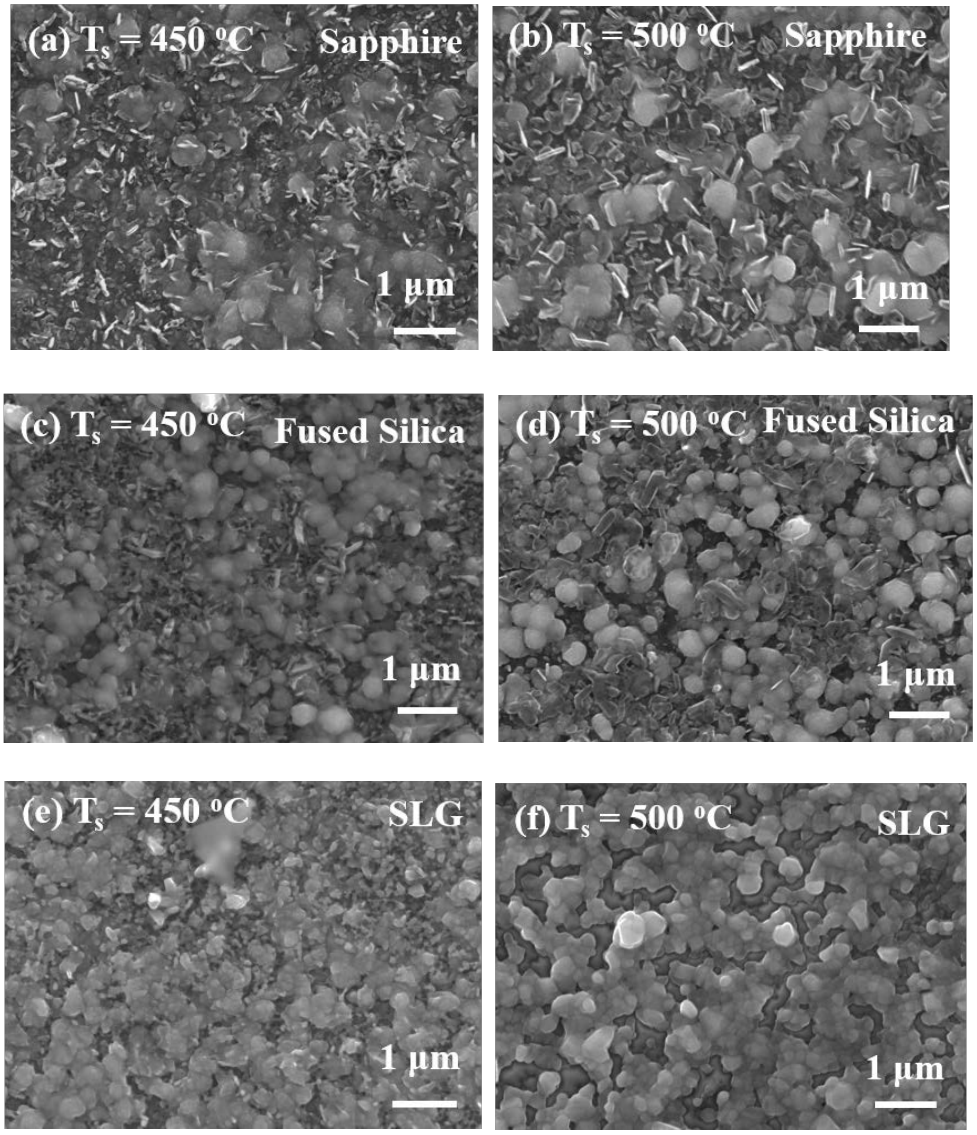


**Figure 4.3 SEM images of CZTS deposited on different substrates.**

When looking at the SEM images closely, a large area of voids were observed in thin film deposited on SLG, while sapphire and fused silica produced void-free thin films. Voids appear when grain size exceeds thin film thickness and it proves thoroughly CZTS grain growth happened when SLG was used as substrate, which is consistent with XRD

results. It is clearly proven that some impurities in SLG are beneficial to CZTS grain growth. Na has been reported to be the critical acting element in SLG [109]. The chemical compositions of the as-deposited metal precursors and sulfurized samples were measured using EDS. All three precursors on sapphire, SLG, and fused silica showed composition Cu/(Zn + Sn) = 1, Zn/Sn = 1 initially. However, the sulfurized film on SLG was closer to stoichiometric CZTS. The loss of Sn and to a lesser extend Cu in the sapphire and fused silica samples suggests that some volatile compounds are formed and evaporate from the surface of the CZTS. In general, SLG is the most stable substrate.

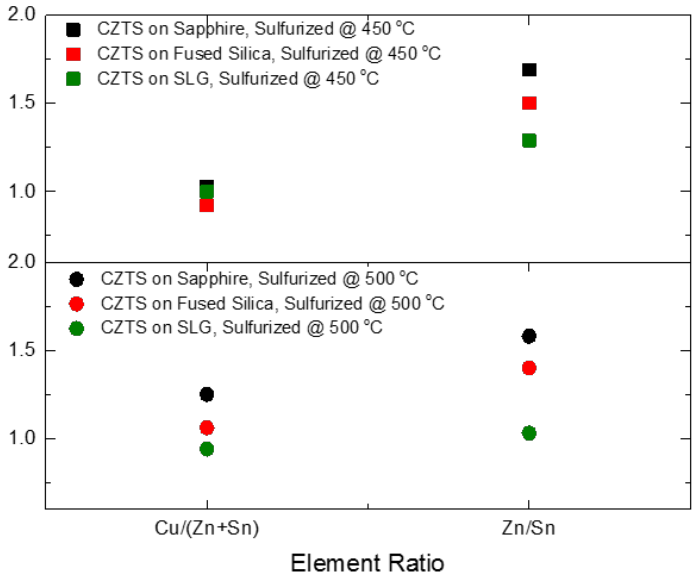


**Figure 4.4 Chemical composition of CZTS deposited on different substrates.**

## 4.3 The Influence of Sulfurization Condition on CZTS Properties

Sulfurization conditions including the sulfurization temperature and time have been studied as well as their influence on CZTS thin film properties. X-ray diffraction and Raman scattering results of samples on SLG (Sn/Zn/Cu) sulfurized at 500ºC, 550ºC and 600ºC for 8 hours have shown that the sulfurization temperature affects the CZTS structure and film morphology. As shown in Figure 4.5, all of the X-ray diffraction peaks are aligned to kesterite CZTS, and stronger XRD peaks were observed at higher sulfurization temperature, indicating a higher degree of crystallinity.

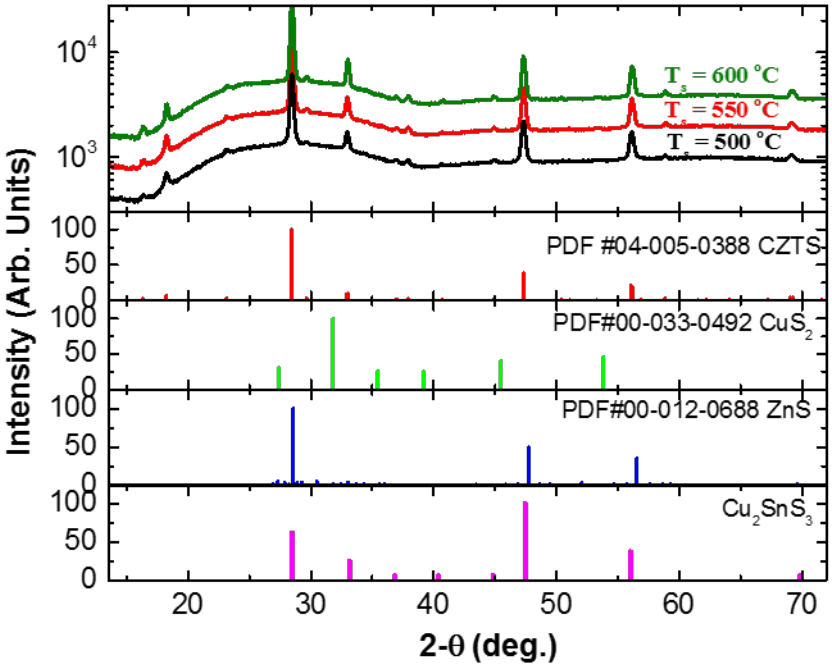


**Figure 4.5 X-ray diffraction results of CZTS sulfurized at 500 ºC, 550 ºC, and 600 ºC.**

Raman scattering results shown in Figure 4.6 indicates that the strongest Raman CZTS peak both increases in intensity and shifts from a lower position to 337 $cm^{-1}$ with increasing sulfurization temperature. Meanwhile, the Raman peaks at 285 $cm^{-1}$ and 370 $cm^{-1}$ were prominent only for the 600 $^{o}$C sulfurized sample. This suggests that increasing phase-pure kesterite films were made at higher annealing temperature, and that the degree of crystallinity increased with sulfurization temperature.

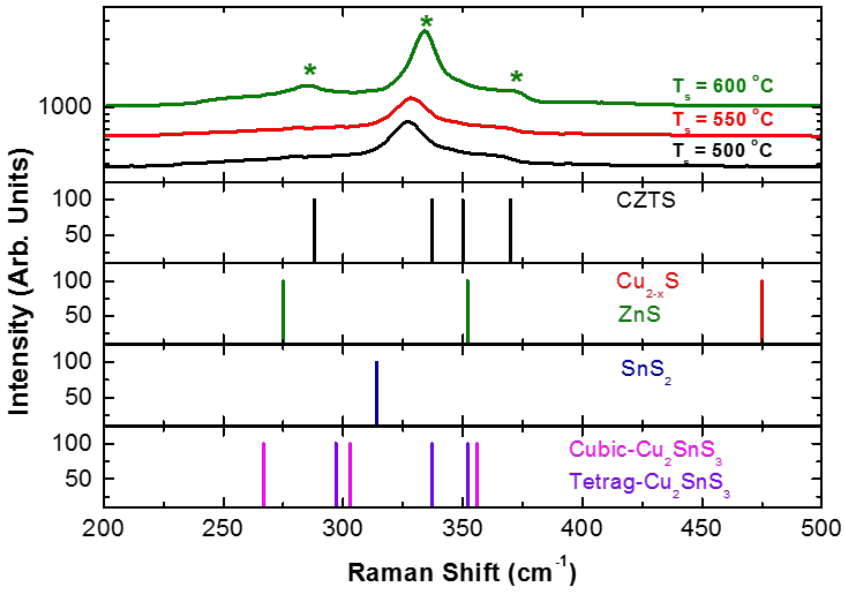


**Figure 4.6 Raman scattering results of CZTS sulfurized at 500 $^{o}$C, 550 $^{o}$C, and 600 $^{o}$C.**

As shown in the SEM images in Figure 4.7, larger CZTS grains, about one micron wide, were formed at higher sulfurization temperature (600 $^{o}$C). Others have seen similar results with intensive grain growth typically between 500 and 600$^{o}$C [92, 94, 176, 177].

As a result, the sulfurization temperature was fixed at 600$^{o}$C and other parameters were varied to optimize the growth conditions.

It is obvious that CZTS thin films sulfurized at 600 $^{o}$C are not void-free (Figure 4.7). This is due to the imbalance between intensive grain growth and the lack of film thickness. The thickness of metal precursor stacks can be adjusted to eliminate this issue and close-packed CZTS thin film with large grains can be obtained, as shown in Figure 4.8.

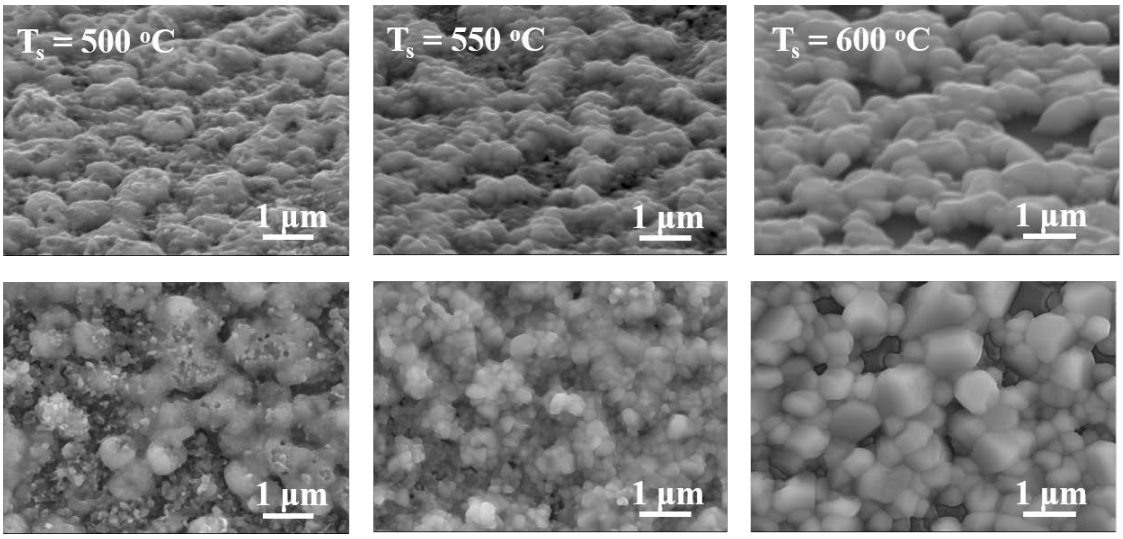


**Figure 4.7 SEM images of CZTS (Tilted view and top view) sulfurized at 500 $^{o}$C, 550 $^{o}$C, and 600 $^{o}$C.**

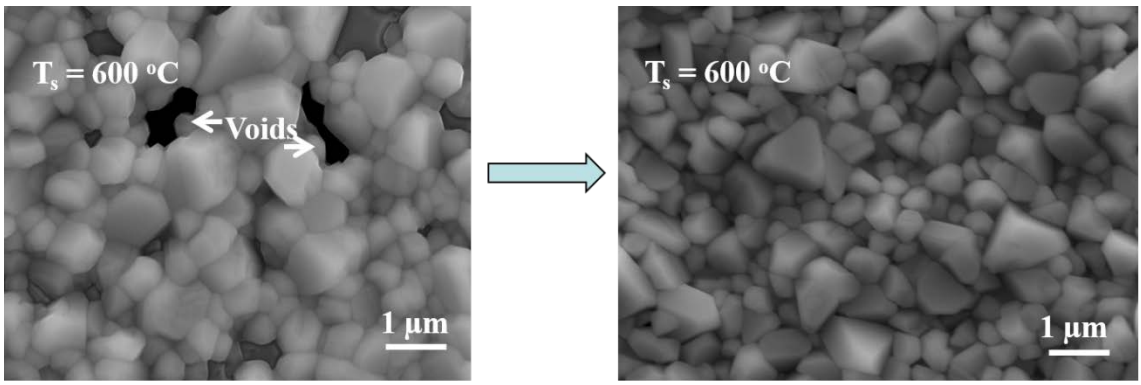


**Figure 4.8 CZTS morphology change with increasing film thickness.**

In order to synthesize functional films for solar cell application, CZTS was also deposited on Mo-coated SLG, where Mo behaves as the back contact layer. However, the addition of the back contact created both morphology and adhesion problems. As is shown in Figure 4.9 (a), there are bumps on the surface of the sample and CZTS thin film peels off from Mo layer. Bad adhesion usually comes from high film stress, part of which is due to thermal expansion coefficient mismatch of two layers, and film surface contamination. The Mo layer (area 4) also cracks during 600 °C sulfurization (Fig. 4.9 (c)) which probably is due to the release of Mo film stress at high sulfurization temperature. It is therefore necessary to study the relationship between Mo film stress and deposition technique and parameters. Two different areas are shown in Fig. 4.9 (b). EDS results show that area 1 is Zn rich while area 2 is closer to stoichiometric CZTS. The sample non-uniformity led to an investigation of the influence of the metal precursor stacking order on CZTS thin film properties, especially morphology.

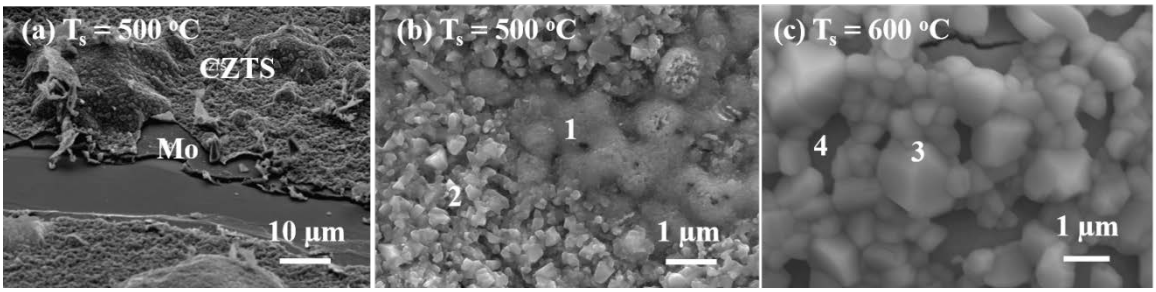


**Figure 4.9 SEM images of CZTS on Mo-coated SLG.**

## 4.4 Precursor Metal Stacking Order Influence on CZTS Properties

Various precursor stacking orders were studied to determine the effect of the film stack on the final film morphology. Three-layer precursor stacks were studied first. Fernandes, P. A. *et al.* suggest that Cu layer should be on the top to reduce the loss of Zn and Sn and achieve a better composition control of CZTS [78]. We found that Zn/Sn/Cu (bottom/middle/top) couldn't produce good CZTS thin film because first layer (Zn) would re-evaporate during second layer Sn deposition. This is due to the higher boiling point (2602 °C) of Sn which requires higher evaporation current to heat the metal source. With the high vapor pressure of Zn, re-evaporation happens and affects the final chemical composition of metal precursor and sulfurized thin film. This made the metal precursor stacking order Cu/Zn/Sn and Sn/Zn/Cu very promising.

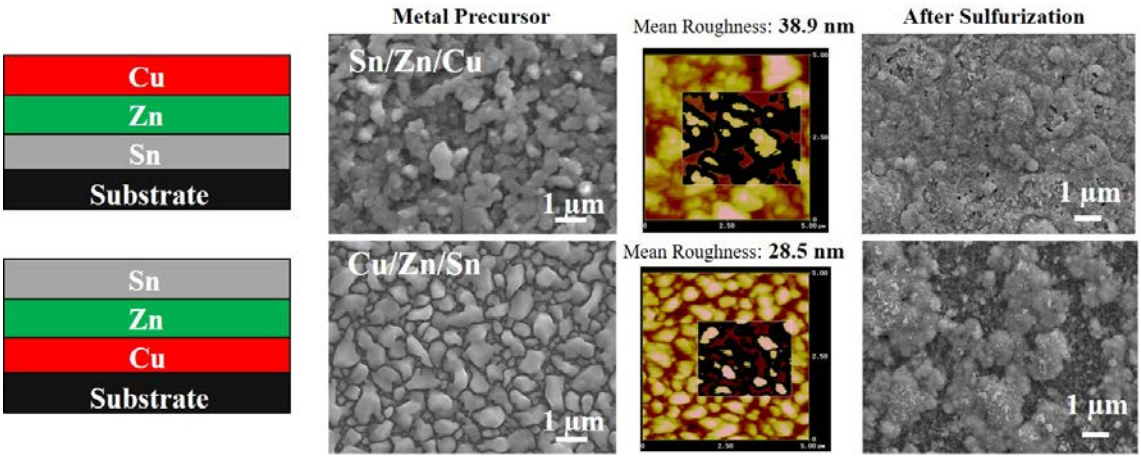


**Figure 4.10 Schematic graphs, SEM, and AFM images of Cu/Zn/Sn and Sn/Zn/Cu metal precursor stacks, and SEM images of sulfurized thin films.**

As shown in Figure 4.10, putting extreme smooth Cu layer at the bottom does help to reduce the total roughness of the precursor, however, Sn layer on the top will increase the film non-uniformity because Sn easily reacts with sulfur, forms sulfides and leaves the film. As a result, I first rigorously tested the stacking order that showed the most promise: Sn/Zn/Cu. The detailed deposition conditions are shown in Table 4.2 below.

**Table 4.2 Summary of deposition conditions.**

| **Precursor metal layers** | **Sulfurization Conditions** | |
|---|---|---|
| (From bottom to top) | Sulfurization Temperature ($^{o}$C) | Sulfurization Time (hrs) |
| Sn: 2185 Å / Zn:1308 Å / Cu: 1901 Å | 600 | 2 |
| Sn: 2185 Å / Zn:1308 Å / Cu: 1901 Å | 600 | 4 |
| Sn: 2185 Å / Zn:1308 Å / Cu: 1901 Å | 600 | 8 |

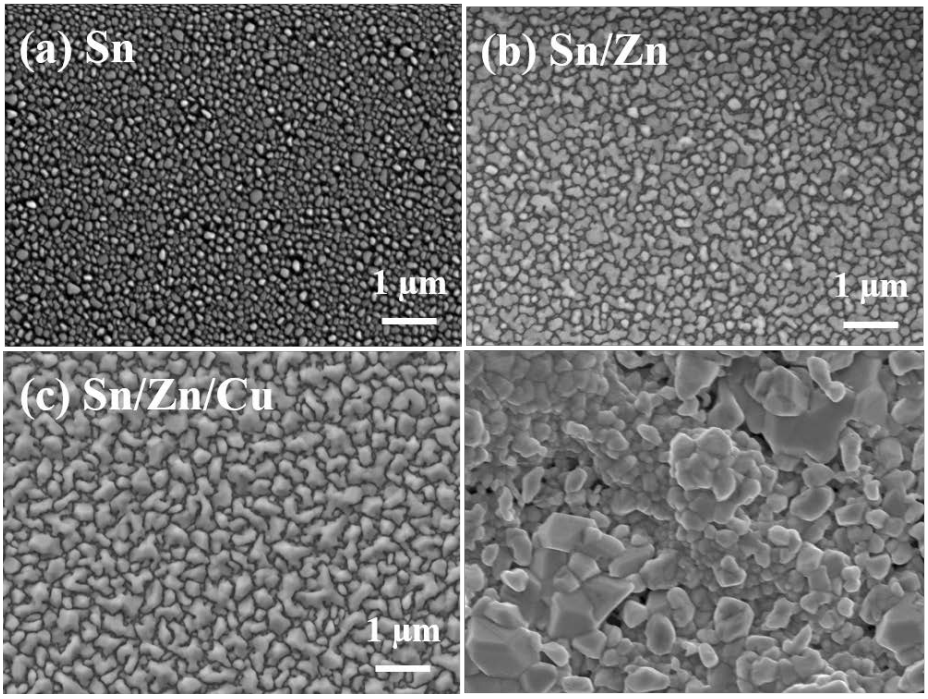


**Figure 4.11 SEM images of (a) first, (b) second and (c) third stacked layers and (d) final CZTS thin film.**

Typical surface morphologies of first, second and third stacked layers of Sn/Zn/Cu precursors are shown in Figure 4.11. From the SEM observations, surface morphologies of each layer of precursors and CZTS thin films are affected by the metal stacking order. Sn doesn't wet glass and it forms large droplets on the substrate which lead to relatively rougher precursor stacks when Sn is deposited as the first layer. Meanwhile, Zn and Sn don't form an alloy. This will slow the metal inter-diffusion process and influences the final thin film properties. Normally, this kind of metal stacks will result in CZTS thin

film with more voids and bigger roughness, as well as poor adhesion between CZTS and the back contact layer, as shown in Figure 4.12.

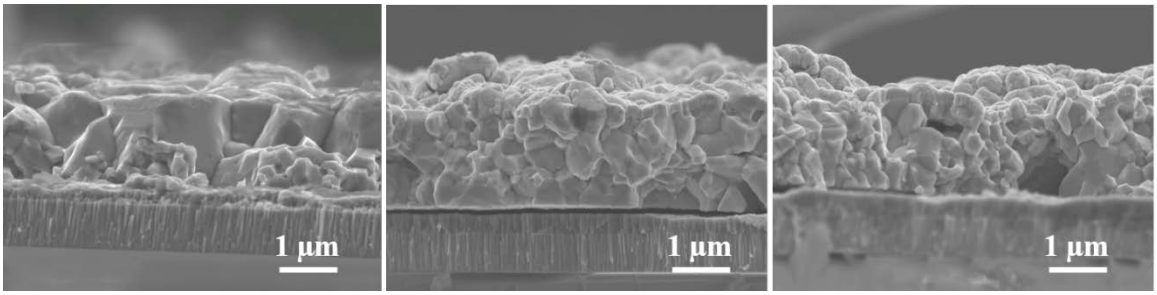


**Figure 4.12 Cross-section SEM images for CZTS deposited on Mo-coated SLG.**

Precursors with optimum three-layer stacking sequence Sn/Zn/Cu on SLG were sulfurized at 600ºC for 2, 4, and 8 hours. X-ray diffraction results collected from these samples have shown that precursor stack affects the phase purity of CZTS films. As is shown in Figure 4.13, films sulfurized from a Sn/Zn/Cu stack directly on SLG show some secondary phases including $Na_2SnS_3$, $Na_4Sn_3S_8$ and SnS. This suggests that sodium diffuses into precursor and forms a sulfide with Sn at the first stage. This might help explain the effect of sodium in CZTS grain growth. These phases disappear after longer sulfurization anneals (Fig. 4.9 (b) Region 1).

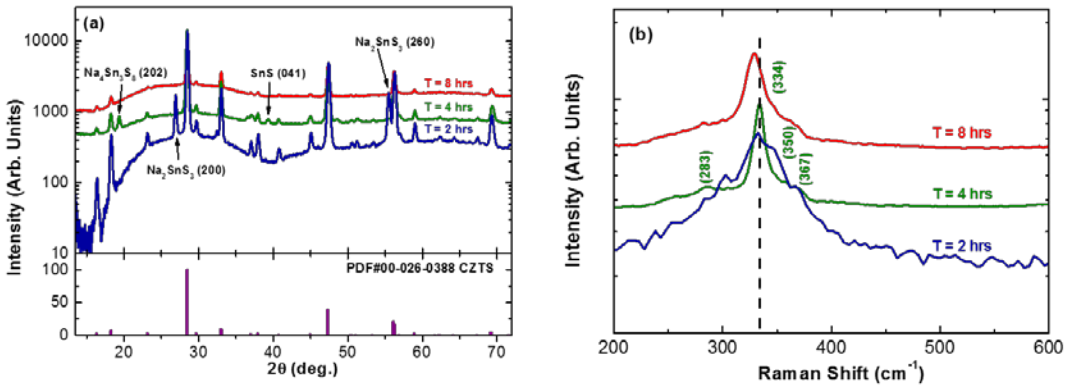


**Figure 4.13 (a) X-ray diffraction results, and (b) Raman scattering results for CZTS thin films sulfurized for 2, 4, and 8 hours.**

Here we propose a CZTS grain growth mechanism (Figure 4.14) which can guide the selection of the metal stacking order to be used to synthesize CZTS thin films with better microstructures. As shown in Figure 4.14 (a), Cu/Zn/Sn metal stack is deposited on Mo-coated SLG. With the increasing sufurization temperature, metal interdiffusion happens and $Cu_{6.26}Sn_5$ and $Cu_5Zn_6$ alloy form first. Sulfur starts to play a role in the process at 300 $^oC$ when multiple types of sulfides such as ZnS, $SnS_2$, $Sn_2S_3$, CuS, $Cu_2SnS_3$ form and the CZTS phase also appears. At higher temperature (500 $^oC$ and above), films are nearly all CZTS with small amount of sulfides, as shown in Figure 4.14 (e).

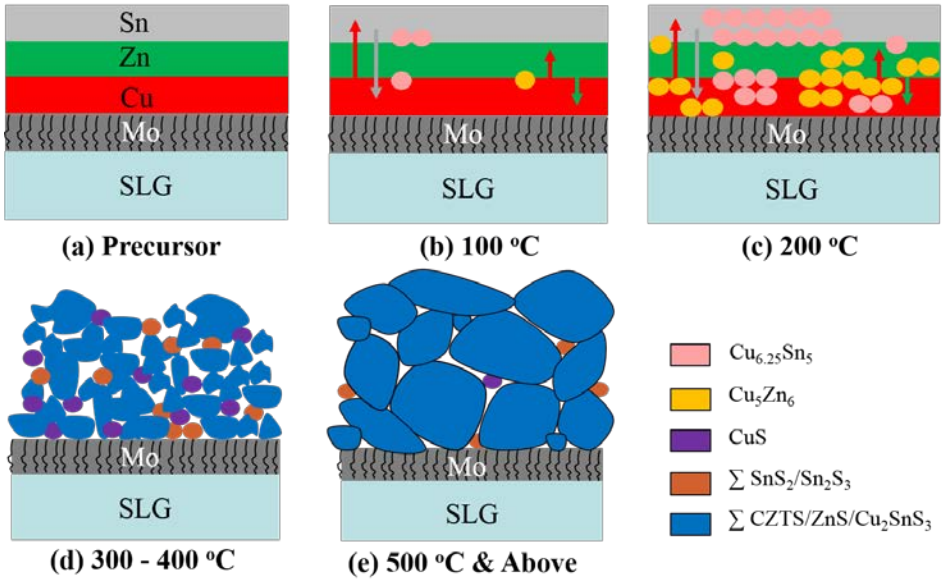


**Figure 4.14 Schematic diagram for CZTS growth mechanism, which was drew based on the CZTS phase evolution theory published by Aydil *et al.* [178].**

While this stack proved the best of the three-layer alternatives, problems remained. Especially common were large, roughly circular Zn-rich regions (Fig. 4.9 (b)). We considered the possibility that droplet formation during the sulfurization process led to the lateral segregation of Zn. The problem is exacerbated in the optimal three-layer stack since zinc and tin form eutectics with melting temperatures as low as 199 °C, as shown in Figure 4.15.

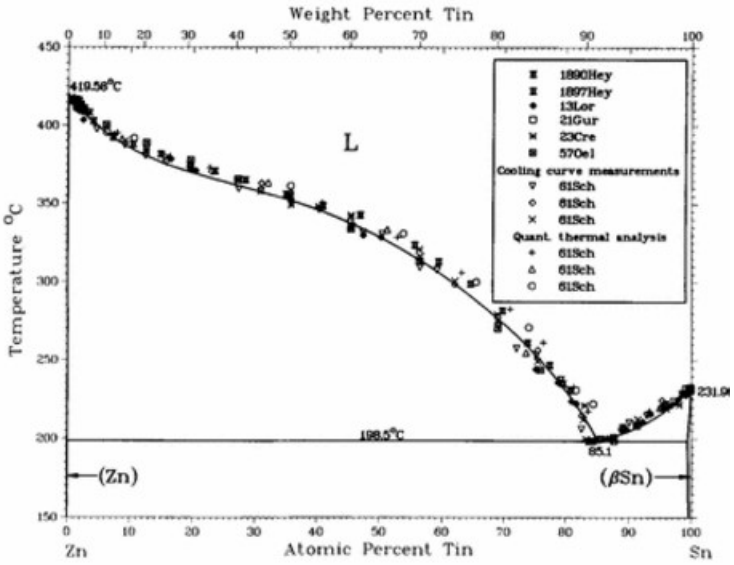


**Figure 4.15 Sn-Zn (Tin-Zinc) system. Source: [179].**

The goal then is to develop a stack or a sulfurization process that avoids this droplet formation. We therefore investigated the metal stack Cu/Sn/Cu/Zn where the embedded Cu layer would impede the formation of Zn/Sn eutectics.

**Table 4.3 Summary of CZTS deposition conditions.**

| **Precursor metal layers** | **Sulfurization Conditions** | |
|---|---|---|
| (From bottom to top) | Sulfurization Temperature (°C) | Sulfurization Time (hrs) |
| Cu: 950 Å / Sn: 2185 Å / Cu: 951 Å / Zn:1308 Å | 600 | 2 |
| Cu: 950 Å / Sn: 2185 Å / Cu: 951 Å / Zn:1308 Å | 600 | 4 |
| Cu: 950 Å / Sn: 2185 Å / Cu: 951 Å / Zn:1308 Å | 600 | 8 |

Precursors with the stacking order Cu/Sn/Cu/Zn produce films with X-ray diffraction peaks that are all indexed to kesterite CZTS, as shown in Figure 4.16. A secondary phase, $Cu_2SnS_3$, indicating an incomplete sulfurization, is observed in the film sulfurized at 600ºC for 2 hours, but this phase disappears after longer sulfurization anneals.

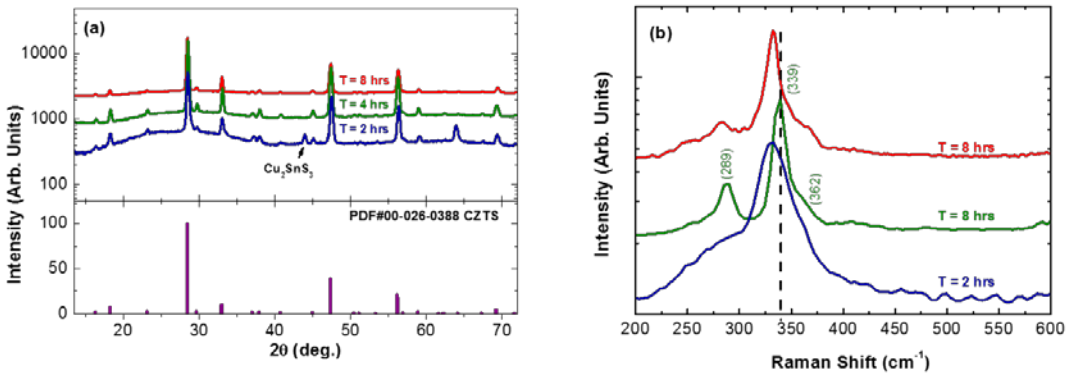


**Figure 4.16 (a) X-ray diffraction results, and (b) Raman scattering results for CZTS thin films sulfurized for 2, 4, and 8 hours at 600 ºC.**

As shown in Figure 4.17 (a) and (b), films with the stacking sequence Cu/Sn/Cu/Zn deposited on Mo-coated SLG show kesterite CZTS characteristics irrespective of anneal time. Both Mo and $MoS_2$ peaks show that excessive sulfurization can cause a significant amount of $MoS_2$ formation at CZTS/Mo interface during the annealing process. The two strongest Raman peaks at 287 $cm^{-1}$ and 338 $cm^{-1}$ are consistent with the kesterite CZTS phase. The peak at 368 $cm^{-1}$ can also be indexed to CZTS [95]. The shoulder seen from 350-355 $cm^{-1}$ can be attributed to the ZnS phase. For shorter anneal times, a small peak near 250 $cm^{-1}$ arises from the convolution of peaks corresponding to CZTS, $Cu_{2-x}S$, $Sn_2S_3$ and ZnS [141]. Figure 4.17 (a) and (b) show that film sulfurized for 4 hours is phase-pure

CZTS and Figure 4.17 (c) demonstrates that all sulfurized thin films are nearly stoichiometric. The thicknesses of metal layers in precursor stack can be adjusted to tune the film composition and final thickness. CZTS film sulfurized at 600 $^{o}$C for 4 hours on Mo-coated SLG was quite uniform with grain size of about 1 micron as shown in Figure 4.17 (d). Importantly, this stacking order greatly improved lateral uniformity.

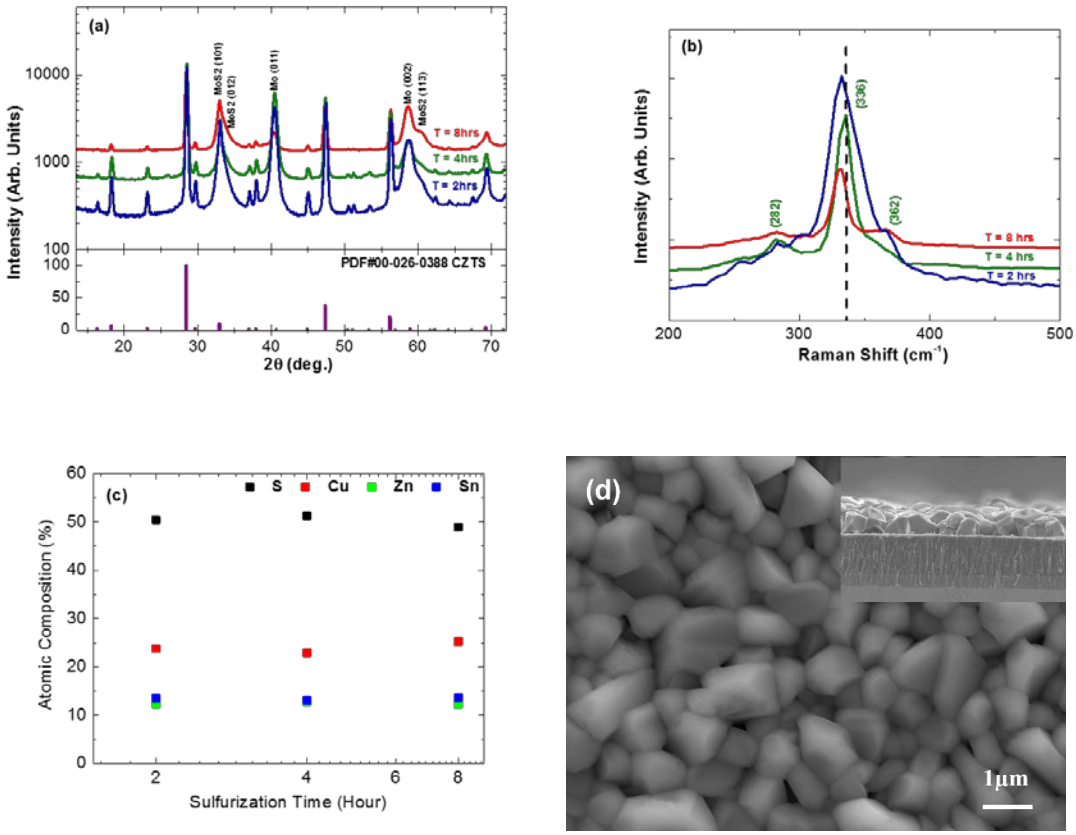


**Figure 4.17 (a) X-ray diffraction results, (b) Raman scattering results, (c) EDS results for CZTS thin films sulfurized for 2, 4, and 8 hours, and (d) Top view and cross-section SEM images of CZTS sulfurized for 4 hours.**

We used SEM images to estimate the grain size of CZTS thin films. A random straight line was drawn through the micrograph. The number of grain boundaries intersecting the line was then counted. The average grain size is found by dividing the number of intersections by the actual line length. The level of magnificent was kept low to improve statistics.

We find that the CZTS grain size is much larger when some of the SLG is exposed or if we put an extra piece of SLG into the ampoule during sulfurization process, as shown in Figure 4.18. This suggests that some impurity from the SLG is transported through the vapor and helps grain growth. This impurity transports readily in a sulfur ambient, presumably by forming a volatile sulfur-containing compound, but diffuses more slowly through the Mo layer, requiring a longer anneal time for Mo-coated SLG compared to uncoated SLG to obtain the desired grain-growth effect.

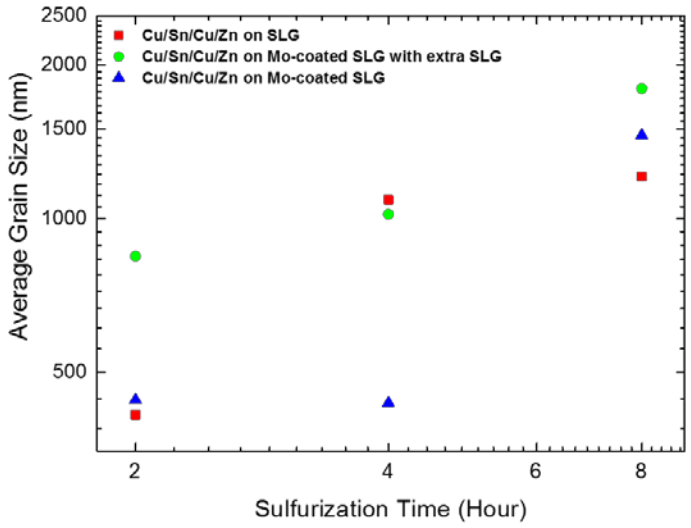


**Figure 4.18 CZTS grain size under different sulfurization time.**

Further experiments on the stacking order showed that moving the intermediate copper layer to the top of the stack (Cu/Sn/Zn/Cu) actually produces an even more uniform Zn rich CZTS thin film. At first glance this appears to be in contrast to the observations made above: putting Zn and Sn into contact permits the formation of very low melting temperature eutectics, which ultimately leads to droplet formation. However, putting the coper layer on top of the stack constrains the formation of droplets. Surface tension between the eutectic and both top and bottom copper layers forces the molten eutectic to spread into a uniform molten layer. Such a structure may be beneficial. The liquid eutectic will have a high diffusivity for Cu, allowing uniform, large grain growth.

## 4.5 Back Contact Metal Material Influence on CZTS Properties

Stoichiometric and uniform CZTS thin film with grain size around 1 μm were obtained using a bare SLG as substrate, which was also proven by EDS, XRD and Raman scattering results. However, switching to Mo-coated SLG substrate created difficulties of producing CZTS thin film with desirable morphology.

The resistivity, film stress, and adhesion of single layer Mo thin film deposited on SLG with various sputtering pressure (0.5 mT to 10 mT) were tested. It is found that under low chamber pressure (0.5 mT-1 mT), high energy bombardment of atoms at the surface produces compressively stressed films. These thin films are very dense and have a low resistivity, but also have poor adhesion to substrate due to a large intrinsic stress. With increasing chamber pressure (1 mT-5 mT), gas phase collisions decelerate sputtered species and reduce the energy of adatoms on the substrate. Thin film growth follows the "Island-mode" mechanism and voids and spaces form between free-standing columns. The interatomic forces between the columns produce tensile stress in the films. These films are low resistive with better adhesion to substrate. Under high chamber pressure (5 mT-10 mT), gas phase collisions further reduce adatom energy. Interatomic forces between columns diminishes and porous structure created by these columns further reduces tensile stress. The films are more resistive but have good adhesion.

To produce a low resistive Mo back contact with good adhesion to the substrate, a bi-layer structure (a compressive stressed low resistive layer on top of a tensile stressed high resistivity layer) was proposed. This bi-layer configuration proved to successfully fabricate low-resistivity Mo thin film on SLG substrate with good adhesion for CIGS PV [128]. It has been used as back contacts for CIGS and CZTS based solar cells for years. To further study the changes of Mo stress, morphology, and the adhesion to CIGS/CZTS thin films after a heat treatment, Karthikeyan *et al.* in our group did a series of in-situ studies to develop a thermally stable Mo bilayer for CIGS/CZTS PV applications [180]. In this study, four different Mo thin films were deposited using sputtering system. Bottom layer with thickness of 50 nm, 150 nm, 250 nm, and 500 nm were tested while the top layer thickness was adjusted to keep the total Mo film thickness about 1 μm, as shown in table 4.4.

**Table 4.4 Four different configurations of Mo bi-layers.**

| | **5 mT bottom layer (nm)** | **1 mT top layer (nm)** |
|---|---|---|
| **S1** | 50 | 950 |
| **S2** | 150 | 850 |
| **S3** | 250 | 750 |
| **S4** | 500 | 500 |

Mo stress variation during anneals ranging from 20 $^{o}$C to 500 $^{o}$C were measured. Basically, there are two critical factors can cause changes in the stress: (i) The coefficient of thermal expansion (CTE) of Mo ($4\times10^{-6}$ $K^{-1}$) is lower than that of SLG ($9\text{-}9.95\times10^{-6}$ $K^{-1}$). As a result, Mo back contacts are put under increased tensile stress during the high temperature sulfurization of Cu-Zn-Sn precursors (ii) Softening of SLG occurs at high temperature. This can change the residual stress and adhesion of the Mo films. Dense compressively films have large elastic modulus that can induce high stress during thermal annealing. In turn, they have a higher stress relaxation during cooling and results in more compressively stressed films after cooling. The S4 sample has a 500 nm porous bottom layer. Its thermal stress will be low compared to other films resulting in less stress relaxation.

The resistivity of Mo thin films before and after 500 $^{o}$C anneal were also measured and shown in Figure 4.19.

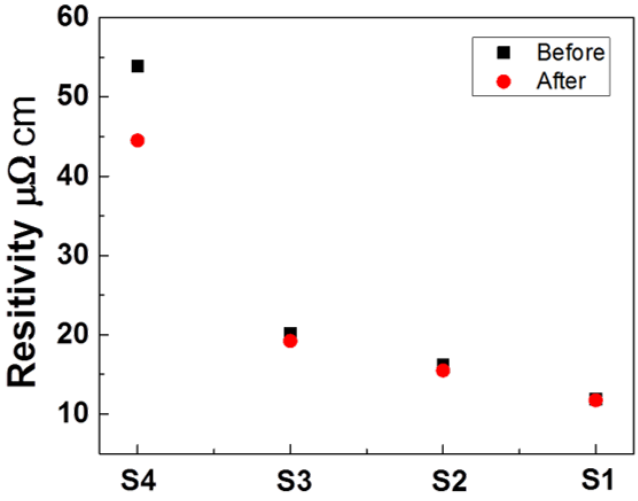


**Figure 4.19 The resistivity of Mo thin films before and after 500 ºC anneal.**

S1 sample showed the lowest resistivity, however the adhesion and film thermal stability was poor. The resistivity of S4 sample was very high because of its thick porous bottom layer. In summary, S2 and S3 configurations showed good electro mechanical properties for a robust back contact layer for PV applications.

CZTS thin films were grown on all these four Mo back contacts under the same sulfurization conditions. Morphologies of CZTS films are shown in Figure 4.20. It is clear that the grain size of CZTS deposited on S2 sample is the largest (~1 μm) while CZTS on S1 sample has the smallest grains. The extensive grain growth of CZTS on S2 is probably due to the enhanced nucleation sites with the rougher surface of the S2 configuration.

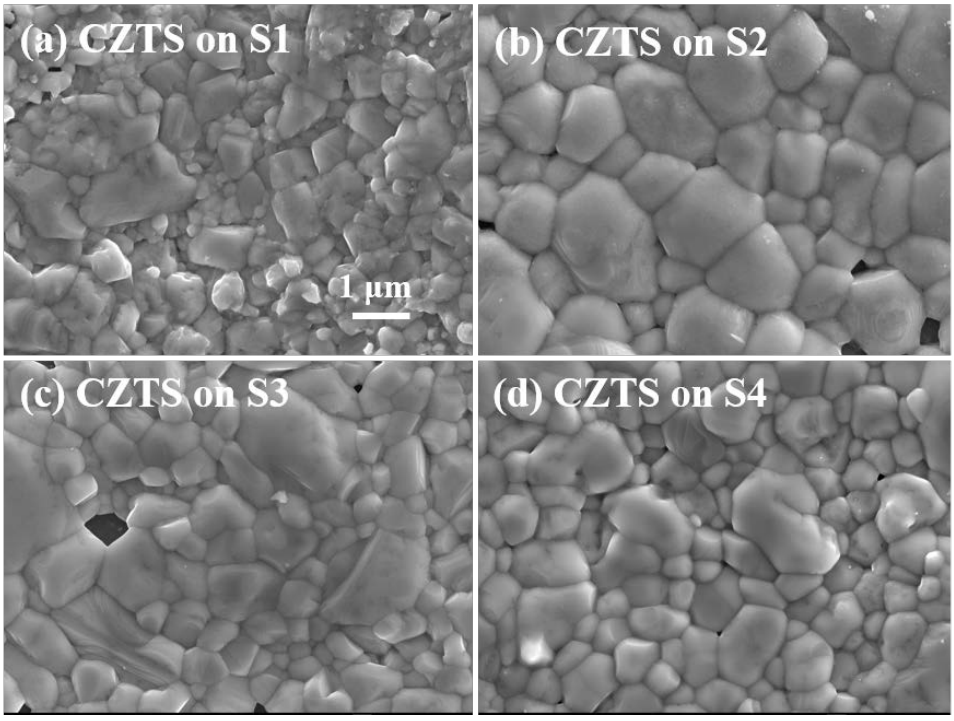


**Figure 4.20 SEM images of CZTS deposited on Mo films with (a) S1, (b) S2, (c) S3, and (d) S4 configurations.**

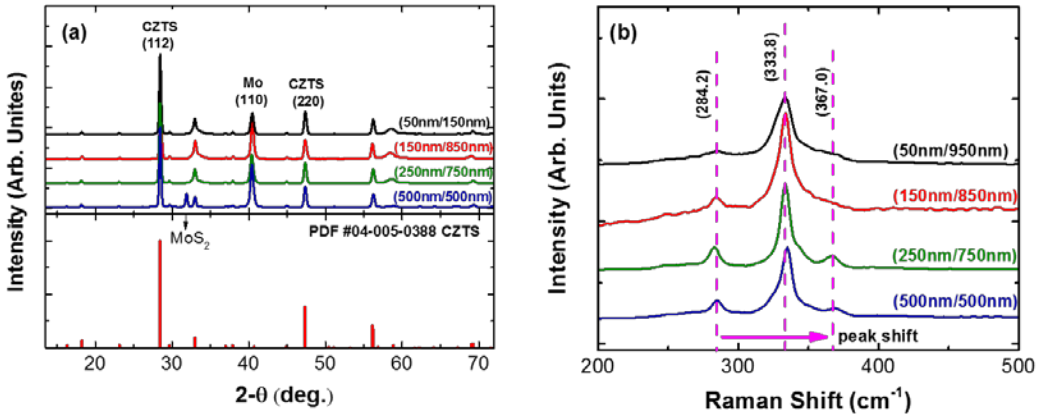


**Figure 4.21 (a) X-ray diffraction results, (b) Raman scattering results of CZTS deposited on Mo films of S1, S2, S3 and S4 configurations.**

As shown in Figure 4.21 above, for CZTS deposited on S1, S2, and S3, all the XRD peaks aligned to CZTS. As for CZTS grown on S4, a peak at 32.68 $^{o}$ which corresponds to $MoS_2$ (100) was observed. A Raman main peak at 333.8 $cm^{-1}$ shifted to longer wavelength (335.1 $cm^{-1}$) with increasing the thickness of bottom layer Mo. The Raman spectra of CZTS depends on the statistical disorder in the Cu and Zn cation sublattice. This disorder may initiate a change of the crystal symmetry from kesterite-type ($I4$) to the ($I42m$) space group [154]. In most cases, CZTS crystals grown at high temperature are characterized as the co-existence of regions with different composition ratio of Cu/(Zn + Sn) which results in kesterite and disordered kesterite phases. Disordered phase with the ($I42m$) symmetry is shown as a dominant broadened A-symmetry peak at lower wavelength than the peak of the main A-symmetry kesterite structure at 337 $cm^{-1}$. The red shift of the main peak means that the CTZS disordered phase is reduced when deposited on S4. Meanwhile EDS results (Table 4.5) show the Cu poor/Zn rich composition of CZTS on S4 which might be responsible for the Raman peak shift.

**Table 4.5 EDS results of CZTS deposited on Mo films of S1, S2, S3 and S4 configurations.**

| Sample | S Atomic % | Cu Atomic % | Zn Atomic % | Sn Atomic % | Cu/(Zn +Sn) | Zn/Sn |
|---|---|---|---|---|---|---|
| **CZTS on S1** | 51.0 | 23.5 | 12.4 | 13.1 | 0.92 | 0.95 |
| **CZTS on S2** | 50.3 | 24.2 | 12.2 | 13.3 | 0.95 | 0.92 |
| **CZTS on S3** | 50.6 | 23.9 | 12.3 | 13.2 | 0.94 | 0.93 |

| | | | | | | |
|---|---|---|---|---|---|---|
| **CZTS on S4** | 50.3 | 23.6 | 14.5 | 11.6 | 0.9 | 1.25 |

Even though S4 Mo produced CZTS thin film with less disorder phases, it was highly resistive and therefore not an optimal back contact. Based on previous discussions, the S2 configuration was chosen as the default CZTS back contact in later research. The thickness of different metal precursor layer can be controlled to tune the CZTS chemical composition and crystal structures.

Searching for possible back contact metals for CZTS solar cell application, 13 different metals that can make ohmic contacts with CZTS were taken into consideration, as shown in table 4.6.

**Table 4.6 The properties of possible contact metals.**

| **Metals** | **Work Function (eV) [181]** | **Coefficient of Thermal Expansion ($\times 10^{-6}\,K^{-1}$) [181]** | **Resistivity ρ ($\times 10^{-6}\,\Omega\cdot cm$) [182, 183]** | **Price (USD) [184, 185]** |
|---|---|---|---|---|
| **Mo** | 4.36-4.95 | 5 | 5.34 | 8.0/lb |
| **Cr** | 4.5 | 6.2 | 12.5 | 1.05/lb |
| **Al** | 4.06-4.26 | 22.2 | 2.82 | 0.7/lb |
| **Ti** | 4.33 | 8.6 | 42.0 | 8.6/lb |
| **Fe** | 4.67-4.81 | 12 | 10.0 | 52.15/t |
| **Co** | 5.0 | 12 | 6.24 | 13.65/lb |
| **Ni** | 5.04-5.35 | 13.0 | 6.99 | 4.76/lb |

| | | | | |
|---|---|---|---|---|
| **Ag** | 4.26-4.74 | 19.5 | 1.59 | 15.33/ozt |
| **Au** | 5.1-5.47 | 14.2 | 2.44 | 1117.4/ozt |
| **Pt** | 5.12-5.93 | 9.0 | 10.6 | 1600.5/ozt |
| **W** | 4.32-5.22 | 4.3 | 5.6 | 27.72/lb |
| **Ta** | 4.0-4.8 | 6.5 | 13.1 | 140/lb |
| **Pd** | 5.22-5.6 | 11.8 | 10.54 | 1613/ozt |

Among the back contact candidates, Ag, Au, Pt, and Pd were ruled out because of their high price. As for ferromagnetic metals around room temperature, Fe is easily oxidized, while Co is toxic and Ni has a low Curie temperature (355 $^{o}$C) which might cause a change of Ni film during sulfurization process. Looking for other candidates with lower electrical resistivity, Mo, Cr, Al, and Ti are chosen as back contact candidates of interest.

CZTS thin film were deposited on SLG coated with these four metals. As shown in the SEM images in Figure 4.22, CZTS deposited on Mo was close-packed with large grains. While CZTS films grown on other metals have smaller grain size. It is also shown in cross-section images that Mo back contact has a columnar structure, while other metals don't. This structure might be beneficial to Na diffusion into Cu-Zn-Sn precursors and be useful to enhance the grain growth. Meanwhile, Cr, Al, and Ti will react with Zn, Sn or Cu in the precursors and this reaction might also slow the CZTS growth process. This is supported by XRD results (Fig. 4.23).

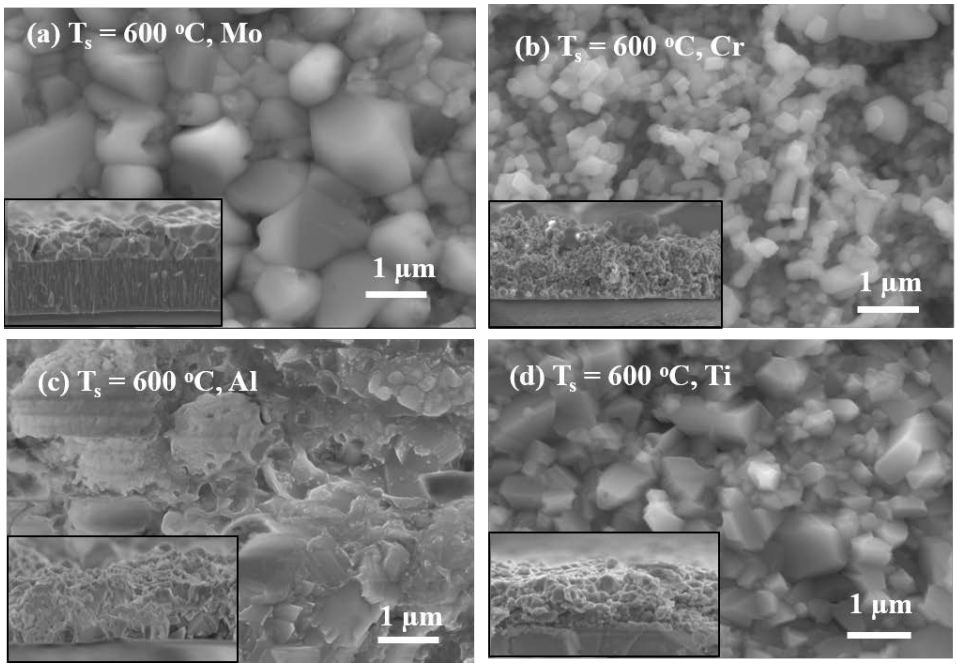


**Figure 4.22 Top view and cross-section SEM images of CZTS deposited on (a) Mo-coated SLG, (b) Cr-coated SLG, (c) Al-coated SLG, (d) Ti-coated SLG.**

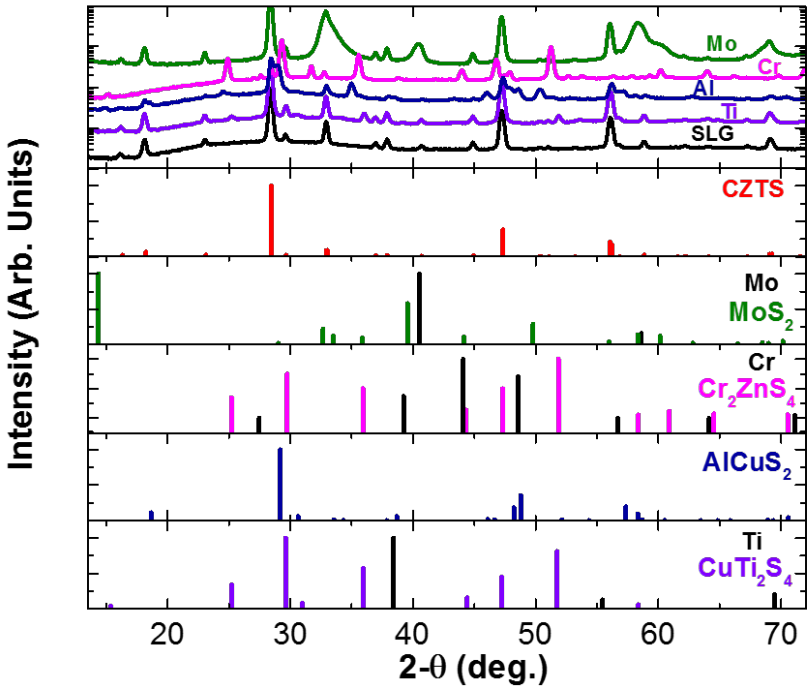


**Figure 4.23 X-ray diffraction results of CZTS deposited on Mo, Cr, Al, and Ti-coated SLG.**

## 4.6 Conclusions

An optimized two-step method of growing $Cu_2ZnSnS_4$ (CZTS) thin films was developed. Using it, it is possible to control the CZTS grain size and film morphology. Several factors that affect CZTS grain growth, such as sulfurization temperature, sulfurization time, the diffusion of impurities from the SLG through Mo or through the ambient, the stacking order of the precursor metal layers, and the back contact layer properties. The results show that control of the thin film composition can be achieved by precisely controlling the thickness of each metal layer during thermal evaporation. Considering the

requirements of an optimal CZTS film, we found that the precursor stacking sequence Cu/Sn/Cu/Zn precursors produced phase pure kesterite CZTS. Sulfurization at 600$^{o}$C for 4 hours with exposed SLG in the ampoule helps obtain a uniform film with grains about one micron in size.

In order to improve the efficiency of CZTS-based thin film solar cells, a deeper understanding of the fundamental properties and optimal preparation of CZTS material is important. Even though there is no consensus on which way is the best for the preparation of CZTS thin films [56], the process established here has the potential in promoting the development of low-cost CZTS thin film solar cells.

# Chapter 5

# 5 CZTS Thin Film Solar Cell Fabrication and Device Measurement

## 5.1 CZTS Thin Film Solar Cell Fabrication

### 5.1.1 Introduction

In this chapter, CZTS thin films with different chemical compositions were formed by thermal evaporation and a post-deposition sulfurization process. Completed solar cells were fabricated based on those CZTS thin films and device measurements were also conducted to study the relationship between film composition, carrier concentration and solar cell performance from an experimental point of view. Meanwhile, CZTS thin film morphology changes related to chemical composition variation and its influence on solar cell performance are also studied.

### 5.1.2 Experimental Details

The metal precursor layers (Cu, Zn, and Sn) were deposited in a stack on Mo-coated soda-lime glass substrates without breaking vacuum by thermal evaporation and then sulfurized at 560 $^{o}$C to obtain $Cu_2ZnSnS_4$ (CZTS) thin films. A lower temperature is used instead of the 600 $^{o}$C mentioned in the previous chapter, because a sulfurization temperature below SLG transition temperature (575 $^{o}$C) is beneficial to produce low stress CZTS. The thicknesses of metal layers in precursor stack were adjusted to tune the

film composition. Various precursors with different metal thicknesses were studied to determine the effect of the film chemical composition on the film properties and final solar cell performance. A Cu/Sn/Cu/Zn stacking order (from bottom to top) was used in this series of experiments as it proved to be able to make functional CZTS thin films in previous chapter. We tested Zn poor, stoichiometric, Zn rich and extremely Zn rich CZTS films, Zn/Sn = 0.91, 1.01, 1.24, 1.35 in this report, as shown in Table 5.1. We also tested a Cu/Sn/Zn/Cu precursor and fabricated a CZTS solar cell using this absorber layer.

**Table 5.1 Summary of CZTS deposition conditions.**

| Sample Number | | Precursor (Cu/Sn/Cu/Zn) | | | | After Sulfurization | |
|---|---|---|---|---|---|---|---|
| | | Cu (nm) | Zn (nm) | Sn (nm) | Total (nm) | Cu/(Zn+Sn) | Zn/Sn |
| 1 | Zn poor | 299.9 | 199.4 | 342.8 | 842.1 | 0.98 | 0.91 |
| 2 | Stoichiometric | 288.8 | 206.1 | 342.8 | 837.7 | 0.92 | 1.01 |
| 3 | Zn rich | 264.9 | 217.9 | 342.7 | 825.5 | 0.87 | 1.24 |
| 4 | Extremely Zn rich | 265 | 235.5 | 343.7 | 844.2 | 0.83 | 1.35 |

The device structure used for CZTS solar cells is identical to that used for CIGS solar cells, except for the substitution of CZTS for CIGS. The device stack was formed using a SLG substrate, a sputtered bi-layer Mo back contact, thermally evaporated CZTS,

chemical bath deposited (CBD) CdS, a sputtered ZnO/ITO double layer, and sputtered Ni/Al grids, as shown in Figure 5.1. No wet etching of the absorber was done to eliminate secondary phases.

Current-voltage (I-V) measurements were performed under simulated AM 1.5 solar spectrum with 100 mW/cm$^2$ (1 sun) illumination. Standard capacitance-voltage (C-V) measurement and analysis techniques [169] were utilized to estimate the concentration and defect level near the CZTS/CdS heterojunction. This method relies on the fact that the width of a reverse-biased space-charge region (SCR) of a semiconductor junction device depends on the applied voltage and assumes that charge is limited to carriers and ionized acceptors. A Hewlett-Packard 4194A Precision Impedance Analyzer was used to measure capacitance as a function of voltage, at room temperature, from -3V to +1V. The ac signal applied was 0.1V at 200 kHz. The carrier concentrations as a function of voltage and also the distance from the junction were derived from the C-V data. The defect concentration distribution near heterojunction interface has a strong influence on the electronic properties of the device and also the efficiency of solar cells.

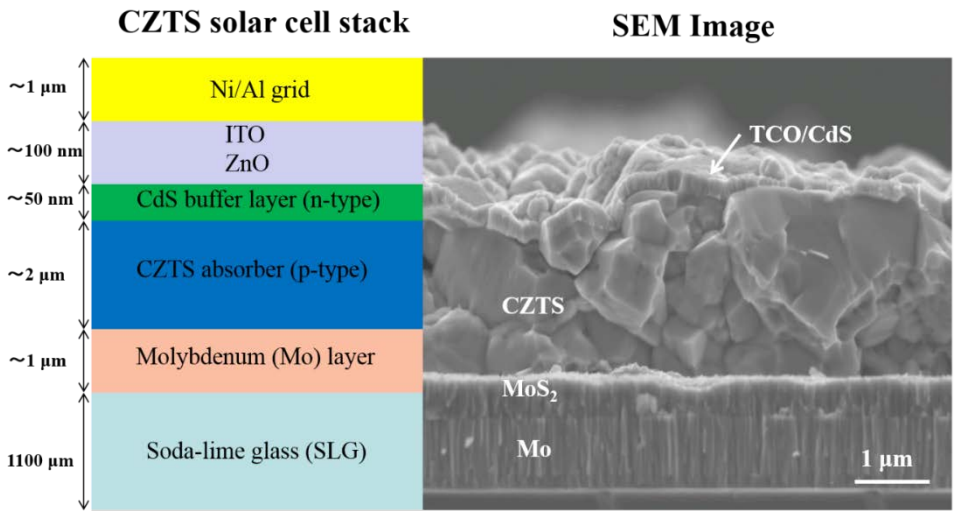


**Figure 5.1 Schematic representation of the final CZTS solar cell.**

## 5.2 Chemical Composition Dependence on CZTS Thin Films

Prior to thin film solar cell fabrication, CZTS absorbers were characterized using X-ray diffraction, Raman scattering, SEM and EDS. The influence of the chemical composition on CZTS film structural properties and morphologies was studied. XRD results collected from samples on Mo-coated SLG (Cu/Sn/Cu/Zn precursor metal stacks) which were sulfurized from precursors with various chemical compositions have shown that kesterite CZTS thin films were produced (Figure 5.2 (a)). Similarly the two strongest Raman peaks at 284.2 $cm^{-1}$ and 335.1 $cm^{-1}$ are consistent with the kesterite CZTS phase. The peak at 368 $cm^{-1}$ can also be indexed to CZTS [95]. The shoulder seen from 350-355 $cm^{-1}$ can be attributed to the ZnS phase; it confirms that CZTS-4 is Zn rich as shown in Table 5.1. CZTS grains are close-packed with an approximate size of 1 micron (Fig. 5.3). No

clear relationship is seen between thin film chemical composition and grain size. However, non-uniformity is observed in some areas for Zn rich samples CZTS-3, and CZTS-4. As a result, the film is divided to two regions with different Zn compositions, as shown in Figure 5.6 (a) and (b). The bright area with many tiny grains is Zn rich, while the darker area with normal grain size is stoichiometric. This non-uniformity occurs during the sulfurization process and is probably due to insufficient inter-diffusion between precursor metals. This phenomenon brings up the idea of switching Cu and Zn layer and making Cu the top layer, which will be explained in detail soon.

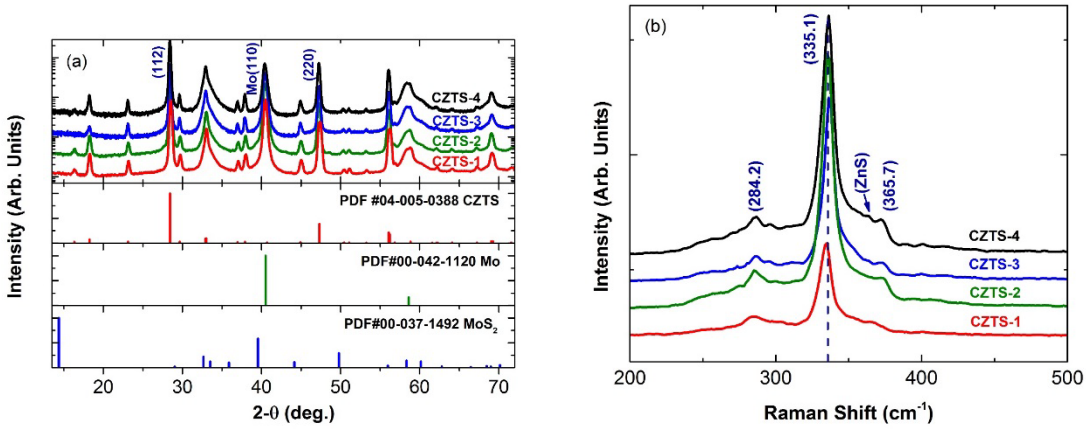


**Figure 5.2 (a) X-ray diffraction, and (b) Raman scattering results of CZTS thin films with different chemical compositions.**

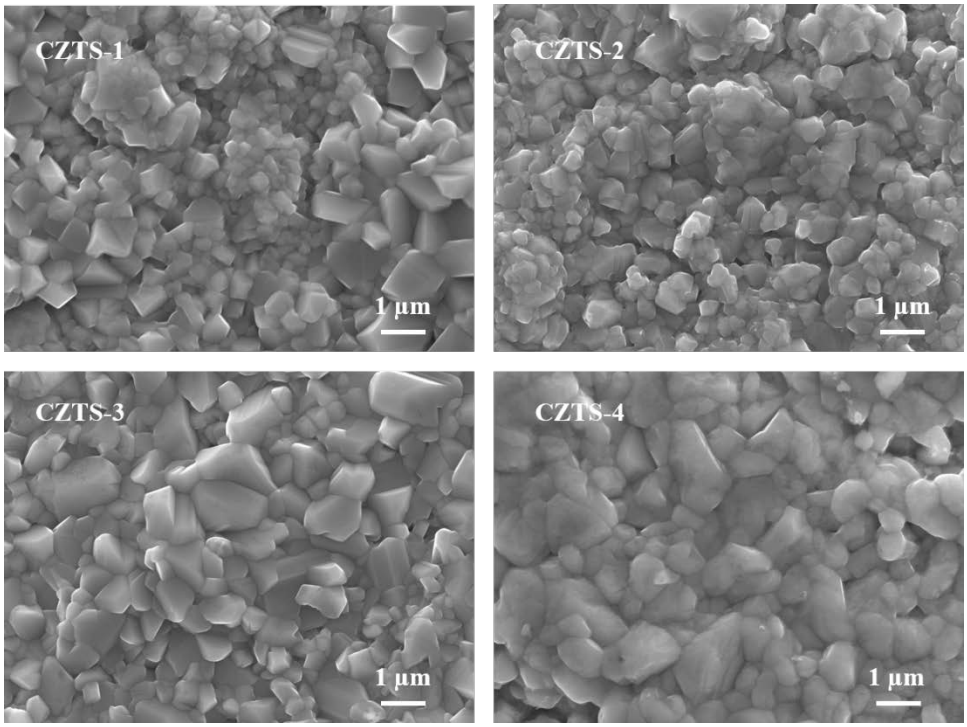


**Figure 5.3 SEM images of CZTS thin films with various chemical composition.**

## 5.3 Chemical Composition Dependence on CZTS Solar Cell Performance

Figure 5.4 (a) shows that higher carrier concentration appears near the CZTS/CdS interface and carrier concentration decreases with increasing the reverse bias applied for solar cell fabricated from CZTS thin films. Clearly one can vary the carrier concentration over several orders of magnitude by changing the composition. It appears from the CV results that the carrier concentration profile is not uniform, instead varying with depth into the absorber. This might be caused by some defects or interface effects. For example, Zn poor or stoichiometric film composition might suppress the $V_{Cu}$ defect formation and relatively enhance the formation of $Cu_{Zn}$ antisite defect which cause the higher carrier

concentration. It is also possible that the CV technique is measuring the response of traps at or near the CZTS/CdS interface, as well as the majority carrier response. This is consistent with the carrier concentration profile reported for solar cells fabricated from CZTS-1 and CZTS-2.

The carrier concentration profile influences the device performance very directly. If the concentration is too high, the depletion width is narrow and carrier collection is poor. If the carrier concentration is low, the absorber is fully depleted, also leading to poor performance. Doping gradients create electric fields that can either aid or hinder carrier transport. Figure 5.4 indicates profiles that are increasing with voltage, which means carrier concentrations are decreasing with depth. This leads to band bending that will obstruct the transport, however shallow peaks in the profiles, as shown by several samples, will improve carrier collection since the doping profile beyond the peak creates an electric field pointing toward the CZTS thin film.

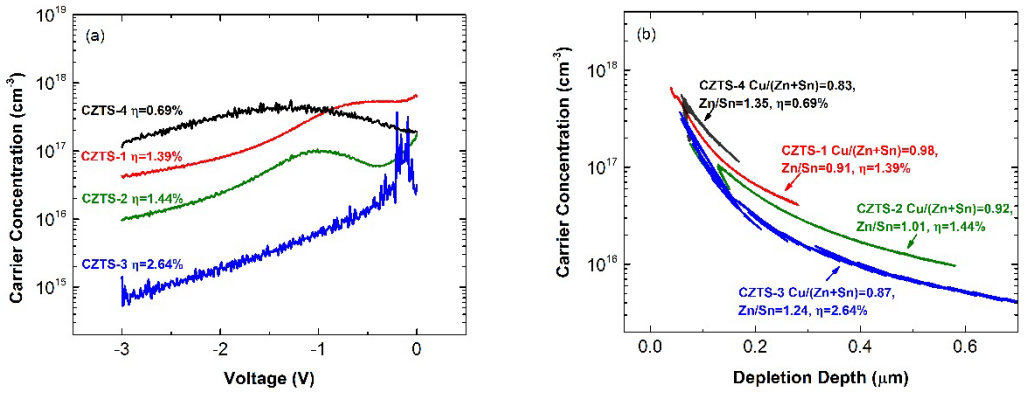


**Figure 5.4 Carrier concentration profiles of CZTS thin films with different chemical compositions, (a) carrier concentration vs. voltage curve, and (b) carrier concentration vs. depletion depth curve.**

We observe that increasing the Zn/Sn ratio and decreasing the Cu/(Zn+Sn) ratio lead to lower carrier concentration and better solar cell performance. Figure 5.5 shows an efficiency of 1.39%, 1.44%, 2.64%, and 0.69% for solar cell CZTS-1, CZTS-2, CZTS-3, CZTS-4, respectively, for a total area of 0.126 $cm^2$. These values were achieved without using an anti-reflecting layer. The optimal composition of CZTS absorber for making solar cells (Cu/(Sn+Zn)=0.8-0.95, Zn/Sn=1.1-1.25) in order to form primary defect $V_{Cu}$ in CZTS absorber is confirmed in this study. However, the carrier concentration starts to grow and solar cell performance drops if the Zn/Sn ratio is too large, as shown in Figure 5.5. Also, it is observed that $J_{sc}$ increases almost 70% when Zn/Sn ratio changes from ~0.9 to 1.24, but drops to only half of the value when Zn/Sn increases further to 1.35. This demonstrates the narrow region of optimal CZTS thin film chemical composition.

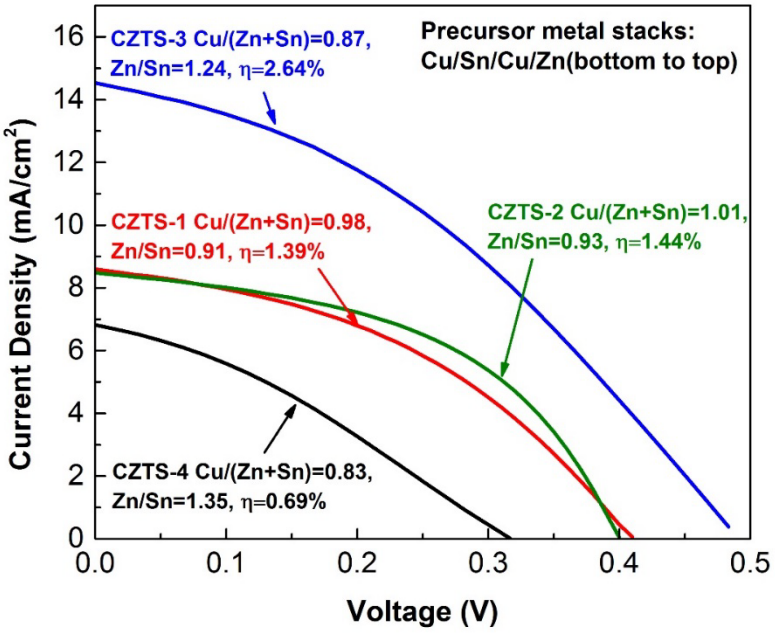


**Figure 5.5 I-V curve for solar cells fabricated from CZTS thin films with different chemical compositions.**

The efficiency is limited partly by FF which shows low shunt resistance ($R_{sh}$) and high series resistance ($R_s$). The J-V measurement results also show a cross-over of dark and light J-V curve which indicates large $R_s$. It will be discussed in detail in Chapter 6. Secondly, the low conversion efficiency is due to relatively low $J_{sc}$ which is a characteristic of high recombination losses in bulk and at interfaces and inefficient carrier collection. Thirdly, due to a non-optimum grid design, an estimated 20% of the total area is covered by the grid. A lower $J_{sc}$ is expected for a solar cell with reducing active area.

## 5.4 Morphology Dependence on CZTS Thin Film Solar Cell Performance

As previously mentioned, the chemical composition influences the film morphology of CZTS, and further the solar cell performance. When Cu/(Zn+Sn) ratio is decreased and Zn/Sn ratio is increased, we frequently observe CZTS non-uniformity. To be specific, more ZnS precipitates appear on the surface of CZTS thin film and this non-uniformity of Zn distribution hinders CZTS grain growth. As a result, areas with small grains are always found to be Zn rich, while other areas are stoichiometric (Fig. 5.6). This non-uniform morphology might be responsible for higher recombination losses and lower carrier collection efficiency as discussed before.

Based on our four-layer precursor stacks discussed in a previous section, we fine-tuned the CZTS thin film microstructure morphology and structural properties by looking at both the Cu/Sn/Cu/Zn and Cu/Sn/Zn/Cu metal precursor stacking order. The thicknesses of metal layers in precursor stacks were adjusted to tune the film composition.

Precursors with metal stacking orders Cu/Sn/Cu/Zn and Cu/Sn/Zn/Cu were sulfurized under the same conditions and structural and morphological characterizations were conducted for both thin films. For the CZTS thin films produced by Cu/Sn/Zn/Cu precursor, grains were close-packed with an approximate size of 1 μm (Figure 5.6 (d)). EDS results revealed that the CZTS thin film has a composition ratio of Cu/(Zn+Sn) = 0.82, and Zn/Sn = 1.35. However, in films produced by precursor stacks with Zn on top,

there are areas with extremely small grains as shown in Figure 5.6 (a) and (b). EDS results show that the small grain area is extremely Zn and S rich (Figure 5.7 (c)), suggesting zinc sulfide (ZnS) precipitates on the film surface when a precursor with Zn on the top is sulfurized. These areas are smaller than the three-layer Cu/Sn/Zn stack, but the still could be found.

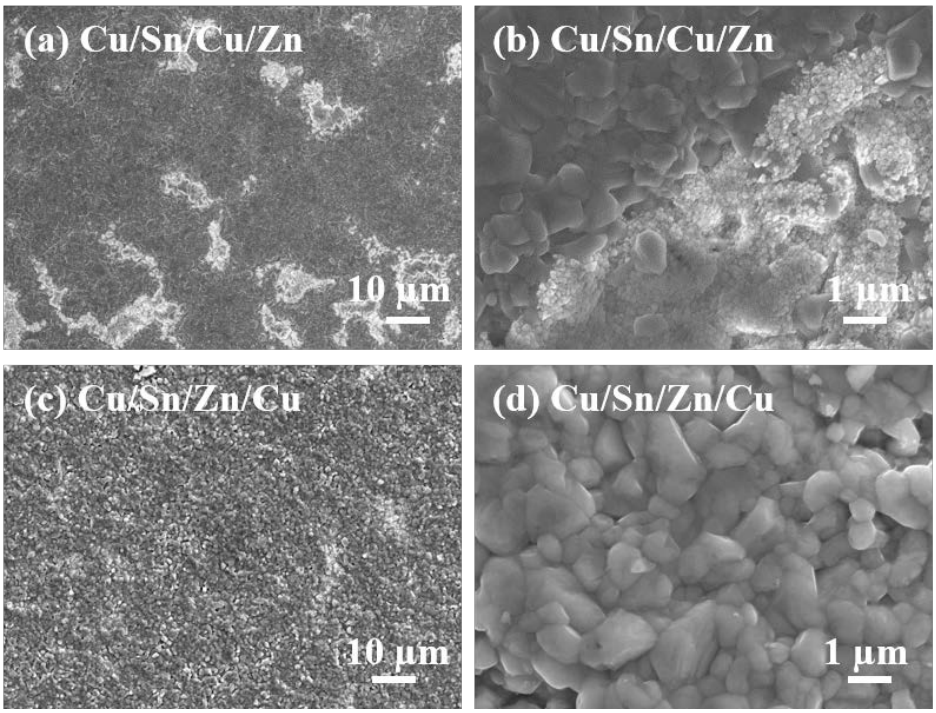


**Figure 5.6 SEM images of CZTS thin film produced by precursor (a) with Cu on top (lower magnification), (b) with Cu on top (higher magnification), (c) with Zn on top (lower magnification), and (d) with Zn on top (higher magnification).**

X-ray diffraction results of CZTS thin films showed they are in kesterite phase (Figure 5.7 (a)). However, for the thin film produced by precursor stacks with Zn on top, two small peaks at 27.62$^{o}$ and 48.62$^{o}$ (annotated by the blue stars) show the existence of ZnS

secondary phase. Similarly the two strongest Raman peaks at 284.8 $cm^{-1}$ and 335.3 $cm^{-1}$ were consistent with the kesterite CZTS phase. The 373.5 $cm^{-1}$ peak can also be indexed to CZTS [95]. However the feature at 350 $cm^{-1}$ again suggests the formation of ZnS. Solar cell fabricated using the CZTS thin film produced by Cu/Sn/Zn/Cu precursor as the absorber layer exhibited an open-circuit voltage of 433 mV, a short-circuit current of 7.78 $mA/cm^2$, a fill factor of 46.2% and a conversion efficiency of 1.56%, which is shown in Figure 5.7 (d).

The ZnS precipitated CZTS thin film solar cell fabricated from precursor with Zn on top shows lower conversion efficiency (1.16%) and fill factor (34.5%). As is known, ZnS has a band gap of 3.5-3.8 eV [55], making it behave as an insulator in CZTS thin films. This leads to a decrease of solar cell active area which explains the low short-circuit current. At the same time, ZnS precipitates are also responsible for the increase of device series resistance, decreasing the fill factor. The efficiency of solar cell fabricated from Cu/Sn/Zn/Cu precursor is also higher than the efficiency of Zn very rich solar cell (0.69%) in previous discussion, which makes it a consistent result. To reduce the secondary phase and non-uniformity issues, we standardized on the metal precursor stacking order Cu/Sn/Zn/Cu.

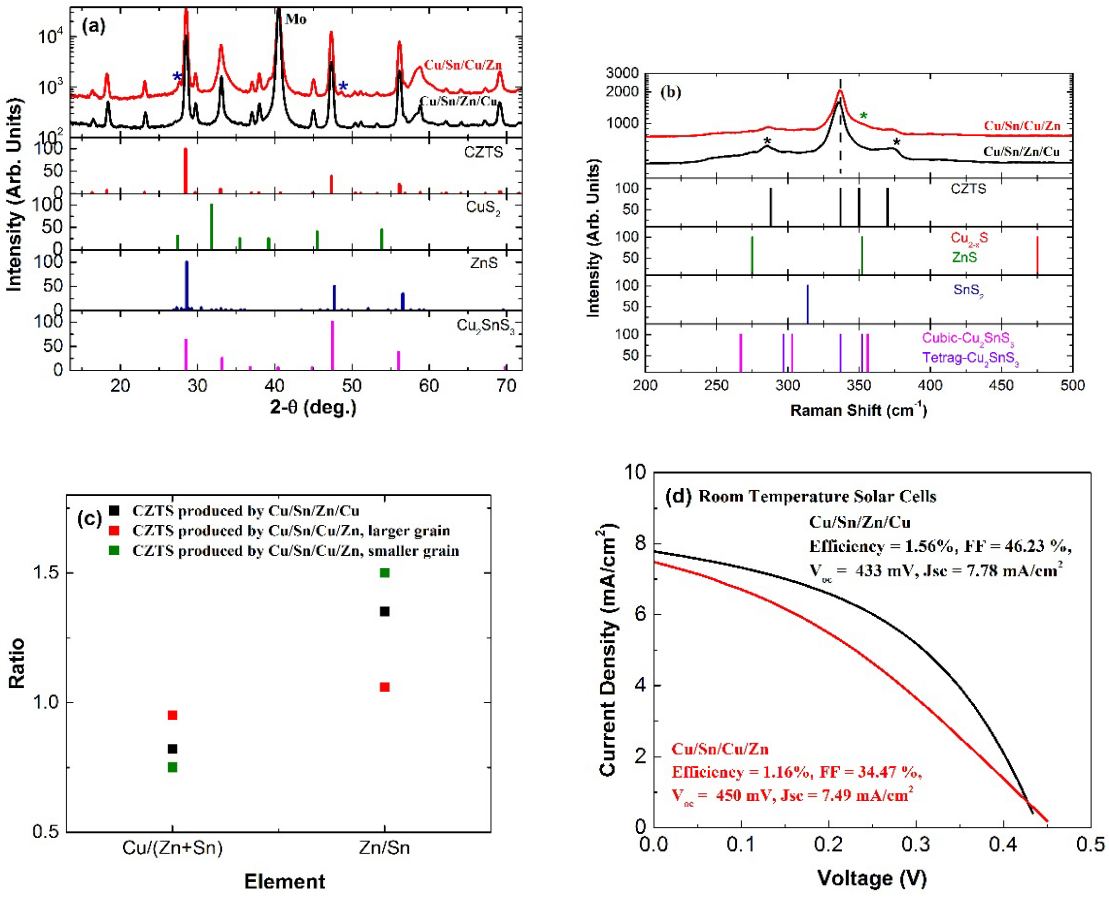


**Figure 5.7 X-ray diffraction results, (b) Raman scattering results, (c) EDS results, and (d) I-V characteristic of solar cells made of these CZTS thin films at room temperature.**

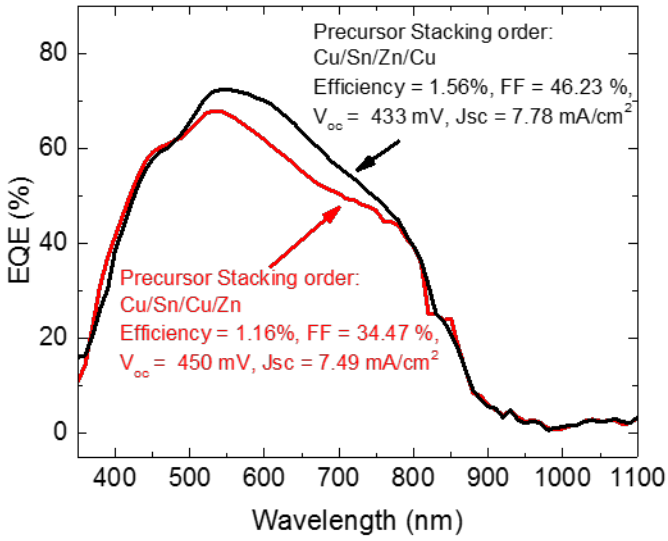


**Figure 5.8 EQE results of solar cells made of these CZTS thin films at room temperature.**

Figure 5.8 shows external quantum efficiency (EQE) spectrum of solar cells fabricated from these precursors. The EQE increases sharply around 350 nm, which is associated with window layer. The notch between 450 nm and 500 nm is in associated with absorption by the CdS buffer layer [186]. The maximum EQE is obtained at a photon wavelength of 550 nm. For longer wavelengths, ($\lambda$ > 600 nm), the EQE curve shows a weak response indicating very low collection efficiency due to higher recombination losses in the bulk and depletion region that leads to a short minority carrier diffusion length [100]. Then EQE drops rapidly to less than 50% of the maximum value at 800 nm and reduces to almost zero around 850 nm. Comparing these two solar cells, it is clear that both cells have similar EQE associated with window layer and buffer layer CdS. However, the maximum EQE obtained for solar cell produced from Cu/Sn/Zn/Cu

precursor is about 76%, while the other cell fabricated from precursor with Zn on the top has lower EQE and the maximum value is around 73%. EQE related to CZTS absorber layer shows that the carrier collection efficiency of two cells is different. CZTS synthesized from precursor with Zn on the top has higher recombination losses and then shorter minority carrier diffusion length compared to absorber produced from precursor with Cu on the top. It is probably due to the non-uniformity of CZTS absorber. The rapid diminishing tail shows very strong rear surface recombination and low minority carrier diffusion length.

The estimated band gap energy of CZTS film is 1.46 eV (almost no light is absorbed beyond 850 nm), in good agreement with earlier report for pure sulfide CZTS films. Further optimization in the composition and morphology of the CZTS absorber layer is needed to increase minority carrier lifetime and reduce recombination losses.

## 5.5 Conclusion

A two-step method of growing $Cu_2ZnSnS_4$ (CZTS) thin films was developed. Using it, it is possible to control the CZTS film chemical composition. Considering the requirements of optimal CZTS film, we first chose to use Cu/Sn/Cu/Zn precursors to grow phase pure kesterite CZTS. Sulfurization of metal stacks inside evacuated quartz ampoule at 560 $^oC$ for 4 hours helps obtain CZTS thin film with grains about one micron in diameter. We have fabricated CZTS solar cells with efficiencies of up to 2.64%. Through capacitance-

voltage measurement results, we have shown that CZTS thin film chemical composition affects its carrier concentration profile. For Cu-deficient films, the carrier concentration first decreases with increasing Zn/Sn ratio, but then increases sharply when the Zn/Sn ratio is increased from 1.24 to 1.35. Further study on detailed carrier concentration depth profile with various film compositions is needed.

Also, CZTS solar cells with efficiencies of 1.56% and 1.16% at room temperature were fabricated using CZTS thin films obtained from sulfurization of two different metal stack precursors Cu/Sn/Zn/Cu and Cu/Sn/Cu/Zn. It is suggested that precursors with Cu on the top provide more uniform CZTS thin films with fewer ZnS secondary phase and therefore produce higher efficiency solar cells.

# Chapter 6

# 6 Post Deposition Rapid Thermal Annealing (RTA) of CZTS Solar Cells

## 6.1 RTA of CZTS Thin Films and Solar Cells

### 6.1.1 Introduction

The conversion efficiency of CZTS thin film solar cells is improving, but is still well below the level required for commercialization. To a large extent, this is due to the difficulty of controlling the CZTS film morphology and chemical composition. In this project, CZTS thin films were produced from thermally-deposited metal precursor stacks followed by an ex-situ sulfurization process. To improve the microstructure morphology and properties of CZTS, various approaches have been studied, such as tuning the thin film chemical composition, testing different metal precursor stacking orders, and optimizing back contact metal deposition. Besides optimizing CZTS synthesis, post deposition rapid thermal annealing (RTA) of complete CZTS solar cells was also investigated since it has been shown to improve CIGS solar cell performance, as discussed in Chapter 2 in detail. The absorber bulk carrier concentration and defect level at p-n interface were studied by C-V measurement. Further the influence of post deposition RTA on CZTS solar cell performance was also explored. The motivation of this work is to apply this approach to CZTS thin film solar cells and to study the

relationship between post deposition RTA conditions, CZTS thin films, CZTS/CdS interfacial defect concentration and solar cell performance.

### 6.1.2 Experimental Details

A Cu/Sn/Zn/Cu metal precursor stacking order (from bottom to top) was used in this set of experiments as it proved to be able to make functional CZTS thin films with better uniformity as described in a previous chapter. CZTS thin films were synthesized under optimized conditions, and cut into two pieces. One piece was used to investigate the effect of post RTA on CZTS thin film properties by forming Schottky junctions with Al deposition. The other one was used for CZTS thin film solar cell fabrication following the standard procedures discussed in Chapter 5. Both the CZTS thin films and solar cells went through the same post RTA cycles, which were conducted sequentially at 150 $^{o}$C, 200 $^{o}$C, 250 $^{o}$C, 300 $^{o}$C, 350 $^{o}$C and 400 $^{o}$C for 30 seconds in a $N_2$ atmosphere, respectively. We then investigated the effect of post RTA on the CZTS thin films and CZTS solar cell performance separately. In this way, it was possible to separate the change or improvement of the CZTS absorber material characteristics and the CZTS/CdS p-n interfacial properties. We assume the alteration of ZnO/ITO layer and Ni/Al top contact is negligible.

I-V and C-V measurements were carried out after each annealing step to study the post RTA effect on CZTS solar cell performance. The short circuit current density ($J_{sc}$), open

circuit voltage ($V_{oc}$), fill factor ($FF$), and conversion efficiency ($\eta$) are the major cell characteristics of interest. In order to address the effect of post RTA on CZTS thin film properties, film crystalline structure, microstructure morphology, and chemical composition were characterized after each anneal.

### 6.1.3 RTA Temperature dependence on Solar Cell Efficiency Improvement

Post deposition RTA was done on a solar cell with 1.56% efficiency at room temperature. Electrical test results showed that the solar cell performance improved with the increasing RTA temperature, reaching the highest performance after annealing at 350 $^{o}$C. However, the $J_{sc}$, $V_{oc}$, and $FF$ dropped sharply after a 400 $^{o}$C anneal (Fig. 6.1). More details about how the solar cell properties change with the increasing RTA temperature are shown in Figure 6.2.

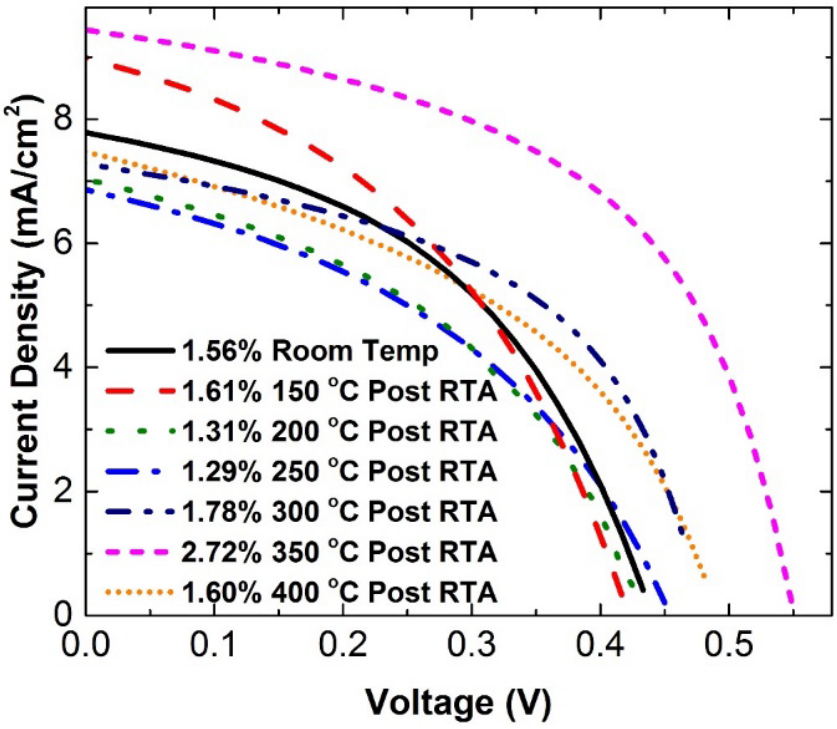


**Figure 6.1 Solar cell I-V characteristics at room temperature and different post RTA temperatures.**

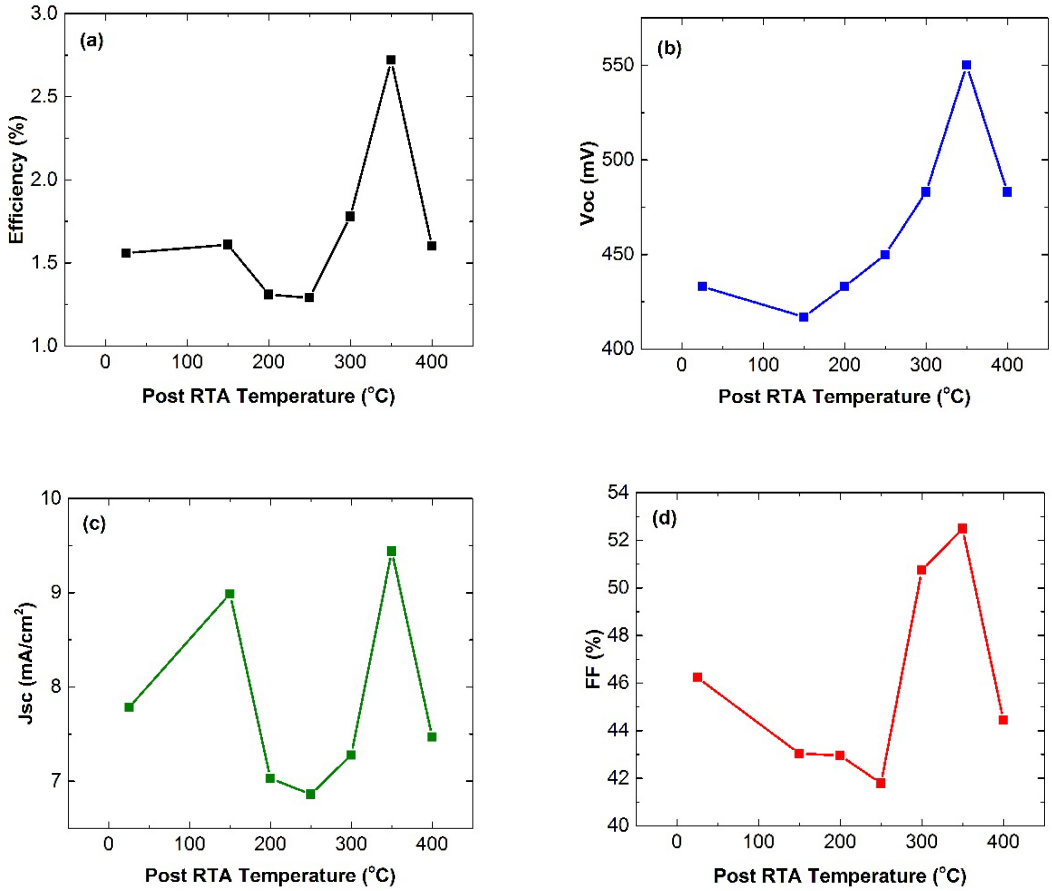


**Figure 6.2 (a) Solar cell conversion efficiency, (b) $V_{oc}$, (c) $J_{sc}$, and (d) FF at room temperature and different post RTA temperatures.**

If the CZTS device follows the same behavior as CIGS solar cells, one might expect that the annealing process leads to Cd diffusion into the absorber. This may lead to a displacement of the p-n junction away from the hetero-interface, reducing interfacial recombination. Doping compensation may also increase the depletion width, thereby

improving the carrier collection. It is also possible that the annealing process simply improves the CZTS absorber properties or the interface by reducing the trap density.

## 6.2 RTA temperature dependence on CZTS/CdS interfacial properties

In order to study the relationship between CZTS/CdS interfacial properties and post RTA temperature, C-V measurements were conducted after each annealing step. With annealing, the CZTS/CdS interfacial defect concentration first increases with increasing RTA temperature and starts to decrease at 350 $^{o}$C. Accordingly, the zero bias depletion width in the absorber decreases first, but increased at 350 $^{o}$C. Meanwhile, increasing RTA temperature shifts the zero bias depletion depth to smaller values.

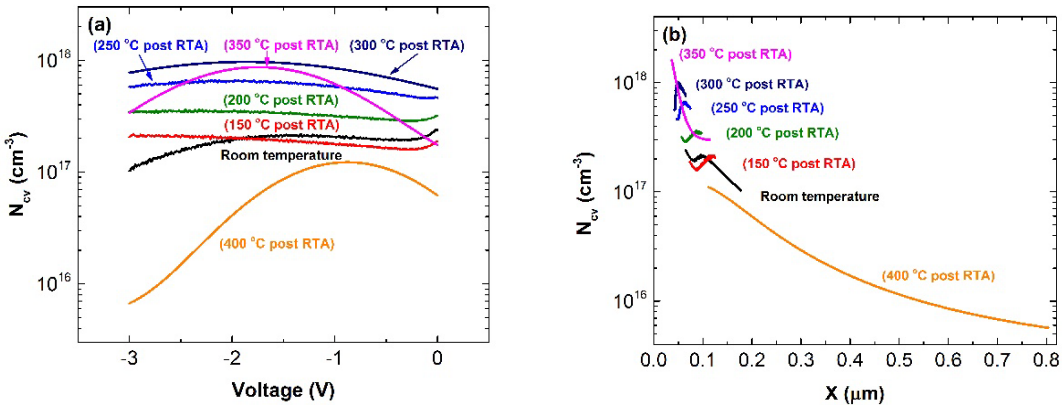


**Figure 6.3 CZTS C-V profile at room temperature and different post RTA temperatures. (a) Carrier concentration vs. voltage profile, (b) carrier concentration vs. depletion depth profile.**

As shown in Figure 6.3 (b), the carrier concentration in these films, as measured by standard C-V, is quite high near the surface. If true, this is the reason for the low values

of $J_{SC}$ (Fig. 6.2 (c)). However, sharply rising profiles for lower post RTA temperature near the surfaces can also be associated with surface states.

The high temperature profiles suggest counter doping diffusion from the CdS. It is observed that carrier concentration curves bend down near zero bias for 300 $^{o}$C, 350 $^{o}$C, and 400 $^{o}$C post RTA (Fig. 6.3 (a)), but others do not. The high temperature behavior may be due to a reduction of the defect-related charge and surface states at CZTS/CdS interface which improves $V_{oc}$ (Fig. 6.2 (b)). However, the recombination velocity depends on both the trap density and the minority carrier concentration. Changes in the carrier concentration profile can lead to band bending that reduce the minority carrier concentration. It is difficult to deconvolute these two effects.

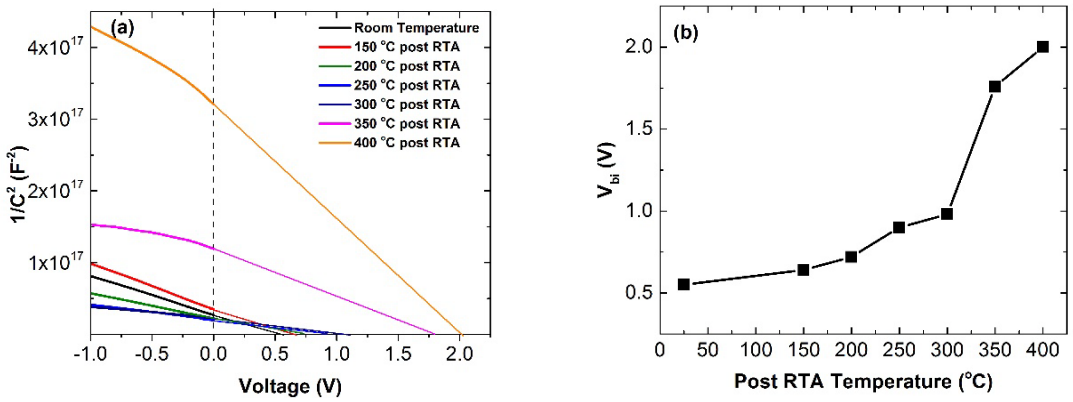


**Figure 6.4 (a) Mott-Schottky plot ($1/C^2$ vs. V profile), (b) built-in voltage ($V_{bi}$) of CZTS thin film solar cell with increasing post RTA temperature.**

Besides doping concentration, CZTS/CdS junction built-in voltage ($V_{bi}$) was also investigated by extrapolating the C-V measurement results. The relationship between

$1/C^2$ and voltage (Mott-Schottky plot) was plotted for CZTS solar cells under various post RTA conditions (Fig. 6.4 (a)), and $V_{bi}$ was derived from the intercept of the plot by

$$\frac{1}{C^2} = \frac{2}{qN_A\varepsilon_s\varepsilon_0 A^2}(V_{bi} - V) \tag{6.1}$$

$$N_A = \frac{2}{q\varepsilon_s\varepsilon_0 A^2\left[\frac{d}{dV}(1/C^2)\right]} \tag{6.2}$$

where $N_A$= doping density ($cm^{-3}$), q = the electron charge ($1.6\times10^{-19}$ C), $\varepsilon_0$ = permittivity of free space ($8.85\times10^{-14}$ F/cm), $\varepsilon_s$ = dielectric constant ($\varepsilon_0$ of CZTS is 7 from first principle calculation [187]), A = area of the cell ($cm^2$), C = measured capacitance, and V = applied DC voltage.

An increasing of $V_{bi}$ was observed with increasing post RTA temperature. This phenomenon is also consistent with the observation of $V_{oc}$ improvement and suggests a depinning of the Fermi level at the surface since counter doping in the absorber should decrease the barrier height. As shown in Figure 6.4 (b), $V_{bi}$ is higher than $V_{oc}$ under high temperature post RTA conditions. This is an artifact and suggests that the simple model of the junction is incorrect. Obviously, post RTA treatments reduce interfacial states and improve the $V_{bi}$ which also benefits $V_{oc}$ and solar cell performance. The measured $V_{bi}$ of solar cells under post RTA at 350 $^oC$ and 400 $^oC$ were unphysically high (Fig. 6.4), and it might be related to the Cd counter doping into CZTS at CZTS/CdS interface with increasing post RTA temperature. The CZTS absorber will be fully depleted along the

grain boundaries and p-n junction be damaged at high temperature (above 400 $^{o}$C), resulting poor solar cell performance.

This is not to say that counter doping is detrimental. This is certainly not the case. It will have a significant impact of carrier collection efficiency. For CZTS thin film solar cell without post RTA treatment, the $V_{bi}$ of the junction is about 0.55 V (Fig. 6.4). The average doping concentration ($N_A$) calculated using the equation (6.2) was $2\times10^{17}$ cm$^{-3}$. With $V_{bi}$ and $N_A$, the depletion width ($W_d$) can be estimated by [63]

$$W_d = (2\varepsilon_s\varepsilon_0 V_{bi}/qN_A)^{1/2} \tag{6.3}$$

A simple calculation gives us an estimation of $W_d$ = 32.6 nm. Meanwhile, carrier diffusion length can be derived by [63]

$$L_n \sim (D_n\tau)^{1/2} = [\mu_n(kT/q)\tau]^{1/2} \tag{6.4}$$

where $\mu_n$ is the electron mobility ($\mu_n$ of CZTS is conservatively assumed as > 5 cm$^2$/Vs [63]), $\tau$ is the minority carrier lifetime ($\tau$ of CZTS is estimated as 8 ns [63]), and $kT/q$ is 28.85 mV at room temperature.

The lower bound of the CZTS carrier diffusion length was estimated, $L_n$ ~ 352.2 nm. The sum of the estimated $W_d$ (~32.6 nm) and the $L_n$ (~ 352.2 nm) is about 384.8 nm. Thus, the total thickness that contribute to the photocurrent is much smaller than the CZTS film thickness (1.5~2 μm). This suggests very poor collection of carriers across the entire

absorber thickness, which might explain the low $J_{sc}$ observed before. Assuming we don't change carrier mobility and minority carrier lifetime, the carrier diffusion length $L_n$ is relatively stable. The only approaches to improve the CZTS solar cell performance are either increase the $V_{oc}$ or decrease surface doping concentration $N_A$. From the previous discussions, post RTA treatment proves to be helpful in both aspects.

In order to test the repeatability of the effects of post RTA, same experiments were carried out on several other CZTS thin film solar cells. Similar results were observed. Solar cell performance increases with increasing post RTA temperature, and reaches a highest point at optimum temperature before going down again. The optimum temperature is either 300 $^{o}$C or 350 $^{o}$C, depending on the unannealed CZTS doping concentration. Figure 6.5 (a) shows a CZTS solar cell reaching the highest performance at 300 $^{o}$C post RTA, and efficiency starts to drop after 350 $^{o}$C anneal.

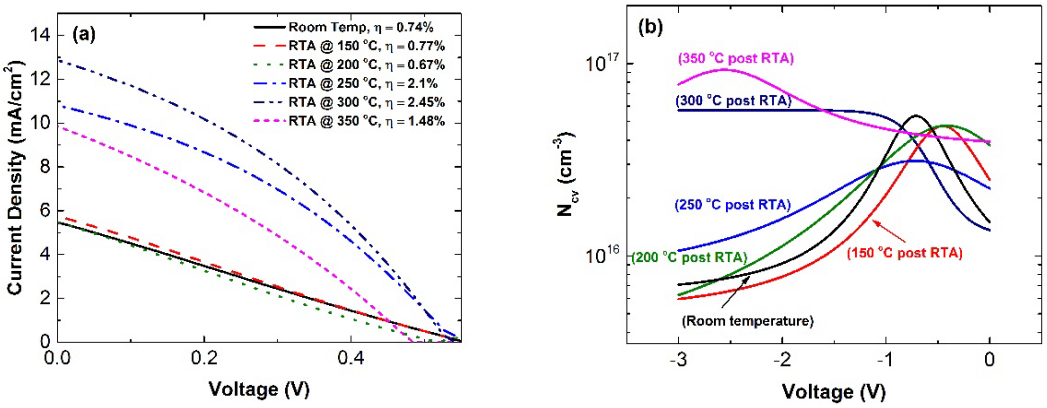


**Figure 6.5 (a) I-V measurement results, and (b) carrier concentration vs. voltage profile of another CZTS solar cell.**

As shown in Figure 6.5 (b), the initial carrier concentration (room temperature profile) of this cell is higher than the device we discussed before. Also, the carrier concentration follows the similar trend and increases with increasing post RTA temperature. The $N_{cv}$ curve bending near zero and -1 volt bias was observed as well. This suggests the repeatability of post RTA effect on enhancing CZTS thin film solar cell performance.

## 6.3 RTA temperature dependence on CZTS thin film properties

### 6.3.1 Experimental Details

Previously, the effect of post RTA on CZTS/CdS junction properties was investigated. In order to make it clear whether other factors also contribute to the improvement of solar cell performance during post RTA, the post RTA temperature dependence on CZTS thin film properties was studied.

CZTS thin films, which were synthesized by sulfurizing the thermally deposited optimum metal precursor stack Cu/Sn/Zn/Cu, were cut into several pieces. One piece was used to form a Schottky junction by depositing Al onto its surface, and then went through post deposition RTA at 150 $^{o}$C, 200 $^{o}$C, 250 $^{o}$C, 300 $^{o}$C, 350 $^{o}$C, respectively. We didn't test 400 $^{o}$C post RTA because of its detrimental effect on junction interface seen in previous experiments. XRD, Raman scattering, SEM/EDS, and CZTS carrier concentration were measured after each anneal. Another piece only went through a 350 $^{o}$C post RTA and then was used to fabricate a thin film solar cell. Post deposition RTA at 150 $^{o}$C, 200 $^{o}$C,

250 $^{o}$C, 300 $^{o}$C, 350 $^{o}$C were carried out on this cell later. I-V and C-V profile were measured after each anneal.

### 6.3.2 Results and Discussions

XRD results of CZTS thin films as-deposited and under various RTA conditions were shown in Figure 6.6. All the peaks are aligned to CZTS and no significant changes were observed with different annealing temperature. However, a blue shift of the main Raman peak was observed with increasing post RTA temperature (Fig. 6.7). For as-deposited thin film without post RTA, Raman main peak was at 337 $cm^{-2}$ which indicated kesterite CZTS. While, the Raman main peak shifted to 332 $cm^{-1}$ after post RTA at 350 $^{o}$C, which was reported to be related to stannite CZTS [154]. As discussed before in Chapter 2, this might be due to the introduction of Cu-Zn disorder during the RTA at higher temperatures.

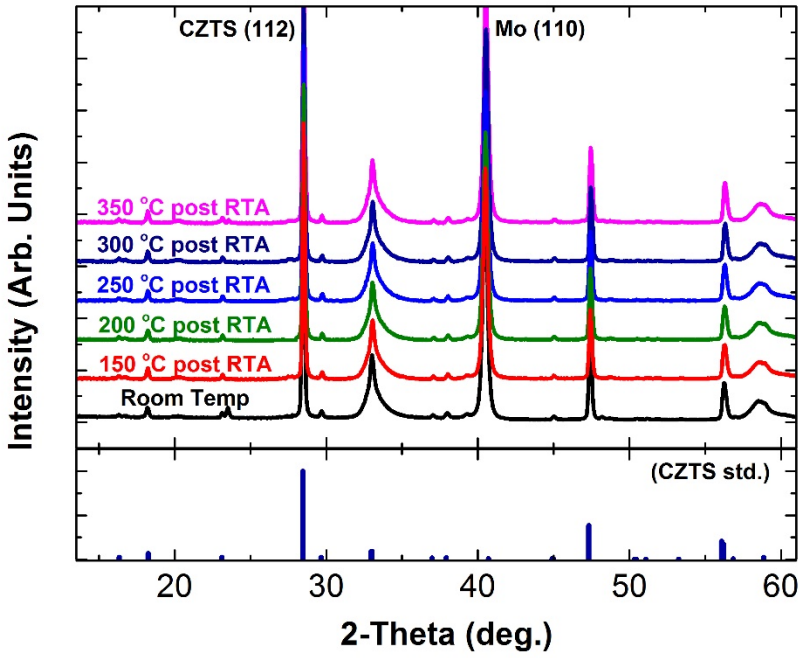


**Figure 6.6 XRD results of CZTS thin film as-deposited and under treatment with increasing post RTA temperature.**

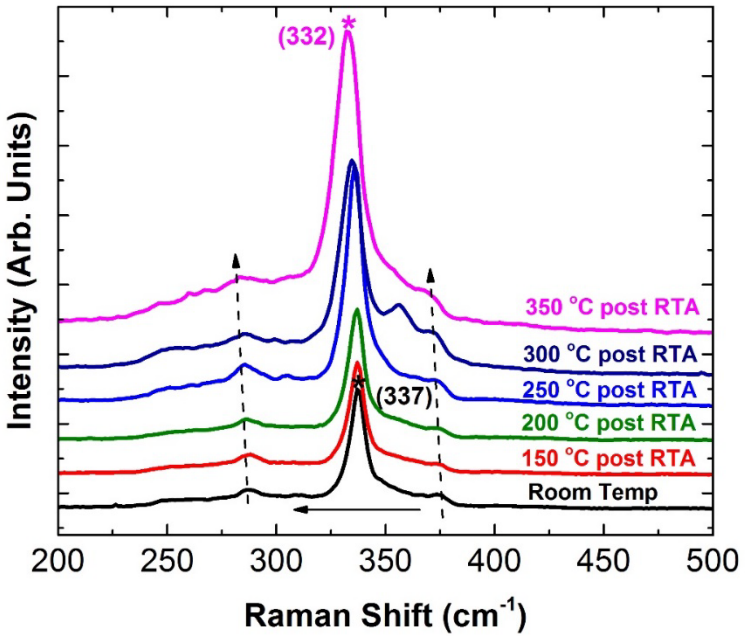


**Figure 6.7 Raman scattering results of CZTS thin film as-deposited and under treatment with increasing post RTA temperature.**

Similarly, C-V measurement was carried out to investigate the effect of RTA on CZTS carrier concentration. Figure 6.8 shows significant and interesting contrasts with the carrier profiles of full devices that have been annealed (Fig. 6.5b). First, the carrier concentrations are generally about an order of magnitude higher in the Schottky device. We do not know the reason for this. Second, the Schottky devices do not show a peak in the carrier profile. This could either indicate a deeper zero-bias depletion width or that the peak in full devices is related to the CdS layer. Cd may be diffusing into the CZTS, counter doping the surface. In CIGS it is believed that the surface of the absorber becomes highly copper deficient as a result of the chemical bath process. The formation

of a copper deficient phase has been observed. This phase is believed to be n-type which could also explain the observed profile.

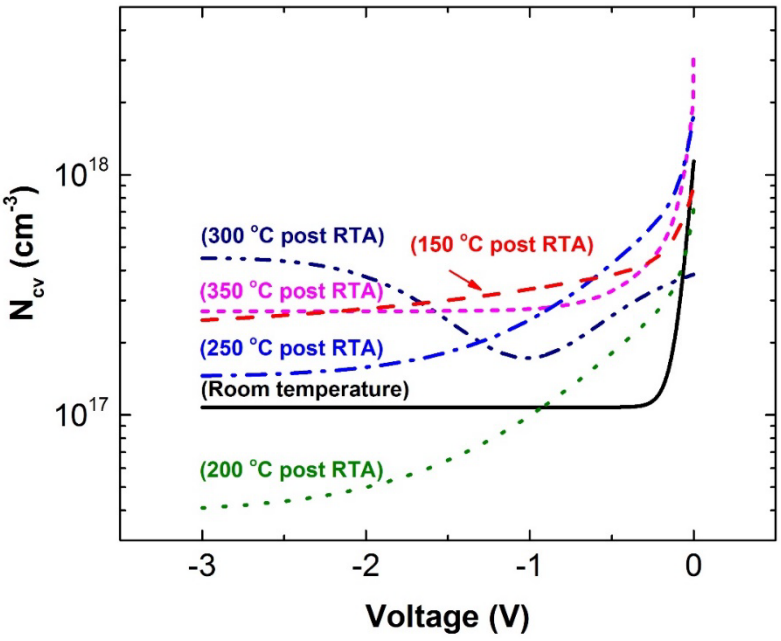


**Figure 6.8 Carrier concentration vs. voltage profiles of CZTS thin film as-deposited and under treatment with increasing post RTA temperature.**

In order to study the effect of Cu-Zn disorder in CZTS absorber on solar cell performance and post RTA, one of the same CZTS pieces was rapid thermal annealed at 350 $^{o}$C for 30 seconds before going through standard solar cell fabrication steps. This cell later was treated with post RTA at 150 $^{o}$C, 200 $^{o}$C, 250 $^{o}$C, 300 $^{o}$C, 350 $^{o}$C.

I-V curve was measured after each anneal, however, the solar cell efficiency improvement was not observed this time (Fig. 6.9). To be specific, the solar cell performance decreased with increasing post RTA temperature, and reached the lowest

efficiency after the 350 $^{o}$C RTA. Details on the changes of CZTS solar cell characteristics with increasing post RTA temperature were shown in Figure 6.10.

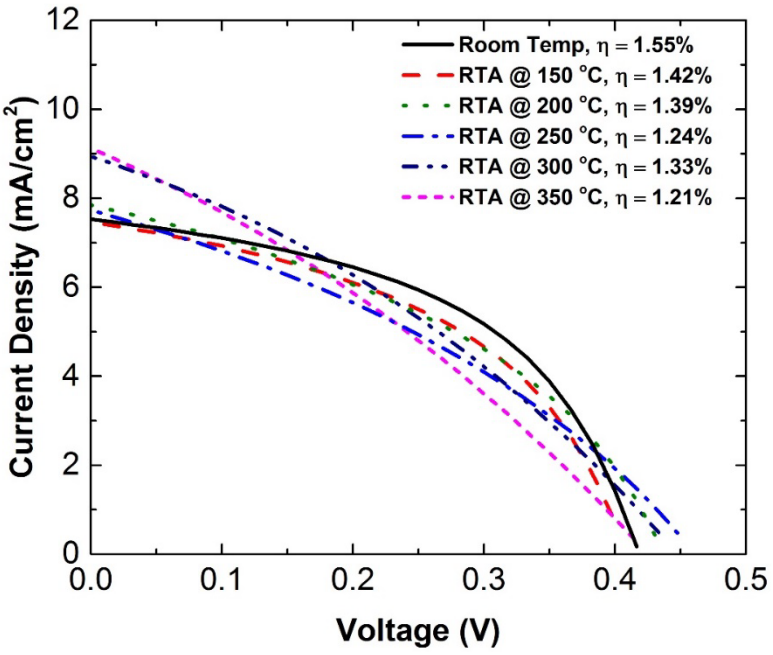


**Figure 6.9 I-V measurement results of CZTS thin film solar cell as-fabricated and under treatment with increasing post RTA temperature.**

$V_{oc}$ first increased with increasing post RTA temperature and reached the maximum value at 250 $^{o}$C before dropping. This is probably due to the aforementioned counter doping of Cd into CZTS, which improves the junction properties and $V_{oc}$. An increase in $J_{sc}$ was observed with increasing post RTA temperature, while conversion efficiency and FF were reduced rapidly. I-V curves can be extrapolated to give information about series resistance ($R_S$) and shunt resistance ($R_{SH}$). The slope of I-V curve at $J_{sc}$ is proportional to

the $R_{SH}$, and the slope at the $V_{oc}$ point is proportional to the $R_S$. The decrease of $R_{SH}$ can explain the drop in FF.

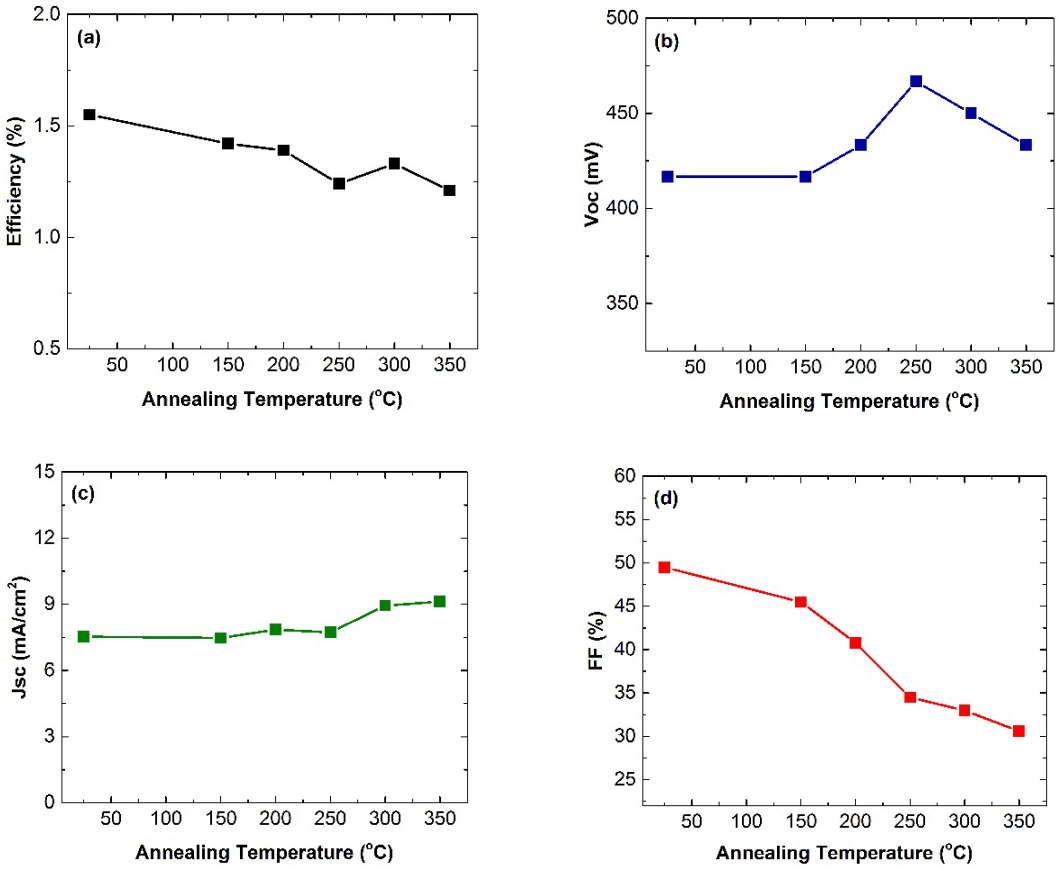


**Figure 6.10 (a) Solar cell conversion efficiency, (b) $V_{oc}$, (c) $J_{sc}$, (d) FF of CZTS thin film solar cell as-fabricated and under treatment with increasing post RTA temperature.**

The carrier concentration ($N_A$) was derived after each RTA treatment by conducting C-V measurements. $N_A$ was found to be an order of magnitude higher for as-fabricated CZTS solar cell without post RTA than the device shown in Figure 6.5. This is probably due to the elimination of trap states that increase the carrier concentration after the 350 °C RTA.

The higher carrier concentration might be also due to the 350 $^{o}$C RTA treatment on CZTS absorber before solar cell fabrication, which led to the introduction of Cu-Zn disorder defects into the film. Since the $Cu_{Zn}$ antisite is the dominant acceptor defect in CZTS, a higher carrier concentration is expected with more Cu-Zn disorder defects and also higher $J_{sc}$.

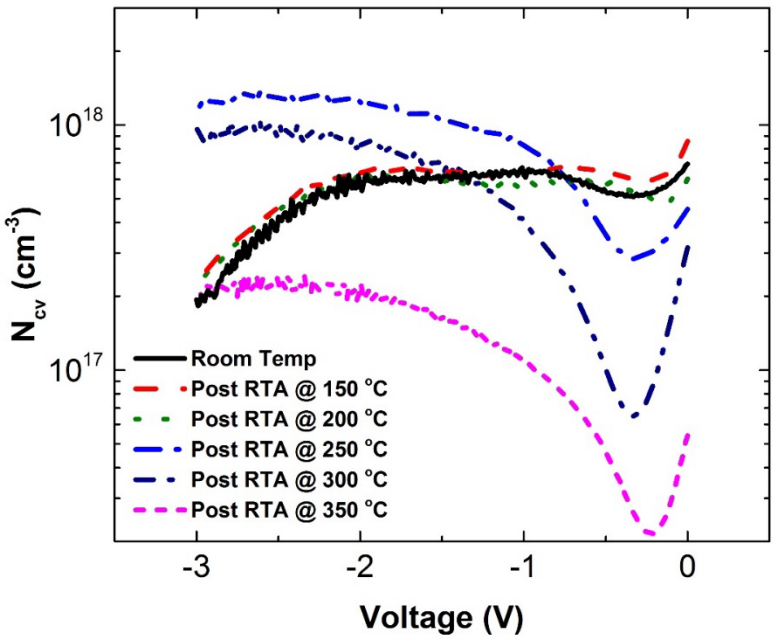


**Figure 6.11 C-V measurement results of CZTS thin film solar cell as-fabricated and under treatment with increasing post RTA temperature.**

The carrier concentration profiles sink near zero voltage, and the curves bend deeper at higher RTA temperatures. This is consistent with the observation in previous experiments, and interfacial doping level decreases because of Cd counter doping during the RTA. However, the bulk carrier concentration of CZTS absorber increases after

higher temperature RTA, which can explain the drop of solar cell performance. The latter may be due to the removal of deep states that traps charge.

## 6.4 Conclusion

A $Cu_2ZnSnS_4$ (CZTS) solar cell with an efficiency of 1.56% at room temperature was fabricated using a film obtained from sulfurization of the metal stack precursor Cu/Sn/Zn/Cu. It is suggested that precursor stacks with Cu on the top provide more uniform CZTS thin films with fewer ZnS secondary phases and then produce higher efficiency solar cells. The effect of post deposition RTA on complete CZTS solar cells was investigated. Solar cell performance first improves with increasing RTA temperature, but then decreases sharply near 400 $^oC$. Through C-V measurement results, we have shown that post RTA of CZTS solar cell affects CZTS/CdS interfacial defect concentration profile and zero bias depletion depth, which means the defect-related charge at CZTS/CdS interface reduces and this improves $V_{oc}$ and the fill factor. The effect of RTA on CZTS absorbers was studied as well. An increase in CZTS carrier concentration was observed. This is probably due to the elimination of trap states during the RTA. It might be also a result of the introduction of Cu-Zn disorder as seen in the increasing Raman blue shift (Fig. 6.7) with increasing RTA temperature. It was reported that the near-resonant Raman was shown to be a convenient tool to track Cu/Zn disorder in CZTS films, allowing determination of the critical temperature for the transition from ordered to disordered kesterite at a relatively low temperature 533 K (260 $^oC$) [188]. This

is the temperature that the carrier concentration changes start to be observed. Further study on detailed solar cell performance improvement mechanism is needed.

# Chapter 7

# 7 Summary and Outlook

## 7.1 Summary

There is a growing interest in replacing $Cu(In_xGa_{1-x})Se_2$ (CIGS) light absorbers with CZTS and enhancing CZTS thin film solar cell conversion efficiency for large-scale manufacturing. This thesis presented the synthesis of $Cu_2ZnSnS_4$ (CZTS) thin films by the post sulfurization of thermally evaporated metal precursor stacks. The research focused on optimizing the growth of CZTS absorbers, and improving the CZTS solar cell performance from material and device level processes.

The effects of sulfurization conditions, substrates, back contact layers, and metal precursor stacking orders on CZTS thin film structural properties and microstructures were investigated. Based on successfully synthesized CZTS thin films with better morphology and less secondary phases and defects, the influence of CZTS chemical composition on film properties and solar cell performance was studied. It was shown that CZTS thin film chemical composition affects the carrier concentration profile, which then influences the device characteristics. Only a small deviation from the optimal chemical composition can drop device performance significantly. This confirms the idea that the CZTS solar cells with high conversion efficiency exist in a relatively narrow composition region.

In addition to the CZTS absorber chemical composition study, a study of the effects of post deposition rapid thermal annealing (RTA) was conducted and its influence on solar cell performance was studied. It is observed that an optimized RTA enhances the device performance. Through C-V measurement results, we have shown that RTA of CZTS solar cell affects the CZTS/CdS interfacial defect concentration and zero bias depletion depth, which means that the defect-related charge at the CZTS/CdS interface is reduced. This increases both $V_{oc}$ and the fill factor. Also, the effects of RTA on CZTS absorber properties were investigated and an increase in CZTS carrier concentration was observed. This is probably due to the elimination of trap states during RTA. It might also be a result of the introduction of Cu-Zn disorder with increasing RTA temperature.

## 7.2 Outlook

Previous experiments show the possibility of growing CZTS on various metal back contact layers. Mo, Cr, Al, and Ti are identified as back contact candidates of interest. However, CZTS films grown on Cr, Al, and Ti have smaller grains compared to films grown on Mo. It is shown in cross-section images that only Mo back contact has a columnar structure, which might be beneficial to Na diffusion into Cu-Zn-Sn precursors and be useful to enhance the grain growth. This might be solved by providing an alternate source of Na as the vapor transport effect discussed in the thesis. However, Cr, Al, and Ti are also found to react with Zn, Sn or Cu in the precursors. This reaction might also slow the CZTS growth process. To further investigate these promising back contacts, optimal

deposition conditions for the metal layer need to be studied. The back contact film thickness, stress, resistance, and the stability of CZTS/metal interface must be investigated as well.

The C-V measurement used here is one of the most widely-used electrical measurement techniques for evaluating Schottky diode or the p-n junction characteristics. The doping concentration near the p-n interface can be extracted from the capacitance profile. However, the technique measures all charge in the space charge region that is capable of following the applied ac signal, typically 100 kHz to 1 MHz. This includes both shallow bulk states and interface states. It is very possible that the increase in the carrier profiles near the CZTS/CdS interface is due to states associated with this interface. A more precise characterization of the CZTS thin film bulk carrier concentration can be obtained through DLCP measurements to supplement the C-V data because DLCP is not sensitive to interface states. To address the effect of RTA on CZTS absorber carrier concentration, DLCP is quite useful and contributes to a more accurate measurement. Also, near-resonant Raman measurement can be used to track the Cu-Zn disorder and will be useful to explain the order-disorder transition in CZTS thin films.

The development of CTZS absorbers and solar cell characterization methods applicable to CZTS PV has attracted much attention; however, a consistent relationship between device performance and material characterization is still being researched. Mostly, linking material characterization to solar cell performance is limited to closely related

samples from a specific lab, using CZTS synthesized by a certain method, or with process variations limited to some certain parameters [56, 178, 186]. This results in a disappointing lack of tools and methods for process feedback and control during large-scale industrial manufacturing. Thus, one of the challenges in this project is to identify measurable properties of CZTS materials or devices that exhibit strong correlation with PV performance irrespective of the processing method used to deposit the absorber layer [169]. This suggests that it would be beneficial to collaborate with other research groups to investigate the effects of post deposition RTA on CZTS thin films and solar cell characteristics made of absorbers synthesized using other approaches, such as sputtering, the sol-gel method, and electrochemical deposition. Further study is needed to address the relationship between device post deposition treatment, CZTS absorber properties, and device performance.

## References


[1] M. A. Green, K. Emery, Y. Hishikawa, W. Warta, and E. D. Dunlop, "Solar cell efficiency tables (Version 45)," *Progress in Photovoltaics*, vol. 23, pp. 1-9, Jan 2015.

[2] R. Wustenhagen, M. Wolsink, and M. J. Burer, "Social acceptance of renewable energy innovation: An introduction to the concept," *Energy Policy*, vol. 35, pp. 2683-2691, May 2007.

[3] I. Dincer, "Renewable energy and sustainable development: a crucial review," *Renewable & Sustainable Energy Reviews*, vol. 4, pp. 157-175, Jun 2000.

[4] H. Flammersberger, "Experimental study of $Cu_2ZnSnS_4$ thin films for solar cells," Ph. D., Department of Engineering Sciences, Uppsala University, 2010.

[5] A. Becquerel, "Recherches sur les effects de la radiation chimique de la lumiere solaire au moyen des courants electriques " *Comptes Rendus de L'Academie des Sciences* vol. 9 pp. 145-149, 1839.

[6] W. Smith, "Effect of light on Selenium during the passage of an electric current " *Nature*, p. 303, 1873.

[7] M. A. Maehlum. The history of solar energy [Online]. Available: http://energyinformative.org/the-history-of-solar-energy-timeline/

[8] A. Einstein, "On a Heuristic Viewpoint Concerning the Production and Transformation of Light," *Annalen der Physik*, vol. 322, p. 132, 1905.

[9] *R. D. Williams*. Sun Fact Sheet [Online]. Available: http://nssdc.gsfc.nasa.gov/planetary/factsheet/sunfact.html

[10] S. G. Smith, "Human color vision and the unsaturated blue color of the daytime sky," *Am. J. Phys.*, vol. 73, 2005.

[11] P. Wurfel, "Physics of Solar Cells: From Principles to New Concepts," *Physics of Solar Cells: from Principles to New Concepts*, pp. 1-186, 2005.

[12] N. R. E. Laboratory. (2010). *Reference Solar Spectral Irradiance: Air Mass 1.5*. Available: http://rredc.nrel.gov/solar/spectra/am1.5/

[13] P. Education. *Standard Solar Spectra*. Available: http://www.pveducation.org/pvcdrom/appendices/standard-solar-spectra

[14] W. Shockley and J. H. Queisser, "Detailed Balance Limit of Efficiency of p‐n Junction Solar Cells," *Journal of Applied Physics*, vol. 32, p. 510, 1961.

[15] C. H. Henry, "LIMITING EFFICIENCIES OF IDEAL SINGLE AND MULTIPLE ENERGY-GAP TERRESTRIAL SOLAR-CELLS," *Journal of Applied Physics*, vol. 51, pp. 4494-4500, 1980 1980.

[16] A. Luque and A. Marti, "Increasing the efficiency of ideal solar cells by photon induced transitions at intermediate levels," *Physical Review Letters*, vol. 78, pp. 5014-5017, Jun 30 1997.

[17] S. J. Fonash, "Solar Cell Device Physics Second Edition Introduction," in *Solar Cell Device Physics, 2nd Edition*, ed San Diego: Elsevier Academic Press Inc, 2010, pp. 1-8.
[18] J. Merten, J. M. Asensi, C. Voz, A. V. Shah, R. Platz, and J. Andreu, "Improved equivalent circuit and analytical model for amorphous silicon solar cells and modules," *Ieee Transactions on Electron Devices,* vol. 45, pp. 423-429, Feb 1998.
[19] C. Ume, J. Gong, R. Ahmad, and A. Valdes, "Laser Ultrasonic Inspection of Solder Bumps in Flip-Chip Packages Using Virtual Chip Package as Reference," *Ieee Transactions on Components Packaging and Manufacturing Technology,* vol. 1, pp. 1739-1746, Nov 2011.
[20] J. Gong, P. Vukkadala, J. K. Sinha, and K. T. Turner, "Determining local residual stresses from high resolution wafer geometry measurements," *Journal of Vacuum Science & Technology B,* vol. 31, Sep 2013.
[21] J. Gong, S. Sood, R. Bhat, S. Jahanbin, P. Aji, T. Uhrmann, *et al.*, "Wafer edge defect study of temporary bonded and thin wafers in TSV process flow," presented at the Electronic Components and Technology Conference (ECTC), San Diego, CA, 2015.
[22] A. L. Endros, "Mono- and tri-crystalline Si for PV application," *Solar Energy Materials and Solar Cells,* vol. 72, pp. 109-124, Apr 2002.
[23] B. Li, L. D. Wang, B. N. Kang, P. Wang, and Y. Qiu, "Review of recent progress in solid-state dye-sensitized solar cells," *Solar Energy Materials and Solar Cells,* vol. 90, pp. 549-573, Mar 23 2006.
[24] B. Oregan and M. Gratzel, "A LOW-COST, HIGH-EFFICIENCY SOLAR-CELL BASED ON DYE-SENSITIZED COLLOIDAL TIO2 FILMS," *Nature,* vol. 353, pp. 737-740, Oct 1991.
[25] A. Jena, S. P. Mohanty, P. Kumar, J. Naduvath, V. Gondane, P. Lekha, *et al.*, "Dye Sensitized Solar Cells: A Review," *Transactions of the Indian Ceramic Society,* vol. 71, pp. 1-16, Jan-Mar 2012.
[26] M. R. Narayan, "Review: Dye sensitized solar cells based on natural photosensitizers," *Renewable & Sustainable Energy Reviews,* vol. 16, pp. 208-215, Jan 2012.
[27] H. Spanggaard and F. C. Krebs, "A brief history of the development of organic and polymeric photovoltaics," *Solar Energy Materials and Solar Cells,* vol. 83, pp. 125-146, Jun 15 2004.
[28] H. Yanagi, N. Tamura, S. Taira, H. Furuta, S. Douko, G. Schnurpfeil, *et al.*, "An optimal design for photovoltaic properties of two-layer organic solar cells using phthalocyanine and perylene derivatives," *Molecular Crystals and Liquid Crystals Science and Technology Section a-Molecular Crystals and Liquid Crystals,* vol. 267, pp. 435-440, 1995 1995.
[29] H. Hoppe and N. S. Sariciftci, "Organic solar cells: An overview," *Journal of Materials Research,* vol. 19, pp. 1924-1945, Jul 2004.

[30] M. A. Green, "Thin-film solar cells: review of materials, technologies and commercial status," *Journal of Materials Science-Materials in Electronics*, vol. 18, pp. S15-S19, Oct 2007.
[31] K. L. Chopra, P. D. Paulson, and V. Dutta, "Thin-film solar cells: An overview," *Progress in Photovoltaics*, vol. 12, pp. 69-92, Mar-May 2004.
[32] W. Hermes, D. Waldmann, M. Agari, K. Schierle-Arndt, and P. Erk, "Emerging Thin-Film Photovoltaic Technologies," *Chemie Ingenieur Technik*, vol. 87, pp. 376-389, Apr 2015.
[33] Z. Fang, X. C. Wang, H. C. Wu, and C. Z. Zhao, "Achievements and Challenges of CdS/CdTe Solar Cells," *International Journal of Photoenergy*, 2011.
[34] A. Bosio, N. Romeo, S. Mazzamuto, and V. Canevari, "Polycrystalline CdTe thin films for photovoltaic applications," *Progress in Crystal Growth and Characterization of Materials*, vol. 52, pp. 247-279, 2006.
[35] (2015). *CdTe Technology*. Available: http://www.firstsolar.com/en/technologies-and-capabilities/pv-modules/first-solar-series-3-black-module/cdte-technology
[36] B. M. Basola and B. McCandless, "Brief review of cadmium telluride-based photovoltaic technologies," *Journal of Photonics for Energy*, vol. 4, Jun 2014.
[37] J. A. Thornton, D. G. Cornog, R. B. Hall, S. P. Shea, and J. D. Meakin, "REACTIVE SPUTTERED COPPER INDIUM DISELENIDE FILMS FOR PHOTOVOLTAIC APPLICATIONS," *Journal of Vacuum Science & Technology a-Vacuum Surfaces and Films*, vol. 2, pp. 307-311, 1984.
[38] J. A. del Cueto, S. Rummel, B. Kroposki, C. Osterwald, A. Anderberg, and Ieee, "STABILITY OF CIS/CIGS MODULES AT THE OUTDOOR TEST FACILITY OVER TWO DECADES," in *33rd IEEE Photovoltaic Specialists Conference*, San Diego, CA, 2008, pp. 1707-1712.
[39] (2015). *Miasole flexible solar cell*. Available: http://miasole.com/en/miasole-advantages/flexible-solar-cell/
[40] P. S. Vasekar and T. P. Dhakal, "Thin Film Solar Cells using Earth-Abundant Materials " in *Thin Film Solar Cells From Earth Abundant Materials*, ed, 2013.
[41] B. Yang, L. Wang, J. Han, Y. Zhou, H. Song, S. Chen, *et al.*, "CuSbS2 as a Promising Earth-Abundant Photovoltaic Absorber Material: A Combined Theoretical and Experimental Study," *Chemistry of Materials*, vol. 26, pp. 3135-3143, May 27 2014.
[42] T. Kato, H. Hiroi, N. Sakai, S. Muraoka, and H. Sugimoto, "Characterization of Front and Back Interfaces on $Cu_2ZnSnS_4$ Thin-Film Cells " presented at the 27th European Photovoltaic Solar Energy Conference and Exhibition Frankfurt, Germany, 2012.
[43] Y. S. Lee, M. Bertoni, M. K. Chan, G. Ceder, T. Buonassisi, and Ieee, "EARTH ABUNDANT MATERIALS FOR HIGH EFFICIENCY HETEROJUNCTION THIN FILM SOLAR CELLS," in *34th IEEE Photovoltaic Specialists Conference*, Philadelphia, PA, 2009, pp. 1247-1249.

[44] G. M. Kimball, A. M. Muller, N. S. Lewis, and H. A. Atwater, "Photoluminescence-based measurements of the energy gap and diffusion length of Zn3P2," *Applied Physics Letters*, vol. 95, Sep 2009.
[45] E. A. Fagen, "OPTICAL-PROPERTIES OF ZN3P2," *Journal of Applied Physics*, vol. 50, pp. 6505-6515, 1979.
[46] M. Bhushan and A. Catalano, "POLYCRYSTALLINE ZN3P2 SCHOTTKY-BARRIER SOLAR-CELLS," *Applied Physics Letters*, vol. 38, pp. 39-41, 1981.
[47] K. W. Mitchell, "STATUS OF NEW THIN-FILM PHOTO-VOLTAIC TECHNOLOGIES," *Annual Review of Materials Science*, vol. 12, pp. 401-415, 1982.
[48] W. A. Welch, Baranowski, L. Lauryn,Zawadzki, Pawel,DeHart, Clay,Johnston, SteveLany, Stephan, Wolden, A. Colin,Zakutayev, Andriy, "Accelerated development of CuSbS2 thin film photovoltaic device prototypes," *arXiv Preprint*, p. arXiv:1504.01345., 2015.
[49] M. A. Green, A. Ho-Baillie, and H. J. Snaith, "The emergence of perovskite solar cells," *Nature Photonics*, vol. 8, pp. 506-514, Jul 2014.
[50] N.-G. Park, "Perovskite solar cells: an emerging photovoltaic technology," *Materials Today*, vol. 18, pp. 65-72, Mar 2015.
[51] A. Kojima, K. Teshima, Y. Shirai, and T. Miyasaka, "Organometal Halide Perovskites as Visible-Light Sensitizers for Photovoltaic Cells," *Journal of the American Chemical Society*, vol. 131, pp. 6050-+, May 2009.
[52] J. H. Im, C. R. Lee, J. W. Lee, S. W. Park, and N. G. Park, "6.5% efficient perovskite quantum-dot-sensitized solar cell," *Nanoscale*, vol. 3, pp. 4088-4093, 2011.
[53] G. Niu, X. Guo, and L. Wang, "Review of recent progress in chemical stability of perovskite solar cells," *Journal of Materials Chemistry A*, vol. 3, pp. 8970-8980, 2015 2015.
[54] T. Shibata, Y. Muranushi, T. Miura, and T. Kishi, "PHOTOCONDUCTIVE PROPERTIES OF SINGLE-CRYSTAL 2H-SNS2," *Journal of Physics and Chemistry of Solids*, vol. 51, pp. 1297-1300, 1990.
[55] A. Szczerbakow, M. Godlewski, E. Dynowska, V. Y. Ivanov, K. Swiatek, E. M. Goldys, *et al.*, "Structure, surface morphology and optical properties of thin films of ZnS and CdS grown by atomic layer epitaxy," *Acta Physica Polonica A*, vol. 94, pp. 579-582, Sep 1998.
[56] H. Katagiri, K. Saitoh, T. Washio, H. Shinohara, T. Kurumadani, and S. Miyajima, "Development of thin film solar cell based on Cu2ZnSnS4 thin films," *Solar Energy Materials and Solar Cells*, vol. 65, pp. 141-148, Jan 2001.
[57] X. G. Wanga, S. S. Li, W. K. Kim, S. Yoon, V. Craciun, J. M. Howard, *et al.*, "Investigation of rapid thermal annealing on Cu(In,Ga)Se-2 films and solar cells," *Solar Energy Materials and Solar Cells*, vol. 90, pp. 2855-2866, Nov 2006.

[58] M. Izadifard, I. A. Buyanova, J. P. Bergman, W. M. Chen, A. Utsumi, Y. Furukawa, *et al.*, "Effects of rapid thermal annealing on optical properties of GaNxP1-x alloys grown by solid source molecular beam epitaxy," *Semiconductor Science and Technology,* vol. 20, pp. 353-356, May 2005.
[59] H. Miyazaki, R. Mikami, A. Yamada, and M. Konagai, "Cu(InGa)Se-2 thin film absorber with high Ga contents and its application to the solar cells," *Journal of Physics and Chemistry of Solids,* vol. 64, pp. 2055-2058, Sep-Oct 2003.
[60] X. B. Song, X. Ji, M. Li, W. D. Lin, X. Luo, and H. Zhang, "A Review on Development Prospect of CZTS Based Thin Film Solar Cells," *International Journal of Photoenergy,* p. 11, 2014.
[61] J. J. Scragg, P. J. Dale, L. M. Peter, G. Zoppi, and I. Forbes, "New routes to sustainable photovoltaics: evaluation of Cu2ZnSnS4 as an alternative absorber material," *Physica Status Solidi B-Basic Solid State Physics,* vol. 245, pp. 1772-1778, Sep 2008.
[62] H. Katagiri, N. Sasaguchi, S. Hando, S. Hoshino, J. Ohashi, and T. Yokota, "Preparation and evaluation of Cu2ZnSnS4 thin films by sulfurization of E-B evaporated precursors," *Solar Energy Materials and Solar Cells,* vol. 49, pp. 407-414, Dec 1997.
[63] B. Shin, O. Gunawan, Y. Zhu, N. A. Bojarczuk, S. J. Chey, and S. Guha, "Thin film solar cell with 8.4% power conversion efficiency using an earth-abundant Cu2ZnSnS4 absorber," *Progress in Photovoltaics,* vol. 21, pp. 72-76, Jan 2013.
[64] R. H. Zhang, S. M. Szczepaniak, N. J. Carter, C. A. Handwerker, and R. Agrawal, "A Versatile Solution Route to Efficient Cu2ZnSn(S,Se)(4) Thin-Film Solar Cells," *Chemistry of Materials,* vol. 27, pp. 2114-2120, Mar 2015.
[65] W. Wang, M. T. Winkler, O. Gunawan, T. Gokmen, T. K. Todorov, Y. Zhu, *et al.*, "Device Characteristics of CZTSSe Thin-Film Solar Cells with 12.6% Efficiency," *Advanced Energy Materials,* vol. 4, May 2014.
[66] S. A. Kissin, "A REINVESTIGATION OF THE STANNITE (CU2FESNS4) - KESTERITE (CU2ZNSNS4) PSEUDOBINARY SYSTEM," *Canadian Mineralogist,* vol. 27, pp. 689-697, Dec 1989.
[67] S. Siebentritt and S. Schorr, "Kesterites - a challenging material for solar cells," *Progress in Photovoltaics,* vol. 20, pp. 512-519, Aug 2012.
[68] S. Y. Chen, X. G. Gong, A. Walsh, and S. H. Wei, "Crystal and electronic band structure of Cu2ZnSnX4 (X=S and Se) photovoltaic absorbers: First-principles insights," *Applied Physics Letters,* vol. 94, Jan 2009.
[69] S. Schorr, "The crystal structure of kesterite type compounds: A neutron and X-ray diffraction study," *Solar Energy Materials and Solar Cells,* vol. 95, pp. 1482-1488, Jun 2011.
[70] S. B. Zhang, S. H. Wei, A. Zunger, and H. Katayama-Yoshida, "Defect physics of the CuInSe2 chalcopyrite semiconductor," *Physical Review B,* vol. 57, pp. 9642-9656, Apr 1998.

[71] S. H. Wei and S. B. Zhang, "Defect properties of CuInSe2 and CuGaSe2," *Journal of Physics and Chemistry of Solids,* vol. 66, pp. 1994-1999, Nov 2005.
[72] S. H. Wei, S. B. Zhang, and A. Zunger, "Effects of Ga addition to CuInSe2 on its electronic, structural, and defect properties," *Applied Physics Letters,* vol. 72, pp. 3199-3201, Jun 1998.
[73] S. Y. Chen, J. H. Yang, X. G. Gong, A. Walsh, and S. H. Wei, "Intrinsic point defects and complexes in the quaternary kesterite semiconductor Cu2ZnSnS4," *Physical Review B,* vol. 81, Jun 2010.
[74] S. Y. Chen, X. G. Gong, A. Walsh, and S. H. Wei, "Defect physics of the kesterite thin-film solar cell absorber Cu2ZnSnS4," *Applied Physics Letters,* vol. 96, Jan 2010.
[75] K. Ito and T. Nakazawa, "ELECTRICAL AND OPTICAL-PROPERTIES OF STANNITE-TYPE QUATERNARY SEMICONDUCTOR THIN-FILMS," *Japanese Journal of Applied Physics Part 1-Regular Papers Short Notes & Review Papers,* vol. 27, pp. 2094-2097, Nov 1988.
[76] G. Larramona, S. Bourdais, A. Jacob, C. Chone, T. Muto, Y. Cuccaro, *et al.*, "8.6% Efficient CZTSSe Solar Cells Sprayed from Water-Ethanol CZTS Colloidal Solutions," *Journal of Physical Chemistry Letters,* vol. 5, pp. 3763-3767, Nov 2014.
[77] R. Touati, M. Ben Rabeh, and M. Kanzari, "Effect of post-sulfurization on the structural and optical properties of Cu2ZnSnS4 thin films deposited by vacuum evaporation method," *Thin Solid Films,* vol. 582, pp. 198-202, May 2015.
[78] P. A. Fernandes, P. M. P. Salome, and A. F. da Cunha, "Precursors' order effect on the properties of sulfurized Cu2ZnSnS4 thin films," *Semiconductor Science and Technology,* vol. 24, p. 7, Oct 2009.
[79] M. Z. Ansari and N. Khare, "Structural and optical properties of CZTS thin films deposited by ultrasonically assisted chemical vapour deposition," *Journal of Physics D-Applied Physics,* vol. 47, May 2014.
[80] G. Y. Kim, W. Jo, K. D. Lee, H. S. Choi, J. Y. Kim, H. Y. Shin, *et al.*, "Optical and surface probe investigation of secondary phases in Cu2ZnSnS4 films grown by electrochemical deposition," *Solar Energy Materials and Solar Cells,* vol. 139, pp. 10-18, Aug 2015.
[81] Q. M. Chen, S. Y. Cheng, S. L. Zhuang, and X. M. Dou, "Cu2ZnSnS4 solar cell prepared entirely by non-vacuum processes," *Thin Solid Films,* vol. 520, pp. 6256-6261, Jul 2012.
[82] Y. Wang, Y. H. Huang, A. Y. S. Lee, C. F. Wang, and H. Gong, "Influence of sintering temperature on screen printed Cu2ZnSnS4 (CZTS) films," *Journal of Alloys and Compounds,* vol. 539, pp. 237-241, Oct 2012.
[83] B. Long, S. Y. Cheng, Y. F. Lai, H. F. Zhou, J. L. Yu, and Q. Zheng, "Effects of sulfurization temperature on phases and opto-electrical properties of Cu2ZnSnS4

films prepared by sol-gel deposition," *Thin Solid Films,* vol. 573, pp. 117-121, Dec 2014.
[84] P. A. Fernandes, P. M. P. Salome, and A. F. da Cunha, "Growth and Raman scattering characterization of Cu2ZnSnS4 thin films," *Thin Solid Films,* vol. 517, pp. 2519-2523, Feb 2009.
[85] J. S. Seol, S. Y. Lee, J. C. Lee, H. D. Nam, and K. H. Kim, "Electrical and optical properties of Cu2ZnSnS4 thin films prepared by rf magnetron sputtering process," *Solar Energy Materials and Solar Cells,* vol. 75, pp. 155-162, Jan 2003.
[86] T. Tanaka, T. Nagatomo, D. Kawasaki, M. Nishio, Q. X. Guo, A. Wakahara, *et al.*, "Preparation of Cu2ZnSnS4 thin films by hybrid sputtering," *Journal of Physics and Chemistry of Solids,* vol. 66, pp. 1978-1981, Nov 2005.
[87] K. Jimbo, R. Kimura, T. Kamimura, S. Yamada, W. S. Maw, H. Araki, *et al.*, "Cu2ZnSnS4-type thin film solar cells using abundant materials," *Thin Solid Films,* vol. 515, pp. 5997-5999, May 31 2007.
[88] H. Katagiri, K. Jimbo, W. S. Maw, K. Oishi, M. Yamazaki, H. Araki, *et al.*, "Development of CZTS-based thin film solar cells," *Thin Solid Films,* vol. 517, pp. 2455-2460, Feb 2009.
[89] N. Momose, M. T. Htay, T. Yudasaka, S. Igarashi, T. Seki, S. Iwano, *et al.*, "Cu2ZnSnS4 Thin Film Solar Cells Utilizing Sulfurization of Metallic Precursor Prepared by Simultaneous Sputtering of Metal Targets," *Japanese Journal of Applied Physics,* vol. 50, Jan 2011.
[90] R. Nakamura, K. Tanaka, H. Uchiki, K. Jimbo, T. Washio, and H. Katagiri, "Cu2ZnSnS4 thin film deposited by sputtering with Cu2ZnSnS4 compound target," *Japanese Journal of Applied Physics,* vol. 53, Feb 2014.
[91] R. Bodeux, F. Mollica, and S. Delbos, "Growth of Cu2ZnSnSe4 by cosputtering and reactive annealing atmosphere," *Solar Energy Materials and Solar Cells,* vol. 132, pp. 67-73, Jan 2015.
[92] H. Araki, A. Mikaduki, Y. Kubo, T. Sato, K. Jimbo, W. S. Maw, *et al.*, "Preparation of Cu2ZnSnS4 thin films by sulfurization of stacked metallic layers," *Thin Solid Films,* vol. 517, pp. 1457-1460, Dec 2008.
[93] T. Kobayashi, K. Jimbo, K. Tsuchida, S. Shinoda, T. Oyanagi, and H. Katagiri, "Investigation of Cu2ZnSnS4-based thin film solar cells using abundant materials," *Japanese Journal of Applied Physics Part 1-Regular Papers Brief Communications & Review Papers,* vol. 44, pp. 783-787, Jan 2005.
[94] H. Yoo and J. Kim, "Growth of Cu2ZnSnS4 thin films using sulfurization of stacked metallic films," *Thin Solid Films,* vol. 518, pp. 6567-6572, Sep 2010.
[95] K. J. Wang, B. Shin, K. B. Reuter, T. Todorov, D. B. Mitzi, and S. Guha, "Structural and elemental characterization of high efficiency Cu2ZnSnS4 solar cells," *Applied Physics Letters,* vol. 98, Jan 2011.

[96] B.-A. Schubert, B. Marsen, S. Cinque, T. Unold, R. Klenk, S. Schorr, *et al.*, "Cu2ZnSnS4 thin film solar cells by fast coevaporation," *Progress in Photovoltaics,* vol. 19, pp. 93-96, Jan 2011.
[97] T. Tanaka, D. Kawasaki, M. Nishio, Q. Gu, and H. Ogawal, "Fabrication of Cu2ZnSnS4 thin films by co-evaporation," *Physica Status Solidi C - Current Topics in Solid State Physics, Vol 3, No 8,* vol. 3, pp. 2844-2847, 2006 2006.
[98] N. Kamoun, H. Bouzouita, and B. Rezig, "Fabrication and characterization of Cu2ZnSnS4 thin films deposited by spray pyrolysis technique," *Thin Solid Films,* vol. 515, pp. 5949-5952, May 2007.
[99] F. Jiang, S. Ikeda, T. Harada, and M. Matsumura, "Pure Sulfide Cu2ZnSnS4 Thin Film Solar Cells Fabricated by Preheating an Electrodeposited Metallic Stack," *Advanced Energy Materials,* vol. 4, p. 4, May 2014.
[100] S. Ahmed, K. B. Reuter, O. Gunawan, L. Guo, L. T. Romankiw, and H. Deligianni, "A High Efficiency Electrodeposited Cu2ZnSnS4 Solar Cell," *Advanced Energy Materials,* vol. 2, pp. 253-259, Feb 2012.
[101] A. A. Hendi, "Electrical and Optical Properties of Cu2ZnSnS4 Thin Film Prepared by Sol Gel Method without Sulfurization," *Journal of Nanoelectronics and Optoelectronics,* vol. 9, pp. 718-720, Oct 2014.
[102] K. Tanaka, M. Oonuki, N. Moritake, and H. Uchiki, "Cu2ZnSnS4 thin film solar cells prepared by non-vacuum processing," *Solar Energy Materials and Solar Cells,* vol. 93, pp. 583-587, May 2009.
[103] Y. Miyamoto, K. Tanaka, M. Oonuki, N. Moritake, and H. Uchiki, "Optical properties of Cu2ZnSnS4 thin films prepared by sol-gel and sulfurization method," *Japanese Journal of Applied Physics,* vol. 47, pp. 596-597, Jan 2008.
[104] K. Tanaka, Y. Fukui, N. Moritake, and H. Uchiki, "Chemical composition dependence of morphological and optical properties of Cu2ZnSnS4 thin films deposited by sol-gel sulfurization and Cu2ZnSnS4 thin film solar cell efficiency," *Solar Energy Materials and Solar Cells,* vol. 95, pp. 838-842, Mar 2011.
[105] T. K. Todorov, K. B. Reuter, and D. B. Mitzi, "High-Efficiency Solar Cell with Earth-Abundant Liquid-Processed Absorber," *Advanced Materials,* vol. 22, pp. E156-+, May 25 2010.
[106] F. Kessler and D. Rudmann, "Technological aspects of flexible CIGS solar cells and modules," *Solar Energy,* vol. 77, pp. 685-695, 2004.
[107] A. Hultqvist, P. M. P. Salome, V. Fjallstrom, M. Edoff, B. Aitken, K. Zhang, *et al.*, "Performance of Cu(In,Ga)Se-2 solar cells using nominally alkali free glass substrates with varying coefficient of thermal expansion," *Journal of Applied Physics,* vol. 114, Sep 2013.
[108] J. S. Chen, E. Kolawa, C. M. Garland, M. A. Nicolet, and R. P. Ruiz, "MICROSTRUCTURE OF POLYCRYSTALLINE CUINSE2/CD(ZN)S HETEROJUNCTION SOLAR-CELLS," *Thin Solid Films,* vol. 219, pp. 183-192, Oct 1992.

[109] M. Johnson, S. V. Baryshev, E. Thimsen, M. Manno, X. Zhang, I. V. Veryovkin, *et al.*, "Alkali-metal-enhanced grain growth in Cu2ZnSnS4 thin films," *Energy & Environmental Science,* vol. 7, pp. 1931-1938, Jun 2014.
[110] K. Moriwaki, M. Nomoto, S. Ishizuka, A. Mukai, K. Sato, H. Kobayashi, *et al.*, "Effects of alkali-metal block layer to enhance Na diffusion into Cu(in,Ga)Se-2 absorber on flexible solar cells," *Solar Energy Materials and Solar Cells,* vol. 133, pp. 21-25, Feb 2015.
[111] T. Nakada, D. Iga, H. Ohbo, and A. Kunioka, "Effects of sodium on Cu(In, Ga)Se-2-Based thin films and solar cells," *Japanese Journal of Applied Physics Part 1-Regular Papers Short Notes & Review Papers,* vol. 36, pp. 732-737, Feb 1997.
[112] M. Lee, S. M. Lee, S. Jung, S. Ahn, J. S. Cho, J. Park, *et al.*, "Highly efficient flexible CuIn0.7Ga0.3Se2 solar cells with a thick Na/Mo layer deposited directly on stainless steel," *Applied Surface Science,* vol. 346, pp. 562-566, Aug 2015.
[113] S. M. Pawar, A. I. Inamdar, B. S. Pawar, K. V. Gurav, S. W. Shin, X. Yanjun, *et al.*, "Synthesis of Cu2ZnSnS4 (CZTS) absorber by rapid thermal processing (RTP) sulfurization of stacked metallic precursor films for solar cell applications," *Materials Letters,* vol. 118, pp. 76-79, Mar 2014.
[114] J. J. Scragg, T. Kubart, J. T. Watjen, T. Ericson, M. K. Linnarsson, and C. Platzer-Bjorkman, "Effects of Back Contact Instability on Cu2ZnSnS4 Devices and Processes," *Chemistry of Materials,* vol. 25, pp. 3162-3171, Aug 2013.
[115] I. Kaur, D. K. Pandya, and K. L. Chopra, "GROWTH-KINETICS AND POLYMORPHISM OF CHEMICALLY DEPOSITED CDS FILMS," *Journal of the Electrochemical Society,* vol. 127, pp. 943-948, 1980.
[116] J. Herrero, M. T. Gutierrez, C. Guillen, J. M. Dona, M. A. Martinez, A. M. Chaparro, *et al.*, "Photovoltaic windows by chemical bath deposition," *Thin Solid Films,* vol. 361, pp. 28-33, Feb 2000.
[117] S. Abd-Lefdil, C. Messaoudi, M. Abd-Lefdil, and D. Sayah, "Temperature growth and annealing effects on CdS thin films prepared by chemical bath deposition process," *Physica Status Solidi a-Applied Research,* vol. 168, pp. 417-423, Aug 1998.
[118] J. N. Ximello-Quiebras, G. Contreras-Puente, J. Aguilar-Hernandez, G. Sanatana-Rodriguez, and A. A. C. Readigos, "Physical properties of chemical bath deposited CdS thin films," *Solar Energy Materials and Solar Cells,* vol. 82, pp. 263-268, May 2004.
[119] J. Kim, C. Park, S. M. Pawar, A. I. Inamdar, Y. Jo, J. Han, *et al.*, "Optimization of sputtered ZnS buffer for Cu2ZnSnS4 thin film solar cells," *Thin Solid Films,* vol. 566, pp. 88-92, Sep 1 2014.
[120] R. N. Bhattacharya, M. A. Contreras, B. Egaas, R. N. Noufi, A. Kanevce, and J. R. Sites, "High efficiency thin-film CuIn1-xGaxSe2 photovoltaic cells using a Cd1-xZnxS buffer layer," *Applied Physics Letters,* vol. 89, p. 2, Dec 2006.

[121] K. M. McPeak, B. Opasanont, T. Shibata, D. K. Ko, M. A. Becker, S. Chattopadhyay, *et al.*, "Microreactor Chemical Bath Deposition of Laterally Graded Cd1-xZnxS Thin Films: A Route to High-Throughput Optimization for Photovoltaic Buffer Layers," *Chemistry of Materials*, vol. 25, pp. 297-306, Feb 2013.
[122] T. W. Zhang, C. J. Zhu, C. Z. Wang, and J. Li, "Preparation and characterization of Cd1-x Zn (x) S buffer layers for thin film solar cells," *Rare Metals*, vol. 32, pp. 47-51, Feb 2013.
[123] T. Yagioka and T. Nakada, "Cd-Free Flexible Cu(In,Ga)Se-2 Thin Film Solar Cells with ZnS(O,OH) Buffer Layers on Ti Foils," *Applied Physics Express*, vol. 2, Jul 2009.
[124] J. H. Tao, K. Z. Zhang, C. J. Zhang, L. L. Chen, H. Y. Cao, J. F. Liu, *et al.*, "A sputtered CdS buffer layer for co-electrodeposited Cu2ZnSnS4 solar cells with 6.6% efficiency," *Chemical Communications*, vol. 51, pp. 10337-10340, 2015.
[125] D. Hironiwa, N. Matsuo, N. Sakai, T. Katou, H. Sugimoto, J. Chantana, *et al.*, "Sputtered (Zn,Mg)O buffer layer for band offset control in Cu2ZnSn(S,Se)(4) solar cells," *Japanese Journal of Applied Physics*, vol. 53, p. 6, Oct 2014.
[126] N. Sakai, H. Hiroi, and H. Sugimoto, "Development of Cd-free buffer layer for Cu2ZnSnS4 thin film solar cells," in *Photovoltaic Specialists Conference (PVSC), 2011 37th IEEE*, Seattle, WA, 2011, pp. 003654-003657.
[127] K. Orgassa, H. W. Schock, and J. H. Werner, "Alternative back contact materials for thin film Cu(In,Ga)Se-2 solar cells," *Thin Solid Films*, vol. 431, pp. 387-391, May 2003.
[128] J. H. Scofield, A. Duda, D. Albin, B. L. Ballard, and P. K. Predecki, "SPUTTERED MOLYBDENUM BILAYER BACK CONTACT FOR COPPER INDIUM DISELENIDE-BASED POLYCRYSTALLINE THIN-FILM SOLAR-CELLS," *Thin Solid Films*, vol. 260, pp. 26-31, May 1995.
[129] J. J. Scragg, J. T. Watjen, M. Edoff, T. Ericson, T. Kubart, and C. Platzer-Bjorkman, "A Detrimental Reaction at the Molybdenum Back Contact in Cu2ZnSn(S,Se)(4) Thin-Film Solar Cells," *Journal of the American Chemical Society*, vol. 134, pp. 19330-19333, Nov 28 2012.
[130] J. J. Scragg, P. J. Dale, D. Colombara, and L. M. Peter, "Thermodynamic Aspects of the Synthesis of Thin-Film Materials for Solar Cells," *Chemphyschem*, vol. 13, pp. 3035-3046, Aug 27 2012.
[131] K. Golasa, M. Grzeszczyk, K. P. Korona, R. Bozek, J. Binder, J. Szczytko, *et al.*, "Optical Properties of Molybdenum Disulfide (MoS2)," *Acta Physica Polonica A*, vol. 124, pp. 849-851, Nov 2013.
[132] A. Santoni, F. Biccari, C. Malerba, M. Valentini, R. Chierchia, and A. Mittiga, "Valence band offset at the CdS/Cu2ZnSnS4 interface probed by x-ray photoelectron spectroscopy," *Journal of Physics D-Applied Physics*, vol. 46, May 1 2013.

[133] M. Rusu, T. Glatzel, C. A. Kaufmann, A. Neisser, S. Siebentritt, S. Sadewasser, *et al.*, "High-efficient ZnO/PVD-CdS/Cu(In,Ga)Se-2 thin film solar cells: Formation of the buffer-absorber interface and transport properties," in *Symposium on Thin-Film Compound Semiconductor Photovoltaics held at the 2005 MRS Spring Meeting*, San Francisco, CA, 2005, pp. 449-455.

[134] T. Nakada and A. Kunioka, "Direct evidence of Cd diffusion into Cu(In,Ga)Se-2 thin films during chemical-bath deposition process of CdS films," *Applied Physics Letters*, vol. 74, pp. 2444-2446, Apr 26 1999.

[135] S. Tajima, R. Asahi, D. Isheim, D. N. Seidman, T. Itoh, M. Hasegawa, *et al.*, "Atom-probe tomographic study of interfaces of Cu2ZnSnS4 photovoltaic cells," *Applied Physics Letters*, vol. 105, Sep 1 2014.

[136] J. B. Varley and V. Lordi, "Intermixing at the absorber-buffer layer interface in thin-film solar cells: The electronic effects of point defects in Cu(In,Ga)(Se,S)(2) and Cu2ZnSn(Se,S)(4) devices," *Journal of Applied Physics*, vol. 116, Aug 14 2014.

[137] A. Fairbrother, E. Garcia-Hemme, V. Izquierdo-Roca, X. Fontane, F. A. Pulgarin-Agudelo, O. Vigil-Galan, *et al.*, "Development of a Selective Chemical Etch To Improve the Conversion Efficiency of Zn-Rich Cu2ZnSnS4 Solar Cells," *Journal of the American Chemical Society*, vol. 134, pp. 8018-8021, May 2012.

[138] J. Hedstrom, H. Ohlsen, M. Bodegard, A. Kylner, L. Stolt, D. Hariskos, *et al.*, "ZNO/CDS/CU(IN,GA)SE2 THIN-FILM SOLAR-CELLS WITH IMPROVED PERFORMANCE," in *23rd IEEE Photovoltaic Specialists Conference*, Louisville, Ky, 1993, pp. 364-371.

[139] R. V. Forest, K. Han, E. Eser, J. G. G. Chen, R. W. Birkmire, and Ieee, "Understanding the Effect of Na in Improving the Performance of Cu(InGa)Se-2-Based Photovoltaics," in *39th IEEE Photovoltaic Specialists Conference (PVSC)*, Tampa, FL, 2013, pp. 371-375.

[140] D. H. Cho, Y. D. Chung, K. S. Lee, J. H. Kim, S. J. Park, J. Kim, *et al.*, "Control of Na Diffusion from Soda-Lime Glass and NaF Film into Cu(In, Ga)Se-2 for Thin-Film Solar Cells," in *38th IEEE Photovoltaic Specialists Conference (PVSC)*, Austin, TX, 2012.

[141] W. M. H. Oo, J. L. Johnson, A. Bhatia, E. A. Lund, M. M. Nowell, and M. A. Scarpulla, "Grain Size and Texture of Cu2ZnSnS4 Thin Films Synthesized by Cosputtering Binary Sulfides and Annealing: Effects of Processing Conditions and Sodium," *Journal of Electronic Materials*, vol. 40, pp. 2214-2221, Nov 2011.

[142] K. J. Yang, J. H. Sim, B. Jeon, D. H. Son, D. H. Kim, S. J. Sung, *et al.*, "Effects of Na and MoS2 on Cu2ZnSnS4 thin-film solar cell," *Progress in Photovoltaics*, vol. 23, pp. 862-873, Jul 2015.

[143] A. Nagaoka, H. Miyake, T. Taniyama, K. Kakimoto, Y. Nose, M. A. Scarpulla, *et al.*, "Effects of sodium on electrical properties in Cu2ZnSnS4 single crystal," *Applied Physics Letters*, vol. 104, Apr 2014.

[144] C. M. Sutter-Fella, J. A. Stuckelberger, H. Hagendorfer, F. La Mattina, L. Kranz, S. Nishiwaki, *et al.*, "Sodium Assisted Sintering of Chalcogenides and Its Application to Solution Processed Cu2ZnSn(S,Se)(4) Thin Film Solar Cells," *Chemistry of Materials,* vol. 26, pp. 1420-1425, Feb 2014.
[145] M. I. Amal and K. H. Kim, "The influence of the precursor compositional ratio on Cu2ZnSnS4 films prepared by using sulfurization of the metallic precursor," *Journal of the Korean Physical Society,* vol. 63, pp. 2194-2198, Dec 2013.
[146] A. D. Collord and H. W. Hillhouse, "Composition Control and Formation Pathway of CZTS and CZTGS Nanocrystal Inks for Kesterite Solar Cells," *Chemistry of Materials,* vol. 27, pp. 1855-1862, Mar 2015.
[147] H. Nishi, S. Kuwabata, and T. Torimoto, "Composition-Dependent Photoelectrochemical Properties of Nonstoichiometric Cu2ZnSnS4 Nanoparticles," *Journal of Physical Chemistry C,* vol. 117, pp. 21055-21063, Oct 2013.
[148] Y. Zhao, X. X. Han, W. Li, L. Liu, and T. Tanaka, "Synthesis of the Cu2ZnSn(S,Se)(4) alloys with tunable phase structure and composition via a novel non-toxic solution method," *Rsc Advances,* vol. 3, pp. 26160-26165, 2013.
[149] T. P. Dhakal, C.-Y. Peng, R. R. Tobias, R. Dasharathy, and C. R. Westgate, "Characterization of a CZTS thin film solar cell grown by sputtering method," *Solar Energy,* vol. 100, pp. 23-30, Feb 2014.
[150] H. Katagiri, K. Jimbo, S. Yamada, T. Kamimura, W. S. Maw, T. Fukano, *et al.*, "Enhanced conversion efficiencies of Cu2ZnSnS4-based thin film solar cells by using preferential etching technique," *Applied Physics Express,* vol. 1, Apr 2008.
[151] S. Lopez-Marino, Y. Sanchez, M. Placidi, A. Fairbrother, M. Espindola-Rodriguez, X. Fontane, *et al.*, "ZnSe Etching of Zn-Rich Cu2ZnSnSe4: An Oxidation Route for Improved Solar-Cell Efficiency," *Chemistry-a European Journal,* vol. 19, pp. 14814-14822, Oct 25 2013.
[152] P. M. P. Salome, P. A. Fernandes, and A. F. da Cunha, "Morphological and structural characterization of Cu2ZnSnSe4 thin films grown by selenization of elemental precursor layers," *Thin Solid Films,* vol. 517, pp. 2531-2534, Feb 2 2009.
[153] G. Gordillo, C. Calderon, and P. Bartolo-Perez, "XPS analysis and structural and morphological characterization of Cu2ZnSnS4 thin films grown by sequential evaporation," *Applied Surface Science,* vol. 305, pp. 506-514, Jun 30 2014.
[154] M. Y. Valakh, O. F. Kolomys, S. S. Ponomaryov, V. O. Yukhymchuk, I. S. Babichuk, V. Izquierdo-Roca, *et al.*, "Raman scattering and disorder effect in Cu2ZnSnS4," *Physica Status Solidi-Rapid Research Letters,* vol. 7, pp. 258-261, Apr 2013.
[155] M. Altosaar, J. Raudoja, K. Timmo, M. Danilson, M. Grossberg, J. Krustok, *et al.*, "Cu2Zn1-xCdxSn(Se1-ySy)(4) solid solutions as absorber materials for solar

cells," *Physica Status Solidi a-Applications and Materials Science,* vol. 205, pp. 167-170, Jan 2008.
[156] P. A. Fernandes, P. M. P. Salome, and A. F. da Cunha, "Study of polycrystalline Cu2ZnSnS4 films by Raman scattering," *Journal of Alloys and Compounds,* vol. 509, pp. 7600-7606, Jul 2011.
[157] "Handbook of Sputter Deposition Technology: Fundamentals and Applications for Functional Thin Films, Nanomaterials, and MEMS, 2nd Edition," *Handbook of Sputter Deposition Technology: Fundamentals and Applications for Functional Thin Films, Nanomaterials, and Mems, 2nd Edition,* pp. 1-644, 2012.
[158] "Characterization of Advanced Materials," *Characterization of Advanced Materials,* vol. 699, pp. 1-294, 2012.
[159] C. L. Feldman and W. J. Mayer, *Fundamentals of surface and thin film analysis,* 1986.
[160] G. Golan, A. Axelevitch, B. Gorenstein, and V. Manevych, "Hot-Probe method for evaluation of impurities concentration in semiconductors," *Microelectronics Journal,* vol. 37, pp. 910-915, Sep 2006.
[161] Z. V. Bart, "Semiconductor Fundamentals," in *Principles of Electronic Devices,* ed, 2011.
[162] R. Green, "Hall Effect Measurements in Materials Characterization," ed: Keithley Online Webinar, 2011.
[163] L. B. Valdes, "Resistivity Measurements on Germanium for Transistors," in *Proceedings of the IRE,* 1954.
[164] V. P. Kutavichus, V. V. Filippov, and V. H. Huzouski, "Determination of optical parameters and thickness of weakly absorbing thin films from reflectance and transmittance spectra," *Applied Optics,* vol. 45, pp. 4547-4553, Jul 2006.
[165] E. H. Rhoderick and R. H. Williams, *Metal-Semiconductor Contacts*: Clarendon Press, Oxford, 1988.
[166] P. Muret, "THE INFLUENCE OF INTERFACE STATES UPON THE ADMITTANCE OF METAL-SEMICONDUCTOR DIODES," *Semiconductor Science and Technology,* vol. 3, pp. 321-338, Apr 1988.
[167] H. Kroemer, W. Y. Chien, J. S. Harris, and D. D. Edwall, "MEASUREMENT OF ISOTYPE HETEROJUNCTION BARRIERS BY C-V PROFILING," *Applied Physics Letters,* vol. 36, pp. 295-297, 1980 1980.
[168] K. Steiner, "CAPACITANCE VOLTAGE MEASUREMENTS ON SCHOTTKY DIODES WITH POOR OHMIC CONTACTS," *Ieee Transactions on Instrumentation and Measurement,* vol. 42, pp. 39-43, Feb 1993.
[169] I. L. Repins, B. J. Stanbery, D. L. Young, S. S. Li, W. K. Metzger, C. L. Perkins, *et al.*, "Comparison of device performance and measured transport parameters in widely-varying Cu(In, Ga) (Se, S) solar cells," *Progress in Photovoltaics,* vol. 14, pp. 25-43, Jan 2006.

[170] J. Gilot, M. M. Wienk, and R. A. J. Janssen, "Measuring the External Quantum Efficiency of Two-Terminal Polymer Tandem Solar Cells," *Advanced Functional Materials*, vol. 20, pp. 3904-3911, Nov 2010.
[171] S. Karthikeyan, L. Zhang, and A. S. Campbell, "In-situ stress and thermal stability studies of molybdenum bilayer backcontacts for photovoltaic applications," presented at the Photovoltaic Specialists Conference (PVSC), 2014.
[172] Z. F. Tong, C. Yan, Z. H. Su, F. Q. Zeng, J. Yang, Y. Li, *et al.*, "Effects of potassium doping on solution processed kesterite Cu2ZnSnS4 thin film solar cells," *Applied Physics Letters*, vol. 105, Dec 2014.
[173] L. Dormehl. (2014). *Everything you wanted to know about sapphire glass, but were afraid to ask*. Available: http://www.cultofmac.com/267068/everything-wanted-know-sapphire-glass-afraid-ask-qa/
[174] B. H. W. S. d. Jong, "Ullmann's Encyclopedia of Industrial Chemistry, 5th edition," in *Glass*. vol. A12, ed Weinheim, Germany: VCH Publishers, 1989, pp. 365-432.
[175] U. Holzwarth and N. Gibson, "The Scherrer equation versus the 'Debye-Scherrer equation'," *Nature Nanotechnology*, vol. 6, pp. 534-534, Sep 2011.
[176] H. Yoo, J. H. Kim, and L. X. Zhang, "Sulfurization temperature effects on the growth of Cu2ZnSnS4 thin film," *Current Applied Physics*, vol. 12, pp. 1052-1057, Jul 2012.
[177] K. Maeda, K. Tanaka, Y. Nakano, and H. Uchiki, "Annealing Temperature Dependence of Properties of Cu2ZnSnS4 Thin Films Prepared by Sol-Gel Sulfurization Method," *Japanese Journal of Applied Physics*, vol. 50, p. 4, May 2011.
[178] M. Johnson, M. Manno, X. Zhang, C. Leighton, and E. S. Aydil, "Substrate and temperature dependence of the formation of the Earth abundant solar absorber Cu2ZnSnS4 by ex situ sulfidation of cosputtered Cu-Zn-Sn films," *Journal of Vacuum Science & Technology A*, vol. 32, Nov 2014.
[179] Z. Moser, J. Dutkiewicz, W. Gasior, and J. Salawa, "The Sn-Zn (Tin-Zinc) system," vol. 6, ed. Bulletin of Alloy Phase Diagrams, 1985, pp. 330-334.
[180] S. Karthikeyan, Liyuan Campbell, A. Stephen, "In-situ stress and thermal stability studies of molybdenum bilayer backcontacts for photovoltaic applications," presented at the Photovoltaic Specialists Conference (PVSC), 2014.
[181] J. Carper, "The CRC Handbook of Chemistry and Physics," *Library Journal*, vol. 124, pp. 192-+, Jun 1999.
[182] D. Griffiths, *Introduction to Electrodynamics (3rd Edition)*. Upper Saddle River, New Jersey: Prentice Hall, 1999.
[183] *The Engineering Toolbox*. Available: http://www.engineeringtoolbox.com/resistivity-conductivity-d_418.html
[184] *MetalPrices.com*. Available: http://www.metalprices.com/

[185] *Mining Markets and Investment*. Available: http://www.infomine.com/investment/metal-prices/
[186] C. Platzer-Bjorkman, J. Scragg, H. Flammersberger, T. Kubart, and M. Edoff, "Influence of precursor sulfur content on film formation and compositional changes in Cu2ZnSnS4 films and solar cells," *Solar Energy Materials and Solar Cells*, vol. 98, pp. 110-117, Mar 2012.
[187] H. Y. Zhao and C. Persson, "Optical properties of Cu(In,Ga)Se-2 and Cu2ZnSn(S,Se)(4)," *Thin Solid Films*, vol. 519, pp. 7508-7512, Aug 2011.
[188] J. J. S. Scragg, L. Choubrac, A. Lafond, T. Ericson, and C. Platzer-Bjorkman, "A low-temperature order-disorder transition in Cu2ZnSnS4 thin films," *Applied Physics Letters*, vol. 104, p. 4, Jan 2014.